

ISVR Technical Report

SCIENTIFIC PUBLICATIONS BY THE ISVR

Technical Reports are published to promote timely dissemination of research results by ISVR personnel. This medium permits more detailed presentation than is usually acceptable for scientific journals. Responsibility for both the content and any opinions expressed rests entirely with the author(s).

Technical Memoranda are produced to enable the early or preliminary release of information by ISVR personnel where such release is deemed to be appropriate. Information contained in these memoranda may be incomplete, or form part of a continuing programme; this should be borne in mind when using or quoting from these documents.

Contract Reports are produced to record the results of scientific work carried out for sponsors, under contract. The ISVR treats these reports as confidential to sponsors and does not make them available for general circulation. Individual sponsors may, however, authorize subsequent release of the material.

COPYRIGHT NOTICE

(c) ISVR University of Southampton All rights reserved.

ISVR authorises you to view and download the Materials at this Web site ("Site") only for your personal, non-commercial use. This authorization is not a transfer of title in the Materials and copies of the Materials and is subject to the following restrictions: 1) you must retain, on all copies of the Materials downloaded, all copyright and other proprietary notices contained in the Materials; 2) you may not modify the Materials in any way or reproduce or publicly display, perform, or distribute or otherwise use them for any public or commercial purpose; and 3) you must not transfer the Materials to any other person unless you give them notice of, and they agree to accept, the obligations arising under these terms and conditions of use. You agree to abide by all additional restrictions displayed on the Site as it may be updated from time to time. This Site, including all Materials, is protected by worldwide copyright laws and treaty provisions. You agree to comply with all copyright laws worldwide in your use of this Site and to prevent any unauthorised copying of the Materials.

UNIVERSITY OF SOUTHAMPTON
INSTITUTE OF SOUND AND VIBRATION RESEARCH
FLUID DYNAMICS AND ACOUSTICS GROUP

**First Stage Investigations of Acoustic Wave Propagation in a Liquid-Filled Cylindrical
Tube With and Without Bubbles**

by

K. Baik, J. Jiang and T.G. Leighton

ISVR Technical Report No. 328

August 2009

Authorised for issue by
Professor R. J. Astley
Group Chairman

I. EXECUTIVE SUMMARY	2
I-1 The flow rig	3
I-2 The sensors	6
I-3 Summary	8
II. INTRODUCTION TO THE STATIC TEST RIG	9
III. THEORETICAL MODEL	11
III-1. Speed of sound in non-bubbly liquid cylinder	11
III-2. Speed of sound in bulk bubbly media – single distribution	19
III-3. Speed of sound in bulk bubbly media – mixed distribution	24
III-4. Attenuation coefficients	28
III-5. Estimating the bubble distribution by acoustic inversion	30
III-6. Conclusions	31
IV. NUMERICAL STUDY USING FINITE ELEMENTS	33
IV-1. Motivation	33
IV-2. Verify the correctness of theoretical analysis	33
IV-3. Test the methods used in experimental study	38
IV-4. Effect of bubbles on the propagation modes	41
IV-5. Conclusions	45
V. MEASUREMENTS AND RESULTS	46
V-1. Experimental facilities	46
V-2. Sound velocity measurements in bubble-free water	57
V-3. Sound velocity measurements in bubbly water	63
V-4. Attenuation coefficients measurements in bubbly water	67
V-5. Bubble spectrum through acoustic inversion	69
V-6. Bubble spectrum through μCORT Method	70
VI. CONCLUSION AND FUTURE WORK	74
APPENDIX A: DERIVATION OF DISPERSION RELATION	78
APPENDIX B: CHARACTERISTIC EQUATION AT THE ZERO FREQUENCY LIMIT	86
APPENDIX C: DERIVATION OF SOUND SPEED IN BUBBLY MIXTURE	90
APPENDIX D: MEASUREMENT OF BUBBLES USING OPTICAL FIBER	92
APPENDIX E: μCORT(MULTI-COLOR RISING TIME) METHOD	97
E1. Processing procedures	100
E2. Artificial case study for μCORT	104
APPENDIX F: TERMINAL VELOCITY OF BUBBLE IN LIQUID	107
APPENDIX G: DESIGN FOR MIMIC OF TEST SECTION	109
REFERENCES	113

I. EXECUTIVE SUMMARY

This report records the first stages in an investigation carried out with the support of a contract between ISVR and joint sponsors, the CCLRC Rutherford Appleton Laboratory (UK) and the Oak Ridge National Laboratory (ORNL, USA), to develop a suite of sensors capable of measuring the population of gas bubbles in liquid mercury flowing through pipelines. This capability is required to assist in the production of systems to mitigate against cavitation damage in the liquid metal spallation targets of a pulsed neutron source (Figure 1.1).



(a)



(b)

Figure 1.1 (a) The target section which can, on rails, be moved in and out of the chamber shown in (b).

The work has encompassed the design and ordering of equipment and initial studies with *ad hoc* facilities to familiarize the researchers with the techniques, allow them to begin aligning theory with practical observables, and inform the ongoing design and construction of the practical components.

The overall plan will be to equip a pipe with sensors suitable for sizing and counting bubbles. Multiple sensors will be deployed for two reasons. First, to ensure that the ambiguities in the results from one sensor are mitigated against by comparison with an independent sensor. Second, to ensure coverage of a wide range of bubble sizes (acoustical techniques tend to work better with bubbles in the 20-100 micron radius range, whilst optical techniques tend to work better in the 0.5-10 mm radius range).



Figure 1.2 The flow rig test loop at ORNL.

I-1 The flow rig

The bulk of the research work will be undertaken in a water-filled pipe rig constructed to resemble the flow rig at ORNL (Figure 1.2), including proposed extension modifications to the outflow pipe. The sensor systems developed in the project will be deployed and tested on that water-filled rig (which will be termed the ‘flow rig’ in this report) before being transposed to work in the mercury-filled flow test loop at ORNL. A copy of the provisional schematic of the design is shown in Figure 1.3.

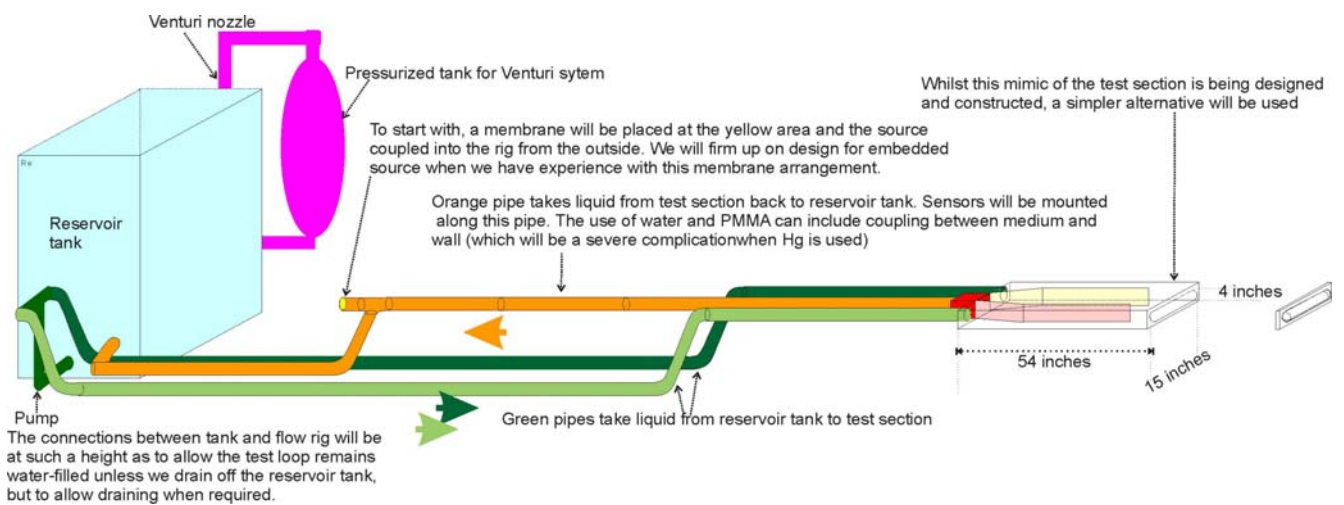


Figure 1.3 A copy of the provisional schematic for the design of the flow rig.

At the heart of the design is the reservoir tank (shown in blue at the left of Figure 1.3). Two separate pumping systems will draw water out of this tank, and return it to it. One supplies the pipework to the flow rig (the material to the right of the reservoir tank in Figure 1.3). The other is a Venturi-based bubble generation system. This is shown behind the reservoir tank in Figure 1.3, and is schematically detailed in Figure 1.4. Design complications included finding a suitable pump to cope with the void fractions expected, but these have been overcome and we expect the unit to work well in providing the required void fractions and bubble size distributions.

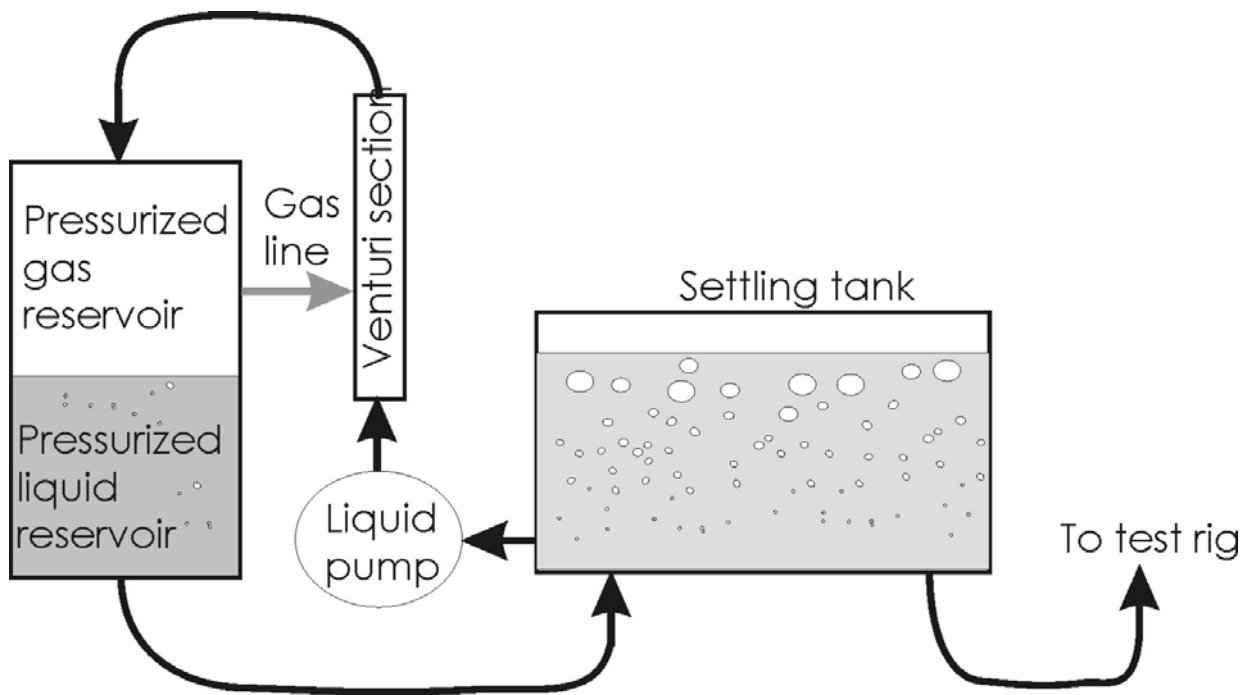


Figure 1.4 A schematic of the Venturi bubbler system.

The current state of the flow rig is shown in Figure 1.5. To speed construction of the flow rig, we have modified the initial design requirement to replace the target section shown in the extreme right of Figure 1.3 with a simpler alternative. This will be in place until the PMMA (Perspex) mimic for the test section is completed (Figure 1.6 - see Appendix G for details).

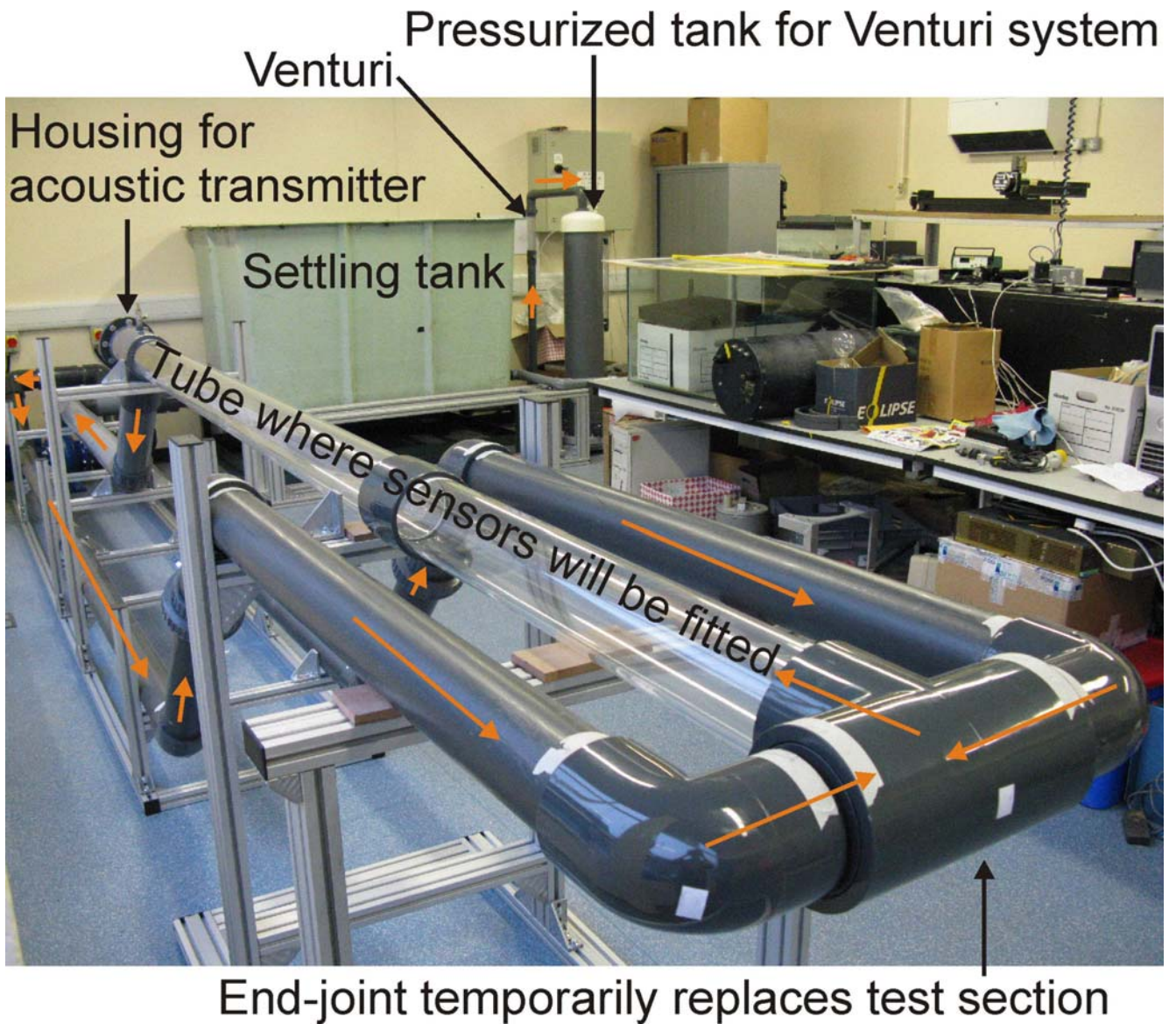


Figure 1.5: The flow rig under construction. The direction of flow is shown by the orange arrows.

Whilst the flow rig has been under construction, ISVR have constructed three static rigs (vertical liquid-filled pipes) in which to conduct experiments with *ad hoc* sensors (whilst the proper sensors are still being constructed) and work on the theory and simulations. One static rig has been shipped to Precision Acoustics, whilst the other is used in ISVR, and the third is kept as a spare (Fig. 1.6). The results of using the flow rig are discussed in Section V.

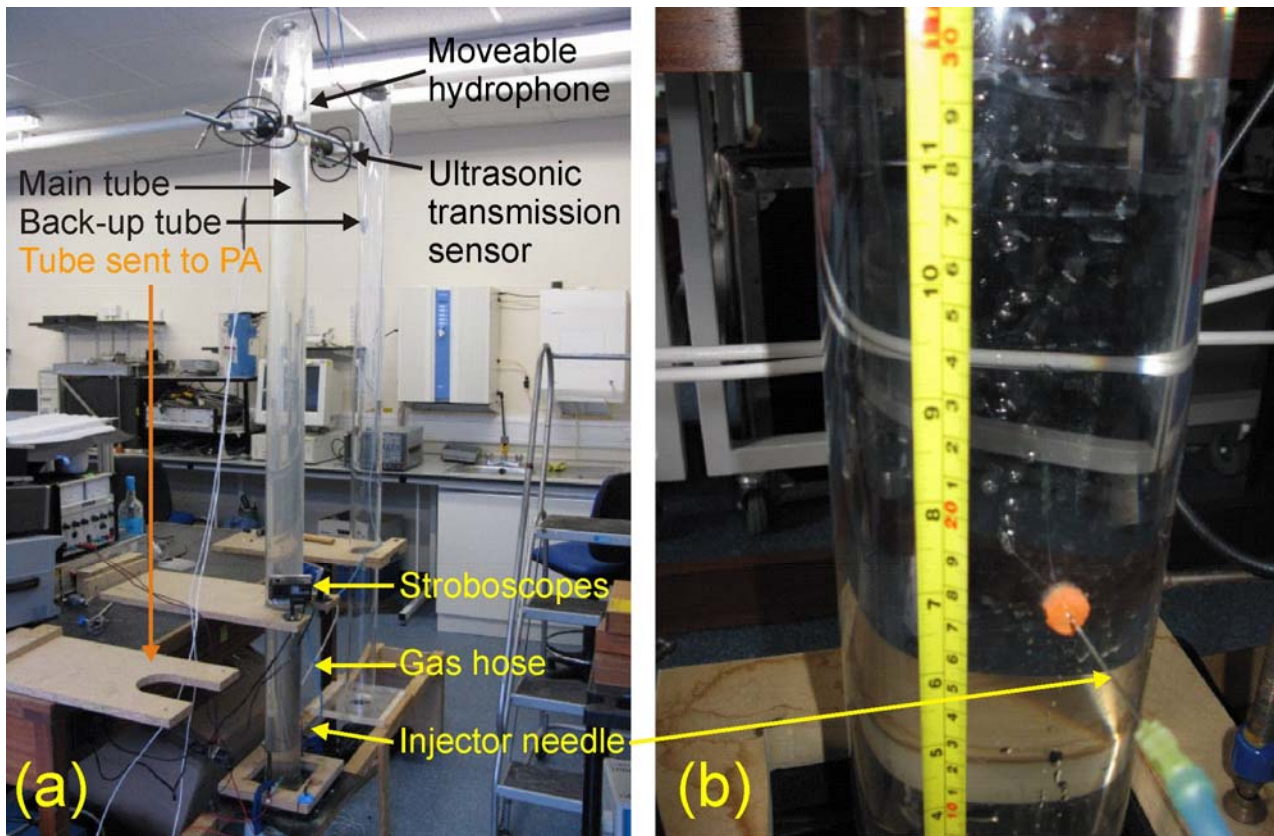


Figure 1.6: The static rig showing (a) the stand for 3 vertical pipes (the pipe on the left having been shipped to Precision Acoustics Ltd.) and (b) a close-up of the central pipe on which the ISVR measurements of this report are taken.

I-2 The sensors

Considerable discussion on the sensors has been undertaken with Precision Acoustics Ltd., building on the award-winning relationship¹ that has already developed between this company and ISVR. These discussions are aimed at developing the acoustic and fibre optic sensors. The requirement for the acoustic sensors was to cover the range from ~ 1 kHz to 1 MHz. Precision Acoustics believe that this range can be covered using two sensors, and are working towards that solution. There has been considerable discussion regarding the geometry of the hydrophone array. The inversion to measure the bubble population is based upon measurement of the attenuation, and the sensor spacing must not be so small that the attenuation measured between them is too small to invert, but neither must it be so large that there is no signal at the hydrophone which is furthest from the source. Given that, across the 1-1000 kHz band specified by the sponsors, the attenuation can vary enormously, fixed hydrophone spacings would present problems. A hydrophone which moves along the acoustic axis of the pipe was proposed (Figure 1.6), but could be very problematical, because of re-radiation of the sound from the rod. Therefore a design which inserts sensors through fixed access ports in the pipe will be used (Figure 1.7)

¹ See http://www.soton.ac.uk/mediacentre/news/2008/oct/08_181.shtml

Pole which slides up and down through centre of source and moves hydrophone along acoustic axis

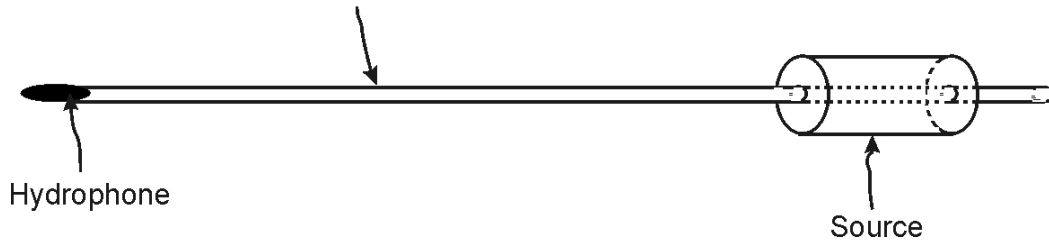


Figure 1.7: A speculative mounting to move a single hydrophone along the centerline of the pipe.

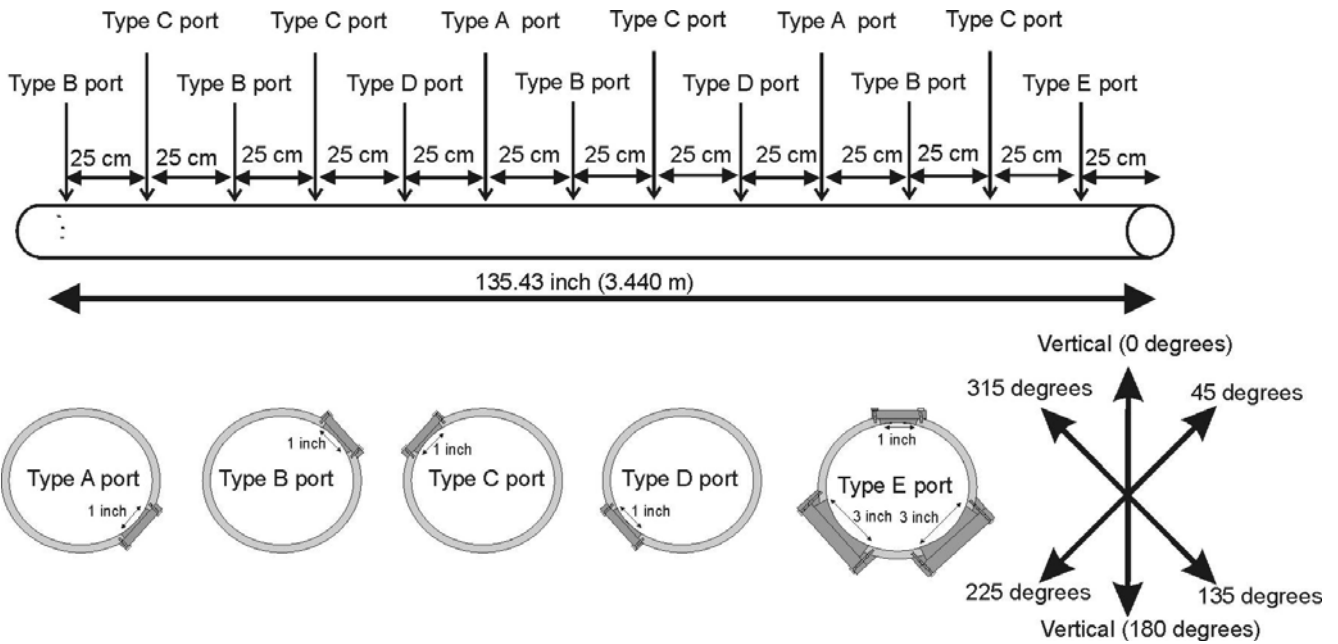


Figure 1.8: A schematic of initial design for access ports in the pipe. Sensor mountings are shown angled to one another to reduce acoustic shadowing effects at high frequencies. The type E port is designed to hold the combination frequency transducers.

The acoustical projectors have proven to be more problematical. Because of changes in the company who provided the quote included in the project proposal, that company will not be able to supply the necessary units. A replacement route is being investigated with Neptune Sonar. It is believed that sources with two amplifiers (ENI and Crowne), with appropriate matching, will accomplish the task.

With respect to the fiber optics bubble sensor, although a low-cost mock-up has worked well in water, it is believed that moving from a multi-mode to a single-mode fiber will be beneficial, and discussion are underway with Precision Acoustics Ltd. about adapting their fiber optic hydrophone technology to work as bubble detectors in mercury. ISVR has provided Precision Acoustics with a duplicate of one of the static rigs described later in the report (Section V), for them to use in testing their apparatus.

I-3 Summary

In summary, the acoustical and optical sensor systems are progressing, although there is considerable work to be done. The Venturi system and the flow rig are well underway (Section VI). In the meantime, a static rig has been constructed, and work on this will be the topic of the remainder of the report. Key to the measurement is an appreciation of the effects of coupling between the bulk liquid and the vessel walls, and this will be significant when mercury is contained within thin-walled steel pipes. Therefore the containment of water in plastic pipes provides a good test bed for explanation and understanding of this coupling. Such an understanding is required to implement bubble sensors in the geometry of the test loop. Section III will discuss the theoretical considerations, Section IV will outline the numerical studies, and Section V will describe the experimental tests to date.

II. INTRODUCTION TO THE STATIC TEST RIG

The object of this project is to provide tools to measure bubble populations inside a pipe at the Oak Ridge National Laboratory (ORNL). With respect to this, the phenomenon of wave propagation inside a liquid-filled cylindrical tube encompasses the important mechanism of sound coupling between the fluid and the elastic pipe material. It is important that this phenomenon be understood, since many of the methods for inverting acoustical observables to determine the bubble population rely on interpreting the difference between the observable (sound speed, attenuation, scattering etc.) in the bubbly fluid, and its value in bubble-free conditions. Critically, the ‘bubble-free’ value is almost always taken to refer to the value of the bulk liquid. However when the liquid is contained within a thin-wall pipe, the bubble-free value does not equal the value of the observable in an infinite body of liquid, and it is important that this difference is not interpreted in the inversion as being due to bubbles.

The test loop in ORNL consists of circulating liquid mercury along the stainless steel pipeline. The current contract is to design the required sensors in a water-based system, and then translate these sensors to the mercury-based system at ORNL. The issue of coupling between the wall and the liquid affects those sensors which are based on measurement of the phase and group velocities, attenuation and scattering, and these will be monitored at ISVR for the case of sound propagating through bubbly and bubble-free water. The presence of the bubbles changes those parameters and this information is used to infer the bubble size distribution and population [1-6].

Therefore in this report, propagation of the wave in water filled pipe is examined using theory, simulation and experiment, to test our ability to cope with the coupling between the water and the tube wall, and predict how it changes the speed of sound and attenuation coefficient. The experiments have been undertaken on a static rig because, although the liquid circulates inside the pipe in the ONRL test loop and the eventual ISVR flow rig, comparison of theory and simulation with experiment for wave propagation in the static liquid with and without bubbles provides a sensible starting point before proceeding [7-8].

The theoretical and experimental works done by Del Grosso [9] and Lafleur [10] were examined and re-derived in Section III, Appendix A, and Appendix B (the re-derivation was important to gain understanding, and also revealed errors in the original publications). The numerical prediction of the dispersion relation in the current PMMA pipe was also shown in this section. Section IV explains the numerical simulation by the Finite Element Model using the COMSOL software. The theoretical model described in Section III was examined and compared with the simulation in this section. Through the simulation, it is possible to check whether the phenomena predicted by the theory will happen and, further, it is possible to anticipate the results in the real mercury-based system. The configuration of the experiments and the measurements are described in Section V.

Section V also describes the comparison of the measurements with the theory (derived in Section III) and the simulations (described in Section IV). This was done for bubble-free conditions to provide a baseline, and then for bubbly conditions. Given the early stages of the work, the observations in bubbly water reported here are only preliminary observations, as the methods for independently characterizing the bubble population are not yet well-developed. In order to see the effect of the bubble on the wave propagation, bubbles were injected into the pipe and the experimental protocol derived for bubble-free water was repeated. The technique to generate the bubbles, apparatus, and the measurements with the bubbles were also shown in Section V. When the bubbles are introduced, it is important to measure the void fraction inside the liquid. Among several methods to measure the void fraction, a method using the optical fiber was briefly explained in Appendix D and the photographic method, called as μ CORT (Multi-Color Rising Time) is described in Appendix E. The latter technique, μ CORT, requires background information on the terminal velocity of rising bubbles in the liquid, and how this is derived for water and mercury is illustrated in Appendix F.

III. THEORETICAL MODEL

III-1. Speed of sound in non-bubbly liquid cylinder

The early work by Del Grosso [9] provided the theoretical axisymmetric modal dispersion relation in an infinite liquid-filled cylindrical tube, which was proven experimentally by Lafleur [10]. Their results specifically calculated the dispersion relation of axisymmetric propagation mode in a water-filled elastic tube. Del Grosso denoted those axisymmetric modes as ET_m, such that each axisymmetric mode is identified by only one integer *m* which indicates radial modes. These mode shapes are shown schematically in Appendix A. Assuming the time dependence of modes as $\exp(-i\omega t)$, the scalar potential ϕ and vector potential $\vec{\psi}$ in elastic media satisfy the Helmholtz equation in the cylindrical coordinates as follows:

$$\begin{aligned} \nabla^2 \phi + k_c^2 \phi &= 0 \\ \nabla^2 \vec{\psi} + k_s^2 \vec{\psi} &= 0, \end{aligned} \quad (1)$$

where

$$\nabla^2 = \frac{1}{r} \frac{\partial}{\partial r} \left(r \frac{\partial}{\partial r} \right) + \frac{1}{r^2} \frac{\partial^2}{\partial \theta^2} + \frac{\partial^2}{\partial z^2},$$

$k_c = \omega/C_c$ and $k_s = \omega/C_s$ are the longitudinal and shear wavenumbers respectively, and C_c and C_s are the longitudinal and shear speeds respectively. The Laplacian ∇^2 is only dependent on the variables r and z for the axisymmetric modes, and the derivative with respect to the angle θ can be eliminated. Because the displacement vector \vec{u} can be expressed as $\vec{u} = \nabla \phi + \nabla \times \vec{\psi}$, assuming the z -dependence of each potential as $\exp(ik_z z)$ (propagating modes to z -direction), the general solutions to the displacement vector \vec{u} in the axisymmetric modes can be expressed as [11]:

$$\vec{u}_w = -q_w [AJ_1(q_w r) + BY_1(q_w r)] \hat{r} + ik_z [AJ_0(q_w r) + BY_0(q_w r)] \hat{z} \quad (2)$$

$$\begin{aligned} \vec{u}_e = & -\{q_c [CJ_1(q_c r) + DY_1(q_c r)] + ik_z [EJ_1(q_s r) + FY_1(q_s r)]\} \hat{r} \\ & + \{ik_z [CJ_0(q_c r) + DY_0(q_c r)] + q_s [EJ_0(q_s r) + FY_0(q_s r)]\} \hat{z}, \end{aligned} \quad (3)$$

where,

$$q_c^2 = k_c^2 - k_z^2, \quad q_s^2 = k_s^2 - k_z^2, \quad q_w^2 = k^2 - k_z^2, \quad k = \omega/C_w.$$

The subscripts ‘w’ and ‘e’ indicate the water and the elastic solid respectively. The detail of the derivation is shown in Appendix A.

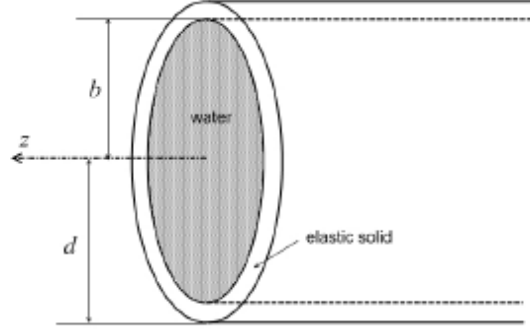


Figure 3.1: Geometry of liquid cylinder. Inner and outer radii are b and d respectively

Figure 3.1 shows the water-filled elastic tube with inner and outer radii b and d respectively. In this geometry, the value of coefficient B is zero to remove divergent behavior of the function $Y_n(q_\omega r)$ at $r = 0$. The other constants A , C , D , E , and F are to be determined from the boundary conditions that are based on the continuity of normal displacement, the continuity of the normal stress tensor, and the vanish of shear stress tensor. The resulting four equations with respect to four constants C , D , E , and F are as follows.

$$\begin{aligned} & C[iq_c k_z J_1(q_c b)] + D[iq_c k_z Y_1(q_c b)] \\ & + E[-(k_z^2 - k_s^2/2)J_1(q_s b)] + F[-(k_z^2 - k_s^2/2)Y_1(q_s b)] = 0, \end{aligned} \quad (4)$$

$$\begin{aligned} & C[iq_c k_z J_1(q_c d)] + D[iq_c k_z Y_1(q_c d)] \\ & + E[-(k_z^2 - k_s^2/2)J_1(q_s d)] + F[-(k_z^2 - k_s^2/2)Y_1(q_s d)] = 0, \end{aligned} \quad (5)$$

$$\begin{aligned} & C \left[P J_0(q_c b) + q_c \frac{1 + Qb}{b} J_1(q_c b) \right] + D \left[P Y_0(q_c b) + q_c \frac{1 + Qb}{b} Y_1(q_c b) \right] \\ & + E \left[-ik_z q_s J_0(q_s b) + ik_z \frac{1 + Qb}{b} J_1(q_s b) \right] + F \left[-ik_z q_s Y_0(q_s b) + ik_z \frac{1 + Qb}{b} Y_1(q_s b) \right] \\ & = 0, \end{aligned} \quad (6)$$

$$\begin{aligned}
& C \left[P J_0(q_c d) + \frac{q_c}{d} J_1(q_c d) \right] + D \left[P Y_0(q_c d) + \frac{q_c}{d} Y_1(q_c d) \right] \\
& + E \left[-i k_z q_s J_0(q_s d) + \frac{i k_z}{d} J_1(q_s d) \right] + F \left[-i k_z q_s Y_0(q_s d) + \frac{i k_z}{d} Y_1(q_s d) \right] \\
& = 0,
\end{aligned} \tag{7}$$

where,

$$Q = \frac{\rho_w \omega^2 J_0(q_w b)}{2 \rho_e C_s^2 q_w J_1(q_w b)}, \quad P = k_z^2 - \frac{k_s^2}{2},$$

and ρ_w and ρ_e are the density of water and the elastic solid respectively. Equations (4)-(7) are compared to Eqs. (4a)-(4d) in Lafleur's result [10]. However his expression has typographical errors in Eq. (4d). It is necessary to add P_m in front of $Y_1(bP_m)$ in the second line and substitute d with b for the denominator on the second term in the fourth line. The non-trivial solutions for these equations are determined by the determinant of 4×4 matrix, which is:

$$\begin{aligned}
1 & + [L_{11}(q_c) L_{00}(q_s)] \frac{bd}{2} \left(\frac{\pi k_z q_c q_s}{2P} \right)^2 + [L_{11}(q_s) L_{00}(q_c)] \frac{bd}{2} \left(\frac{\pi P}{2k_z} \right)^2 \\
& + [L_{10}(q_c) L_{01}(q_s) + L_{01}(q_c) L_{10}(q_s)] \left(\frac{bd \pi^2 q_c q_s}{8} \right) \\
& + [b L_{11}(q_c) L_{10}(q_s) + d(1 + Qb) L_{11}(q_c) L_{01}(q_s)] \left(\frac{\pi^2 q_c^2 q_s}{8P} - \frac{\pi^2 q_c^2 k_z^2 q_s}{8P^2} \right) \\
& + [b L_{11}(q_s) L_{10}(q_c) + d(1 + Qb) L_{11}(q_s) L_{01}(q_c)] \left(\frac{\pi^2 q_c P}{8k_z^2} - \frac{\pi^2 q_c}{8} \right) \\
& + [(1 + Qb) L_{11}(q_s) L_{11}(q_c)] \left(\frac{\pi^2 q_c^2}{8k_z^2} + \frac{\pi^2 q_c^2 k_z^2}{8P^2} - \frac{\pi^2 q_c^2}{4P} \right) = 0,
\end{aligned} \tag{8}$$

where $L_{mn}(y) = J_m(dy) Y_n(by) - J_n(by) Y_m(dy)$. The detailed derivation of this equation is shown in Appendix A.

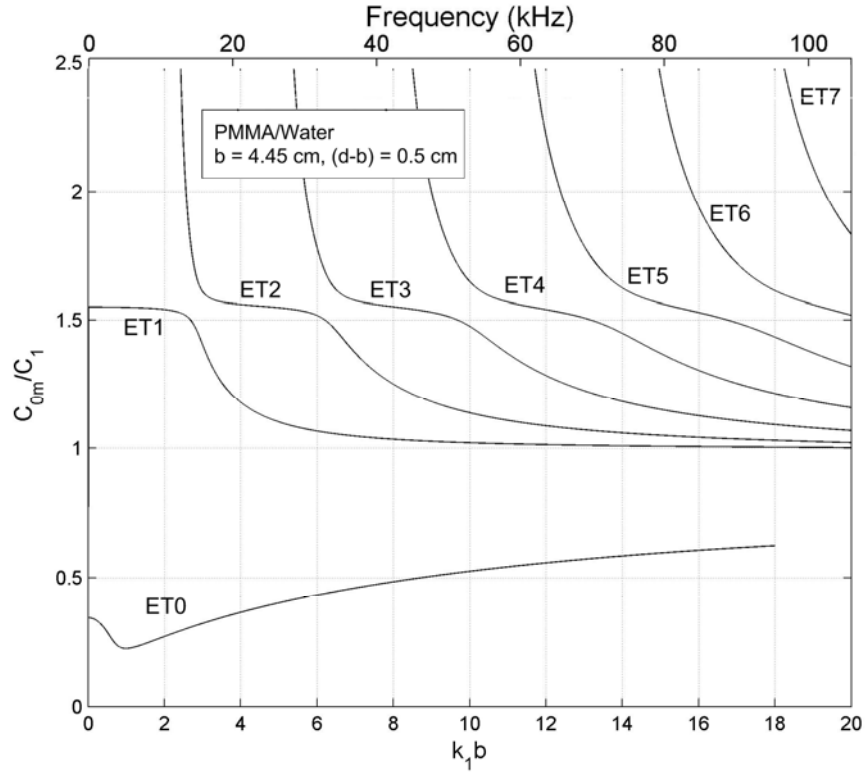


Figure 3.2: Normalized phase velocity of axisymmetric modes in the water-filled PMMA (Perspex) pipe as a function of frequency. The material properties of PMMA are shown in Table 3 [12].

This characteristic equation cannot be solved analytically, but roots to k_z can be found using numerical manipulation by appropriate mathematical software. Figures 3.2 and 3.3 show the normalized phase and group velocities of axisymmetric modes in the water-filled PMMA pipe as a function of frequency. The displacement profile of each axi-symmetric mode is shown in Appendix A. The phase velocity of each mode is calculated as $C_{0m} = \omega/k_z$ from roots to k_z . At the zero frequency limit, two modes (ET0 and ET1) exist at $C_{00}/C_\omega = 0.343$ and $C_{01}/C_\omega = 1.552$. The detail for the modal dispersion at the zero frequency limit is explained in Appendix B. The phase velocities of other modes becomes infinite at the cut-off frequency. As the frequency increases, the phase velocity of the ET1 mode converges to C_ω , the speed of sound in water, and the phase velocity of the ET0 mode approaches $C_{00}/C_\omega = 0.63$. Other higher modes can be seen, and their phase velocities are decreasing as the frequency increases. Group velocities can be easily converted from the calculated phase velocities using following relation where c_l is phase velocity and c_g is group velocity [13].

$$\frac{c_g}{c} = \frac{c_l}{c} \left[1 - \frac{1}{1 - \frac{c_l/c}{ka \frac{d(c_l/c)}{d(ka)}}} \right]. \quad (9)$$

Although ET2 and the higher modes have infinite phase velocities at the cut-off frequency limit, their group velocities approach zero at their cut-off frequencies. The consequence of this is that these modes do not exist at driving frequencies that are less than their cut-off frequencies. Hence this report will concentrate upon the ET0 and ET1 modes, and their properties will be compared through the theoretical calculations in this section and the simulation in the next section (the comparison with experimental observations is discussed in Section V).

The cut-off frequency of the mode is obtained from Eq. (8) at the limit of $k_z \rightarrow 0$. Multiplying both sides of Eq. (8) by k_z , then eliminating vanishing terms as k_z goes to zero, and arranging remaining terms, allows Eq. (8) to be reduced as follows:

$$bdP'^2L_{00}(k_c) + k_cP'[bL_{10}(k_c) + d(1 + Q'b)L_{01}(k_c)] + k_c^2(1 + Q'b)L_{11}(k_c) = 0, \quad (10)$$

where

$$P' = -\frac{k_s^2}{2}, \quad Q' = \frac{\rho_w k_s^2 J_0(kb)}{2\rho_e k J_1(kb)},$$

are the limiting form of P and Q respectively as $k_z \rightarrow 0$. In the numerical and experimental studies we will focus on phase velocity, and it can be changed to group velocity if it is necessary (as mentioned previously). The cut-off frequencies of the modes are given by the roots of Eq. (10) when it is solved with respect to frequency ω . Table 1 shows the cut-off frequencies of the modes. The values of the frequencies are expressed in terms of dimensionless quantity kb . Thus, below the cut-off frequencies, ET2 and higher modes do not exist and are not observed. Figure 3.4 shows the phase and group velocities of ET2 mode with the indication of its cut-off frequency. As the driving frequency approaches the cut-off frequency, the phase velocity goes to infinity and the group velocity goes to zero. Except for the ET0 and ET1 modes, all other modes have the same pattern as those shown in Figs. 3.2

In the ORNL test loop, liquid mercury is pumped through stainless steel pipes. However, as discussed earlier, for reasons of cost and safety the experiments in ISVR will be conducted in water-filled PMMA pipes. The above formulation can be used to show the extent to which the water/PMMA

system can be used to capture the coupling issues that will occur in the Hg system at ORNL. This relationship can be demonstrated by the theoretical modal dispersion curves for the mercury-filled stainless steel cylinder as shown in Figs. 3.5 and 3.6.

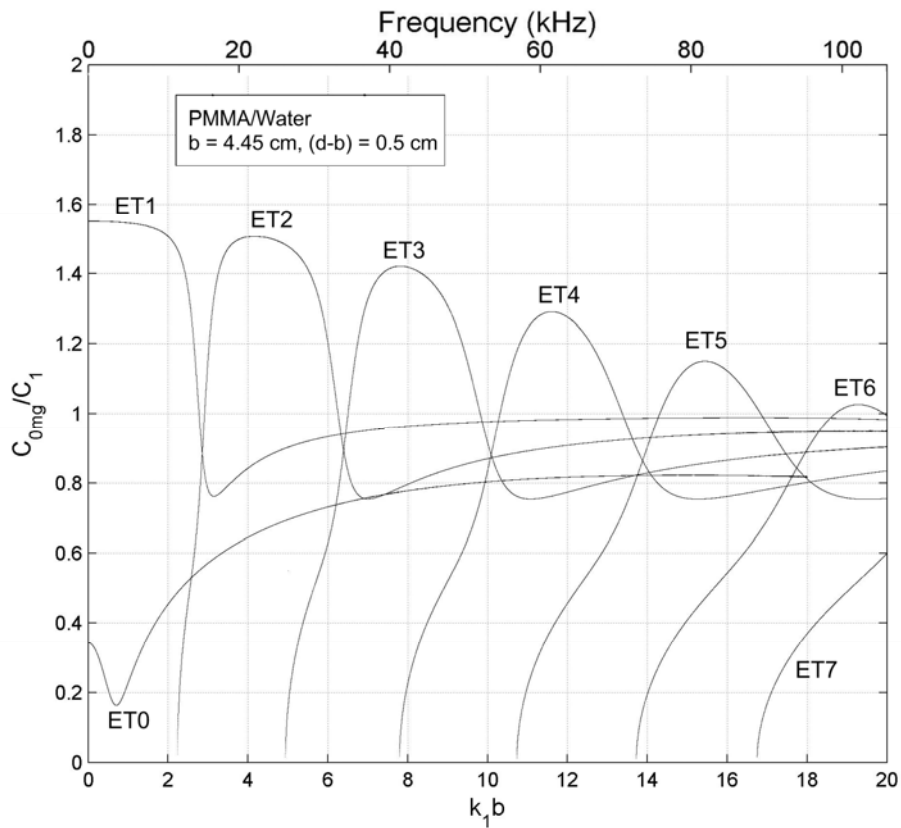


Figure 3.3: Normalised group velocity of axisymmetric modes in the water-filled PMMA pipe as a function of frequency.

Table 1: Cut-off frequencies of the modes.

Mode	ET2	ET3	ET4	ET5	ET6	ET7
Cut-off frequency (kb)	2.234	4.938	7.792	10.730	13.722	16.744

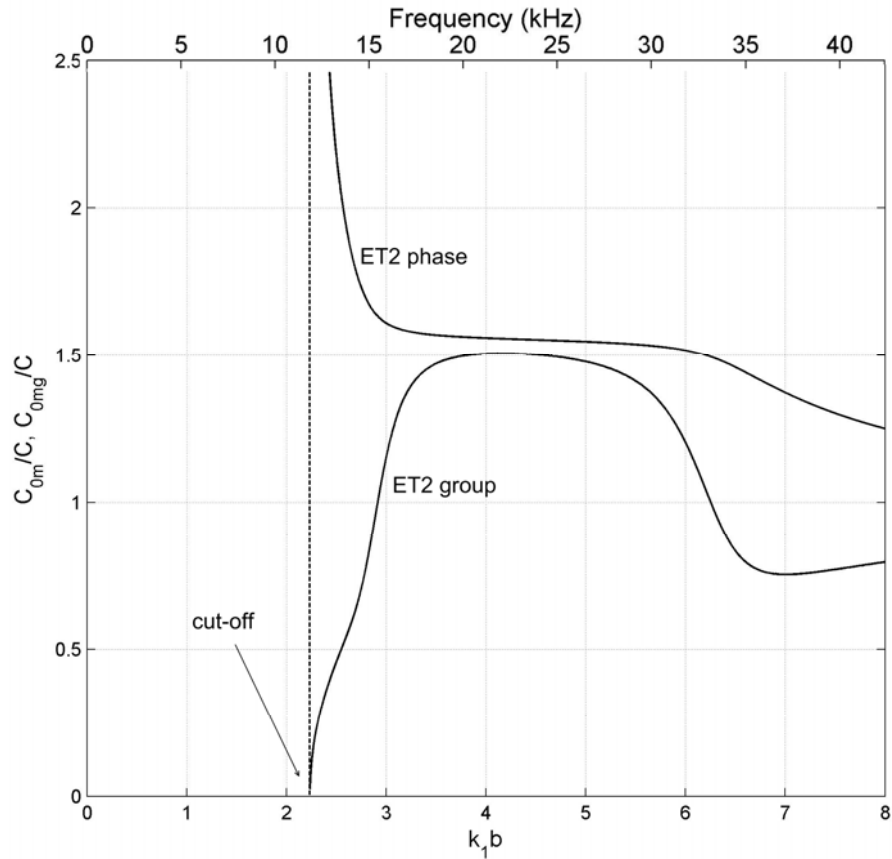


Figure 3.4: Phase and group velocities of ET2 mode. At the cut-off frequency, the phase velocity approaches infinity and the group velocity goes to zero.

Those graphs (Figs. 3.5 and 3.6.) were produced using a similar dimension for the pipe (4 in. inner diameter and 1 cm thickness) to that which occurs in ORNL and the ISVR rigs. Figure 3.5 shows the phase velocities of the modes calculated from Eq. (8), and Fig. 3.6 shows the group velocities of the modes calculated from Eq. (9) for the mercury-filled stainless steel pipe. The material properties of the stainless steel used here are 5.675 km/s for the longitudinal speed, 0.2792 for the Poisson's ratio, and 7.9 g/cm³ for the density. The values of parameters for liquid mercury are 13.5 g/cm³ for the density and 1.451 km/s for the speed of sound. Comparing these graphs with Figs. 3.2 and 3.3, many similarities between two cases can be observed. The behaviors of the phase velocity and group velocity at both the zero and high frequency limits are similar. Although the numerical values are different, the frequency dependence of the modes is very similar between two cases. Hence, the acoustical coupling between mercury and the steel is similar as that between water and the PMMA. This analysis will be used to assist in the transference of the results obtained in the water-PMMA pipework at ISVR to the ORNL mercury based system.

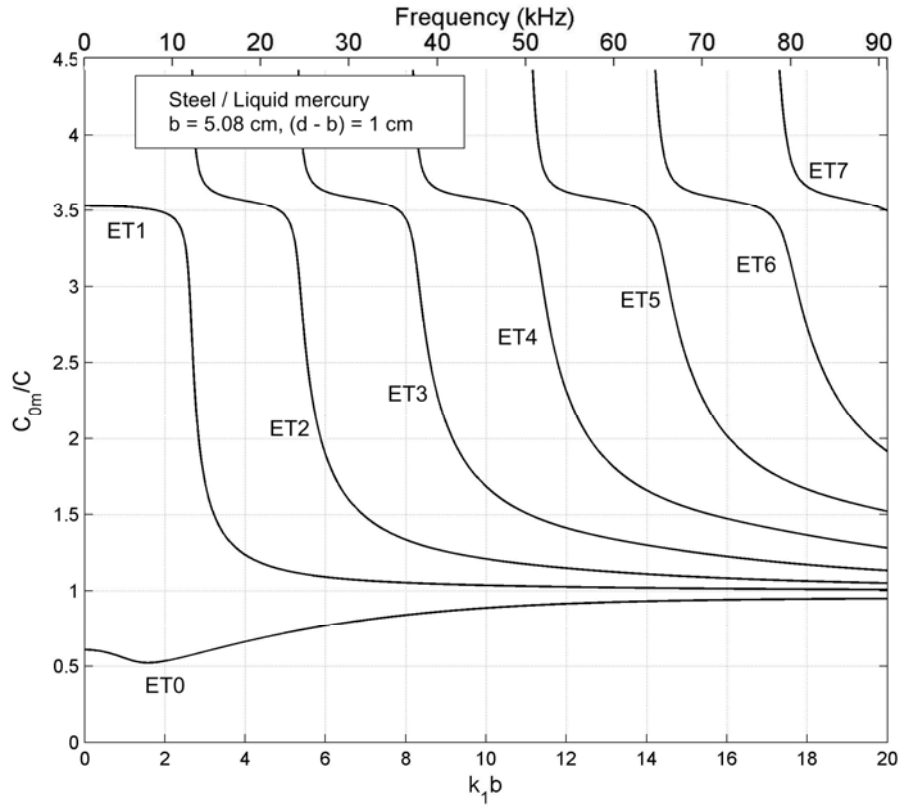


Figure 3.5: Normalized phase velocity of axisymmetric modes in the liquid mercury-filled stainless steel pipe as a function of frequency. Compare this with Fig. 3.2.

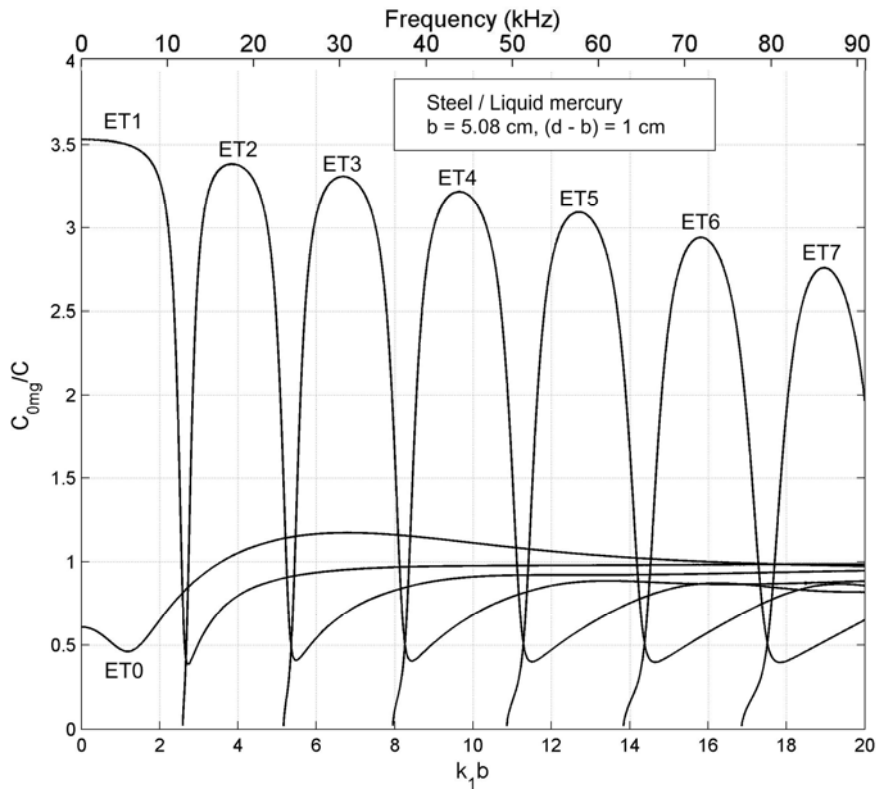


Figure 3.6: Normalized group velocity of axisymmetric modes in the liquid mercury-filled stainless steel pipe as a function of frequency. Compare this with Fig. 3.3.

III-2. Speed of sound in bulk bubbly media – single distribution

When bubbles are injected into pure media, the elastic properties of the media change. The bubble presence affects the compressibility (or bulk modulus) and the density of the mixture. Because the square of the sound speed is given by the ratio of the bulk modulus divided by the density, and because bubbles both absorb and scatter sound, propagation of the sound in the mixture is not the same as the non-bubbly case [14-17]. This means, if the sound speed and attenuation in a bubbly mixture are measured, these data can be inverted to estimate the number and size distribution of bubbles existing in the mixture can be derived under a set of stated assumptions. If for example we assume that:

- the gas volume fraction Γ is small such as $\Gamma \ll 1$;
- the shape of bubble is spherical;
- the perturbations in the radius of the oscillating bubble, ΔR , are small such that $\Delta R \ll R_0$ where R_0 is equilibrium radius of bubble;

then the resulting speed of sound in the mixture is as follows (the detail of the derivation of the equation is shown in Appendix C):

$$c_p \approx c \left[1 - 2\pi c^2 n_b R_0 \frac{\omega_0^2 - \omega^2}{(\omega_0^2 - \omega^2)^2 + 4\beta^2 \omega^2} \right], \quad (11)$$

If the bubbles are all of the same size and spherical, then the number of bubbles per unit volume, n_b , is related with the gas volume fraction Γ through $n_b = 3\Gamma / (4\pi R_0^3)$. In Eq. 11, ω_0 is resonance circular frequency, and β is the damping coefficient. Hence, sound speed in bubbly liquid is dependent on the void fraction (related to n_b), frequency (ω), bubble size (R_0), and damping coefficient (β). Here, damping coefficient β is described as the sum of thermal, radiation, and viscous damping coefficients, β_{th} , β_{rad} , and β_{vis} respectively. Several publications show the damping parameters as a function of the frequency or bubble radius [14-19]. Among them, the works by Commander and Prosperetti are adopted in the present report because they derived the equations in rigorous manner [14-16], although there is a typographical error which is corrected for in the calculations included in this report. A brief derivation and formulation are shown in Appendix C. The expressions to calculate damping coefficients require, as input, information of the hydrostatic pressure in the liquid, the ratio of specific heats of the gas in the bubbles, density of gas, the speed of sound and viscosity of the liquid. Figures 3.7 and 3.8 show the calculation of the total damping coefficients β as a function of frequency at given bubble radius of 10^{-3} and 10^{-4} cm respectively.

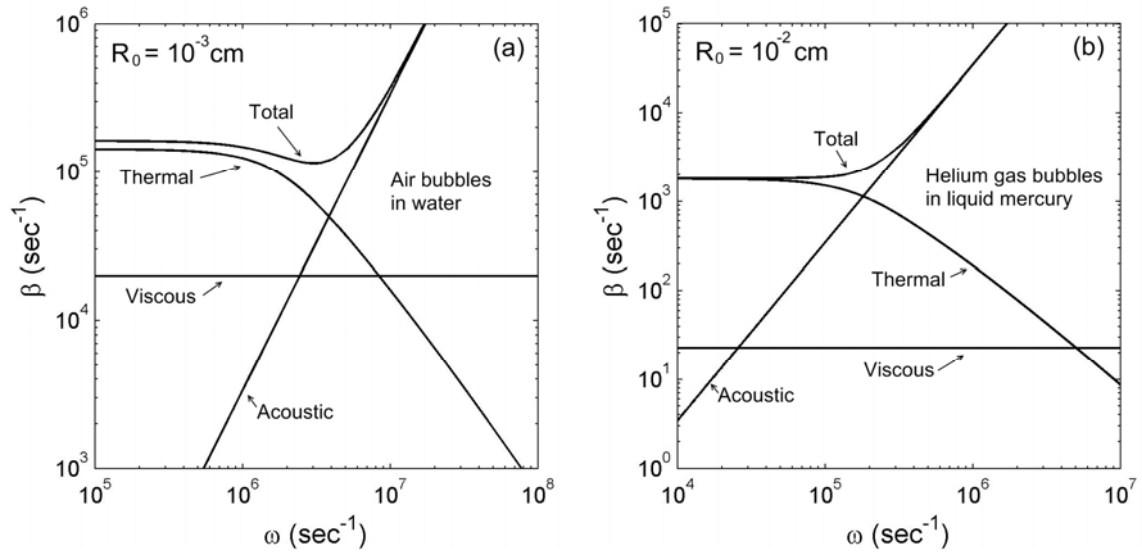


Fig. 3.7: Calculation of damping coefficients as a function of frequency (a) at a given bubble radius of 10^{-3} cm for air bubbles in water and (b) at a given bubble radius of 10^{-2} cm for helium gas bubbles in liquid mercury. Both calculations are done under 1 bar static pressure. Each contribution to the total damping by thermal, viscous, and acoustic effects are superimposed. Compare (a) with Fig. 10 in the reference [16]. Similar features of thermal, viscous, and acoustic damping in liquid mercury mixed with helium gas bubbles are observed in lower frequency range and bigger radius of bubbles than those in water mixed with air bubbles.

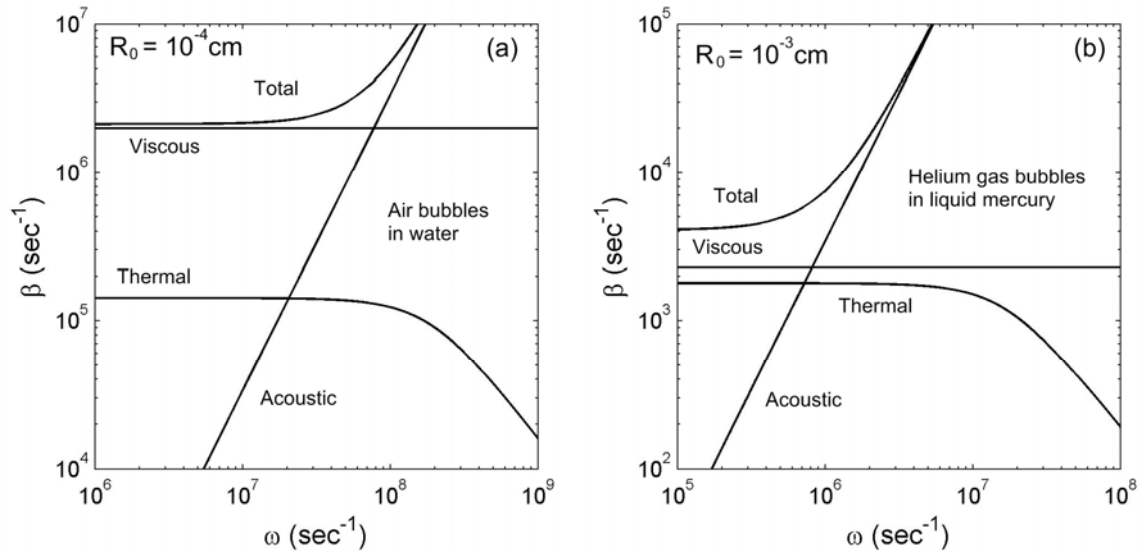


Fig. 3.8: Calculation of damping coefficients as a function of frequency (a) at a given bubble radius of 10^{-4} cm for air bubbles in water and (b) at a given bubble radius of 10^{-3} cm for helium gas bubbles in liquid mercury. Both calculations are done under 1 bar static pressure. Each contribution to the total damping by thermal, viscous, and acoustic effects are superimposed. Compare (a) with Fig. 11 in the reference [16]. Similar features of thermal, viscous, and acoustic damping in liquid mercury mixed with helium gas bubbles are observed in lower frequency range and bigger radius of bubbles than those in water mixed with air bubbles. Compare (b) with Fig. 3.7(a) which shows the same frequency range and bubble radius for the case of air bubbles in water.

As shown in Figs. 3.7 and 3.8, the thermal contribution to total damping is dominant in the low frequency regime for large bubbles, both for air bubbles in water and for helium gas bubbles in liquid mercury under 1 bar static pressure. In contrast, the viscous contribution to damping is constant through the frequency and more dominant for the small size of bubbles. Figures 3.7(a) and 3.8(a) simulated Figs. 10 and 11 in the corresponding reference [16]. These figures reproduce Figs. 10 and 11 in his paper. For the practical use of the corresponding expressions of Eq. (11) in the project, the same calculations were done for the liquid mercury mixed with helium gas bubbles in Figs. 3.7(b) and Fig. 3.8(b). At both graphs, it is obvious that the similar contribution to the total damping by thermal, viscous, and acoustic effects are observed at lower frequency range and bigger bubble radius. Figures 3.7(a) and 3.8(b) show the calculations done at the same acoustic excitation and the bubble radius. However, the pattern of the damping by thermal, viscous, and acoustic effects seen in the liquid mercury case, Fig. 3.8(b), is closer to Fig. 3.8(a) than Fig. 3.7(a).

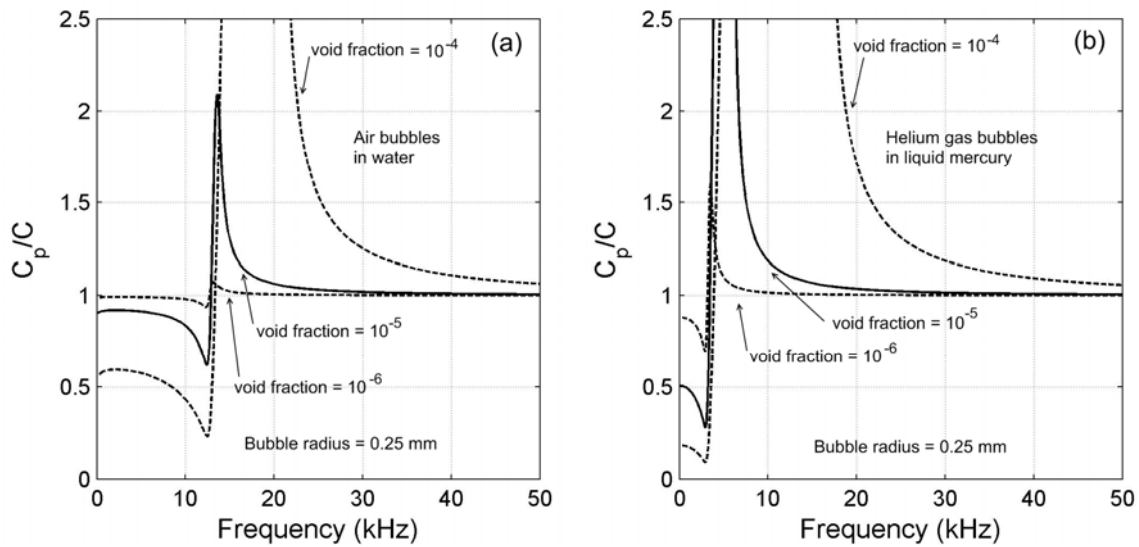


Fig. 3.9: Speed of sound in bulk bubbly liquid as a function of frequency for a given void fraction. Panel (a) is the calculation in water mixed with air bubbles and panel (b) is the calculation in liquid mercury mixed with helium gas bubbles. Bubble size was chosen as 0.25 mm of which corresponding resonance frequency is about 13 kHz for air bubbles in water and about 3.2 kHz for helium gas bubbles in liquid mercury. Each phase speed is normalized by the speed of sound in water (1480 m/s) or in liquid mercury (1451 m/s). These curves were obtained by a monodisperse bubble population under 1 bar static pressure. For a given bubble radius and void fraction, the change of the sound speed is more severe in liquid mercury case than in the water case.

Figures 3.9 and 3.10 show the calculated normalized phase velocity of sound in bulk bubbly liquid as a function of frequency or radius obtained from Eq. (11). Each figure indicates the effect of several different void fractions (noting that all populations are monodisperse, i.e. contain only one size of bubble). Each phase velocity is normalized with respect to the speed of sound in water (1480 m/s) or in liquid mercury (1451 m/s). Figures 3.9(a) and 3.10(a) are calculations for water mixed with air bubbles and Figs. 3.9(b) and 3.10(b) are calculations for liquid mercury mixed with helium gas bubbles. Figure

3.9 shows the change of the phase speed for a given bubble radius of 0.25 mm. It is clear that the change is bigger in liquid mercury compared to water, and the resonance frequency of the helium gas bubbles in liquid mercury is predicted to be at a lower frequency than for air bubbles in water.

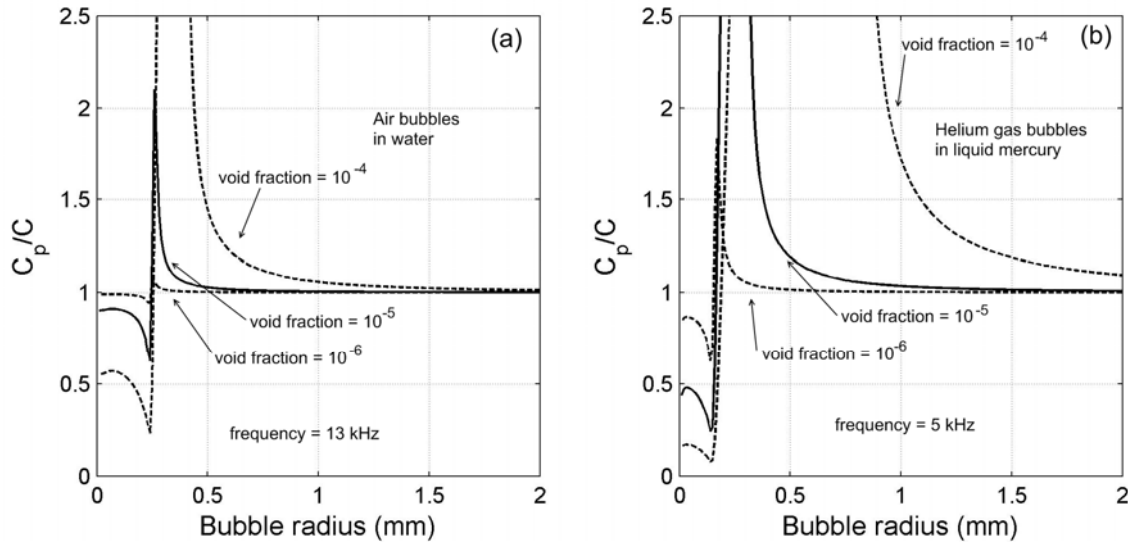


Fig. 3.10: Speed of sound in bulk bubbly liquid as a function of bubble radius for a given void fraction. (a) is the calculation in water mixed with air bubbles at 13 kHz of acoustic excitation and (b) is the calculation in liquid mercury mixed with Helium gas bubbles at 5 kHz excitation. Like Fig. 3.9, these curves were obtained for a monodisperse bubble population under 1 bar static pressure. For a given acoustic excitation and void fraction, the change of the sound speed is more severe in liquid mercury case than in water case.

As shown in Figs. 3.9 and 3.10, the change in sound speed caused by the presence of bubbles is strongly dependent upon the void fraction. In such sound speed plots for a monodisperse bubble population (i.e. where all bubbles have the same size), the resonance frequency is determined by finding the frequency which gives the normalized velocity as unity because the calculation converges to 1 as frequency approach the resonance frequency as shown in Eq. (11). The resonance frequency associated with the bubbles in Fig. 3.9 is around 13 kHz.

When the oscillation frequency of the forcing pressure wave is larger than the resonance frequency of the bubble, the presence of the bubble tends to raise the sound speed in the bubbly liquid to values which are greater than the sound speed in pure water. At the highest driving frequencies, the bubble has no effect on the sound speed (but can strongly affect the attenuation). At the opposite end of the frequency spectrum, as the driving frequency approaches DC the sound speed is reduced by the bubble, and as the frequency increases towards resonance this reduction tends to increase until we approach the through-resonance conditions.

This behaviour is due to the effect of the bubbles on the compressibility of the mixture (the effect of the bubbles on the density is, at these void fractions, of lesser importance). The square of the sound

speed is proportional to the bulk modulus which is the inverse of the compressibility. This means that (for as given medium density) the more compressible material, the slower the sound speed of the propagating wave inside the material. Suppose the pure water contains bubbles which have the same equilibrium radius (a monodisperse population). The radius of the bubble determines the resonance frequency of the bubble, ω_0 . If driving frequency of the pressure is less than the resonance frequency, the response of the bubble is in phase with the driving pressure, in that the bubble is compressed during the compressional half-cycle of the driving pressure, and expands during the rarefaction half-cycle. As a result, the bubbly liquid compresses well, i.e. has a high compressibility and a low sound speed. If one increases the driving frequency from DC, the bubble volume changes become greater as the pulsation amplitude increases as one approaches resonance. Consequently, at DC, the sound speed in the bubbly water is less than the speed of sound in pure water, and remains so for $\omega < \omega_0$ until one approaches resonance.

However as the driving frequency increases towards resonance, the phase relationship between the bubble pulsation and the driving field changes and, being an oscillator, a phase change of π must occur as one moves from DC to very high frequencies. At driving frequencies greater than resonance ($\omega > \omega_0$), this $\sim \pi$ phase change between the pressure and the response of the bubble means that the bubbles expand during the compressive half cycle of the driving field, and bubble contract during the rarefaction half-cycle. The presence of the bubbles make the bubbly liquid more stiff (i.e. less compressible) than bubble-free water, and sound the presence of bubbles increases the sound speed above resonance. At very high frequencies the bubble pulsation amplitude is very small, as the bubble does not have time to respond to the driving field, and so the bubbles have little effect on the sound speed. The effect at very high and very low frequencies is therefore very different, because even though both are far from resonance, at low frequencies the pressure changes in the driving field occur on a much slower timescale than that associated with the natural frequency of the bubble. This explains the general shape of Fig. 3.9, which is for a monodisperse bubble population [20]. When there are bubbles of many sizes present (a ‘polydisperse’ population), the effects are broadly similar [21]. This is discussed in the next section.

If one wishes to predict the sound speed in a bubbly liquid, it is therefore important to know the bubble size distribution unless the drive conditions are at very low frequency (in which case only the void fraction need be known). If one wishes to invert the measured sound speed to determine the bubble population, a range of frequencies covering the main bubble resonances is required, unless one uses only very low frequencies (in which case only the void fraction can be determined) [22].

Figure 3.10 can be also interpreted with the same way as Fig. 3.9 was interpreted. For a given driving frequency, it is a simple matter to calculate which bubble size is resonant. The resonance frequency is inversely related with the equilibrium bubble radius R_0 . At the right side of Fig. 3.10, for large bubbles the resonance frequency is less than a given driving frequency. The bubble dynamics, and effect on the sound speed, are therefore analogous to the above discussion for Fig. 3.9 when a

bubble is driven by a sound field which has a frequency greater than the bubble resonance frequency. Since the compressibility becomes smaller under these conditions (as explained previously), the resulting sound speed becomes supersonic. In the opposite case, sound speed becomes subsonic when bubbles are smaller than the size that would be resonant with the driving field.

III-3. Speed of sound in bulk bubbly media – mixed distribution

Figures 3.9 and 3.10 only describe the effect on the sound speed of a monodisperse bubble population, as illustrated in Eq. (11). In most cases, the population is polydisperse (i.e. it many bubble sizes). When a distribution of bubble sizes is considered, Eq. (11) is modified as a sum of the bubble density with respect to the equilibrium radius R_0 such as:

$$c_p \approx c \left[1 - 2\pi c^2 \int_{R_0=0}^{\infty} \frac{(\omega_0^2 - \omega^2)f(R_0)R_0 dR_0}{(\omega_0^2 - \omega^2)^2 + 4\beta^2\omega^2} \right], \quad (12)$$

where $f(R_0)dR_0 = dn_b$ is the number of bubbles per unit volume with equilibrium radius between R_0 and $R_0 + dR_0$. In most circumstances, dR_0 is set equal to 1 μm . Since any one technique for determining the bubble spectrum contains ambiguities and is limited in the radius range where it is accurate, this project will use several methods (using acoustics and optics) combined together to measure the bubble spectrum, following the COBUST principle (Characterization Bubbles Using Simultaneous Techniques) [2, 23-24].

Figure 3.11 shows an example of the measurement of the number of bubbles in different radius bins inside the static rig shown in Fig. 5.2. This measurement was obtained by the optical fiber method described in Appendix D. Bubbles were introduced through the hole of the small needle at the bottom side of the vertical tube filled with water. As bubbles rise up in the tube, this number distribution of bubbles varies since bubbles suffer from coalescence during rising, their overall volume increases as the hydrostatic pressure is reduced, and the larger bubble rise through buoyancy more quickly than the smaller ones. Three different positions inside the tube were selected to show the change of the distribution. The results show that the population tends to contain a greater proportion of larger bubbles the higher up the water column is the detector. Figure 3.11 was converted into the form of the bubble spectrum $f(R_0)$ as shown in Fig. 3.12.

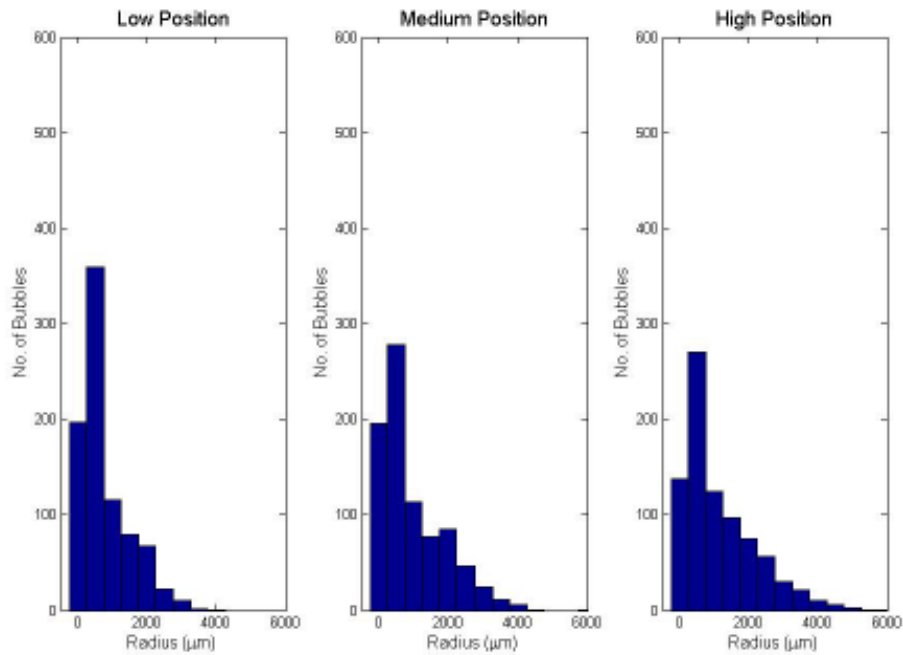


Fig. 3.11: Number of bubbles as a function of the bubble radius. Three different position inside the tube was selected to show the change of the bubble distribution as a function of the position. This distribution was measured through the optical fiber method. Length of the water column inside the tube is about 1.8 m and the needle is far from the base of the tube by 18 cm. Positions ‘High’, ‘Medium’, and ‘Low’ are located about 150 cm, 110 cm, and 70 cm above the needle respectively. All the measurements were done in the center of the tube at each position.

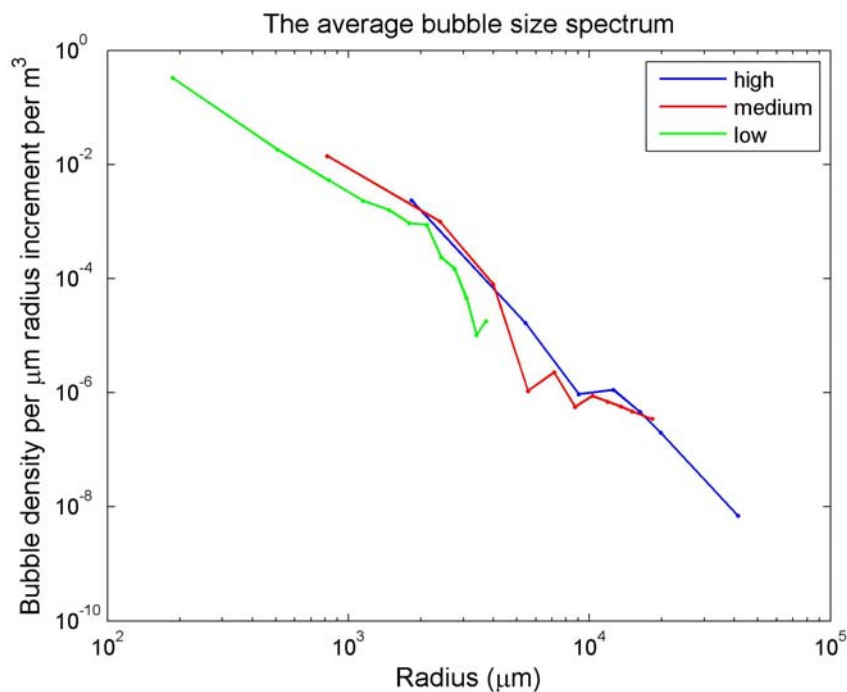


Fig. 3.12: Bubble density as a function of the bubble radius. Note that conversion of the discrete count in Fig. 3.11 into a continuous count (Fig. 3.12) creates some issues when only small numbers of bubbles are detected, as Figure 3.11 cannot record less than one bubble in a bin, but the continuous distributions such as Fig. 3.12 can readily be extrapolated to indicate what fraction of a bubble might be expected in the measurement volume

When bubble spectrum shown in Fig. 3.12 was used as input for Eq. (12), the resulting phase velocities in the mixture are shown in Fig. 3.13, which plots the normalized sound speed as a function of the frequency. Three different measurement positions are represented using the same colours shown in Fig. 3.12. The calculated sound speeds show that the change of the speed is the biggest in the high position of the tube and the least in the low position of the tube. The corresponding gas volume void fractions calculated from Fig. 3.12 are about $5.7 \times 10^{-6} \%$, $3.5 \times 10^{-5} \%$, and $9.5 \times 10^{-5} \%$ for the low, medium, and high positions respectively in the tube. Thus this example shows the effect of bubbles on the speed and attenuation coefficients when gas volume void fraction in the media is low.

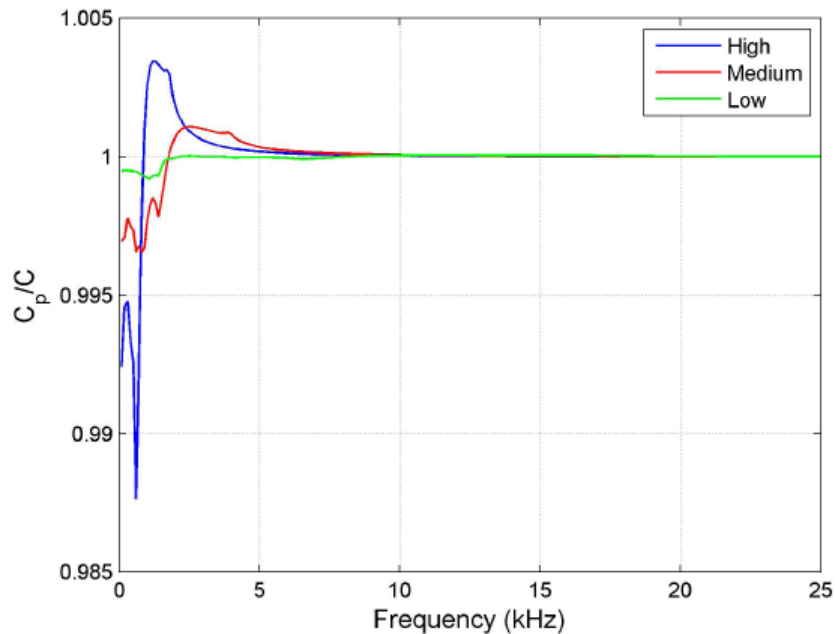


Fig. 3.13: Speed of sound in bubbly water as a function of frequency. This calculation was based on the measurement of the bubble spectrum shown in Fig. 3.12. Although the population was measured in a pipeline, the underlying theory assumes that the bubbles exist in an infinite body of liquid.

Figure 3.14 shows another bubble size spectrum, an example where there exist far more bubbles than the previous case. The spectrum was obtained through the photographic method illustrated in Appendix E. Comparing this with Fig. 3.12, the bubble density in this figure is at least 1000 times larger than that in Fig. 3.12. The gas volume void fraction calculated from this picture is 0.97%. Thus, the effect of this bubble density on the speed of sound is significant, as shown in Fig. 3.15.

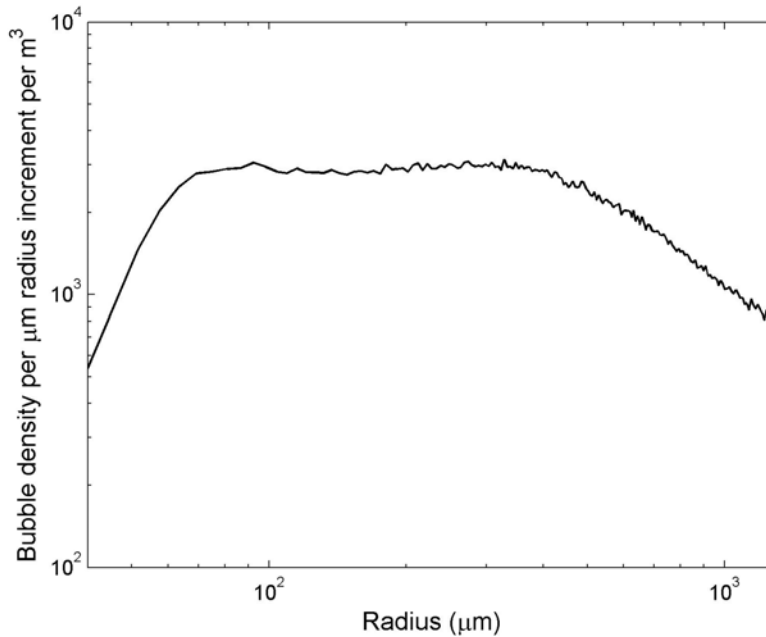


Fig. 3.14: Bubble density spectrum obtained by the photographic method. This reflects the case when there exist many bubbles in the medium. Compare this with Fig. 3.12 (less bubble case). The order of magnitude of this picture is at least 1000 times larger than that of Fig. 3.12. The corresponding gas volume void fraction in this figure is 0.97%.

Figure 3.15 shows the calculated phase speed of sound in bulk bubbly water as a function of frequency obtained from the bubble distribution shown above. The dashed line denotes the speed of sound in pure water (c) and it is located at the value of 1480 m/s. Comparing this with Fig. 3.13 (the case for a lower void fraction), it is clear that the presence of many bubbles (0.97% void fraction) changes the sound speed such that the minimum value is as low as $0.08c$ and the maximum value is as high as more than $3c$ (where c is speed of sound in pure water). This can be contrasted to the case when the void fractions are much lower (Figure 3.12; $9.5 \times 10^{-5}\%$ for high position, $3.5 \times 10^{-5}\%$ for medium position, and $0.57 \times 10^{-5}\%$ for low position), such that the effect is less (Figure 3.13): the speed of sound takes a minimum value of $0.987c$ and a maximum of $1.0003c$, perturbations which are much less than those seen at the higher void fraction. The DC sound speed reduction should scale with void fraction [22].

The real situation in the test rig may not encounter gas volume void fractions as high as 1%. However, clearly even small concentrates of bubbles can change the sound speed considerably. If this change can be predicted and validated, and is sufficiently large but also sufficiently robust, then measured sound speeds can be inverted to estimate the bubble size distribution. This is a relatively straightforward technique for bubbles in the bulk of a fluid, although usually it is more reliable to measure the attenuation [21]. This is discussed in the next section.

As a closing note, the theory presented in this section (and the following one) assumes that the bubbles existed in an infinite 3D volume of liquid. What complicates the situation here is that the

bubbles exist in a pipe, and the bubble-free sound speed there is not a simple fixed value as it is in the bulk, but multi-valued and complicated by the phenomena discussed in Section III-1.

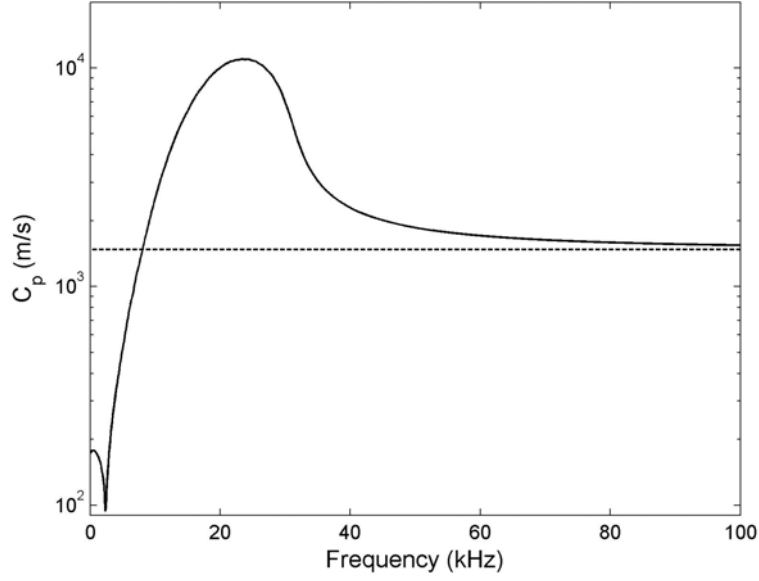


Fig. 3.15: Calculated phase velocity of sound propagating in bulk bubbly water as a function of frequency. Dashed line shows the speed of sound in pure water. This calculation was done based upon the bubble spectrum shown in Fig. 3.14. Although the population was measured in a pipeline, the underlying theory assumes that the bubbles exist in an infinite body of liquid.

III-4. Attenuation coefficients

The attenuation coefficient in polydisperse bubbly water can be calculated from the imaginary part of the sound speed:

$$\frac{c}{c_p} \approx 1 + 2\pi c^2 \int_0^\infty \frac{f(R_0)R_0}{\omega_0^2 - \omega^2 + 2i\beta\omega} dR_0, \quad (13)$$

Because $c/c_p = k_z/k$ (where k_z is the wave vector in the bubbly media), splitting $k_z = k_z^R - ik_z^I$ into the real part and the imaginary part allows the following relations to be obtained:

$$\begin{aligned} \frac{k_z^R}{k} &= 1 + 2\pi c^2 \int_0^\infty \frac{(\omega_0^2 - \omega^2)f(R_0)R_0}{(\omega_0^2 - \omega^2)^2 + 4\beta^2\omega^2} dR_0, \\ \frac{k_z^I}{k} &= 4\pi c^2 \int_0^\infty \frac{\beta\omega f(R_0)R_0}{(\omega_0^2 - \omega^2)^2 + 4\beta^2\omega^2} dR_0, \end{aligned} \quad (14)$$

Hence, a propagating wave in the bubble media suffers from the attenuation as a function of $\exp(-ik_z^I z)$ where z is propagation length. Usually, the attenuation coefficient A is defined in dB scale per unit length and it can be expressed as:

$$\begin{aligned} A &= 20 \log_{10} \left[\frac{e^0}{e^{-k_z^I z}} \right] = 20k_z^I \log_{10}(e) \\ &= 80\pi c \log_{10}(e) \left[\int_0^\infty \frac{\beta\omega^2 f(R_0)R_0}{(\omega_0^2 - \omega^2)^2 + 4\beta^2\omega^2} dR_0 \right]. \end{aligned} \quad (15)$$

Thus the attenuation coefficient can also be calculated from a known bubble spectrum. Taken together, Eqs. (12) and (15) allow calculation of how the presence of bubbles changes the sound speed and causes attenuation. The inverse problem can also be achieved: measurement of the sound speed and the attenuation coefficients provide us the clues to estimate bubble distribution present. This can be done relatively easily for bubbles in an infinite body of liquid, but has not previously been achieved for confined bubbles, as occurs in the tube.

If we assume the bubbles counted in Figs. 3.11 and 3.14 were to exist in an infinite 3D body of liquid, the attenuation can be calculated from Eq. 3.15. The bubble spectra used in the calculation of the sound speed in Fig. 3.12 is used to calculate the attenuation in Fig. 3.16(a), and the spectra for which Fig. 3.14 shows the sound speed is used as input in Eq. (15) to calculate the attenuation in Fig. 3.16(b). Each colour in Fig. 3.16(a) corresponds to the colour of the bubble spectra shown in Fig. 3.12. There is a peak in attenuation associated with the main resonance of the population. Although it was not shown here, at high frequency limit, the attenuation coefficients in Fig. 3.16(b) reduce at the high frequency limit as with the other graphs in Fig. 3.16(a). However it must be recalled that this prediction is based on a long-wavelength theory, and as bubble sizes increase that theory will break down, commensurate with the massive scattering losses which large bubbles generate (as the bubble radius increase without limit, it tends to a pressure-planar release surface). In the frequency band around resonance, there is high attenuation. Those frequency bands are obvious in Fig. 3.16(a). At the measurement position which is termed ‘high’, the bandwidth of the attenuation peak is narrow, whilst it is widest at the pipe position termed ‘low’. As illustrated in the bubble spectrum, at the ‘high’ there is a greater number of big bubbles compared to ‘low’ position. In other words, smaller bubbles in the media cause a wider frequency band (in terms of Hz rather than octaves) in which this high attenuation occurs. This is a natural outcome of the fact that the natural frequency of a bubble is roughly inversely proportional to its radius. It does indicate how inversion of the measured attenuation can have the potential to estimate the sound speed, a calculation which has been achieved many times using the assumption that the bubbles in a large body of liquid, but which has not yet been achieved for bubbles in a confined space like the pipeline.

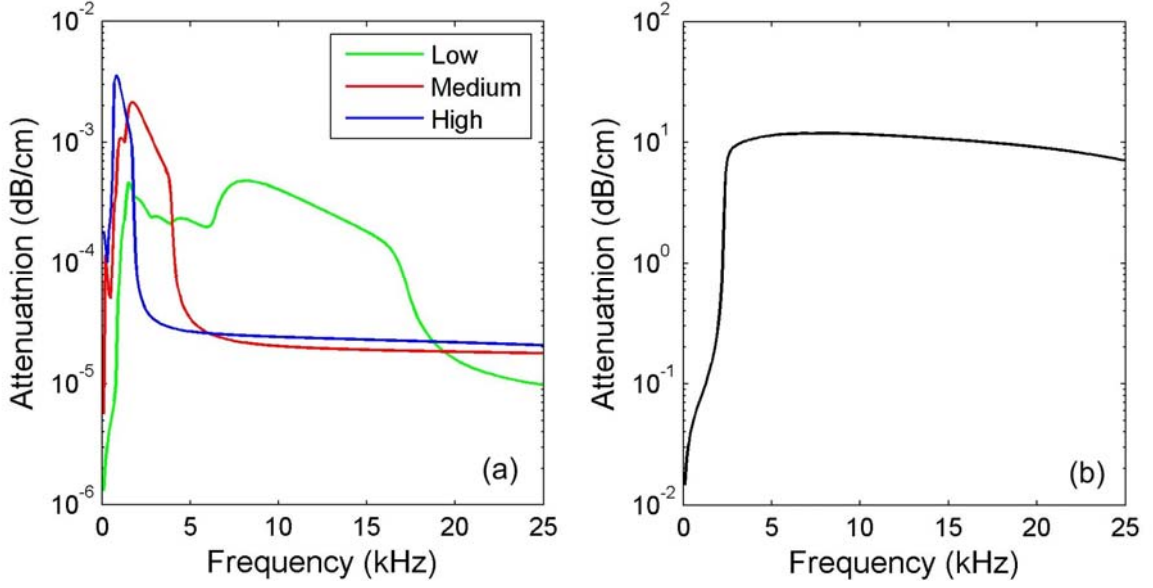


Fig. 3.16: Attenuation coefficients in bulk bubbly water as a function of frequency. (a) and (b) are calculated from bubble density spectrum in Fig. 3.12 and Fig. 3.14 respectively. Although the population was measured in a pipeline, the underlying theory assumes that the bubbles exist in an infinite body of liquid.

III-5. Estimating the bubble distribution by acoustic inversion

From Eqs. (13) and (14), if either the dispersion relation or the attenuation coefficient is measured, the bubble density can in principle be inferred by linear inversion in the matrix problem. In many cases the measurement of inversion tends to be more robust, since small changes (e.g. in hydrophone spacings caused by hydrodynamic vibration of the hydrophone mounts) can generate large error in measurements of the sound speed. Although Eq. (14) is expressed in the form of the integral with respect to the continuous space of bubble radius R_0 , for numerical manipulation the radius representation is not continuous but sampled. Hence, at sufficiently narrow sampling interval of bubble radius, Eq. (14) can be rewritten as:

$$k^l \approx \sum_a^N D_a f(R_{0a}), \quad D_k = \frac{4\pi c \beta(R_{0a}) \omega^2 R_{0a} \Delta R_0}{(\omega_0^2(R_{0a}) - \omega^2)^2 + 4\beta^2(R_{0a}) \omega^2}, \quad (16)$$

where N is number of samples and a is index which indicates sampling point. This can be expressed in terms of matrix equation in terms of α , D , and f which indicate matrix composed of k^l , D_a , and $f(R_{0a})$ respectively. Their relationship is linear as follows.

$$\alpha = Df, \quad (17)$$

In the above equation, when the measurement of the attenuation coefficient as a function of

frequency, α is known, bubble distribution density f can be easily calculated through linear algebra. But, the problem of this method is in the correctness of the solution. Although each matrix is linearly related with each other, it is common to find that the *problem of linear inversion* is *ill-posed*. In order to resolve this ill-posed problem, the process of regularization is necessary [21, 25-27]. In the present study, a method of regularization is chosen as Tikhonov regularization [26-27] is explained briefly as follows. Defining error e and a corresponding composite cost function ψ such as:

$$e = \alpha - Df, \quad \psi = e^T e + \lambda f^T f, \quad (18)$$

where superscript T represents transpose of matrix, regularization can be done by minimizing this cost function with respect to f . Thus, the optimized bubble distribution f_{opt} is obtained as:

$$f_{opt} = (D^T D + \lambda I)^{-1} (D^T \alpha), \quad (19)$$

where I is identity matrix and the scalar parameter λ controls the amount of regularization. This parameter can be found by investigating the norm of the regularized solution, $\|f_{opt}\|$ versus the corresponding residual norm $\|e\|$ [21]. The optimal value of λ is chosen as the value which gives the maximum curvature of $C(y)$ given by

$$C(y) = \frac{|z''|}{(1 + z'^2)^{3/2}}, \quad (20)$$

where $z = \|f_{opt}\|$ and $y = \|e\|$ and the derivatives is done with respect to y .

III-6. Conclusions

The aim of this project is to develop detection techniques, some of which are acoustic, for bubble populations in a pipeline. This project detailed two opposite ends of the problem which are already covered in the literature. The first (Section III-1) is the propagation of waves in a pipeline, where the pipe contains no bubble in the fluid. Several modes are observed, with dispersive wavespeeds that differ from those seen in an infinite body of liquid. The later Sections III-2~III-4 dealt with the opposite problem that of calculating the sound speeds and attenuation in an infinite 3D volume of

bubbly liquid. It is in the region between these two well-characterised extremes that this project must investigate. The following section will report on numerical studies which were undertaken to see if the modes for a bubble-free pipe that were formulated in Section III-1, can be identified in simulations, as a preparatory route to exploring if such simulations can be extended to cover the case of bubbles in pipes.

IV. NUMERICAL STUDY USING FINITE ELEMENTS

IV-1. Motivation

There are three motivations for using a numerical simulation method in this project:

- First, our preliminary experimental results for the measured wave speed in the pipe show slight difference from the theoretical prediction of Section III-1. There are many potential reasons for this, which should be explored to ensure that future predictions are reliable. One obvious reason could be that the theoretical study is based upon simplified geometrical dimensions and an infinite propagation condition, but the practical situation more complicated (using, for an example, a tube of finite length). Numerical simulation provides a valuable tool to bridge the gap between the theoretical and experimental studies.
- Second, the numerical study can test the experimental and processing methods before using them. This advantage makes it an effective way to design the experiment.
- Third, for this project, our experiment will be conducted in a water-based test rig. However, the measurement system is expected to be used in a mercury-based system which has different characteristics. A numerical study is helpful to achieve this transfer successfully.
-

IV-2. Verify the correctness of theoretical analysis

Here, a numerical study is carried out using a finite element method. An axisymmetric model is used in the study in the same manner as employed in the theoretical analysis of Section III-1. Two cases are investigated:

- (i) First, to make sure that the numerical method can give us a reasonable result, the sound propagation inside a pure water column, 1.8m in length and 0.045m in radius, is simulated.
- (ii) Second, the water column is coupled to the PMMA (Perspex) tube which has a thickness of 0.005m by giving same pressure and acceleration at the coupling interface. All the geometrical dimensions used are from the practical measurements as shown in Figure 4.1.

An impulse source is simulated at bottom boundary of the water ($z = 0$). This impulse signal propagates through water and tube to the top boundary ($z = 1.8$ m). The pressure changes in both water and tube are calculated in time domain from 0 to 1 ms. By recording the pressure changes at the centre positions of the water column along z direction, a pressure map can be drawn in time-distance domain as shown in Figures 4.2 (a) and (b).

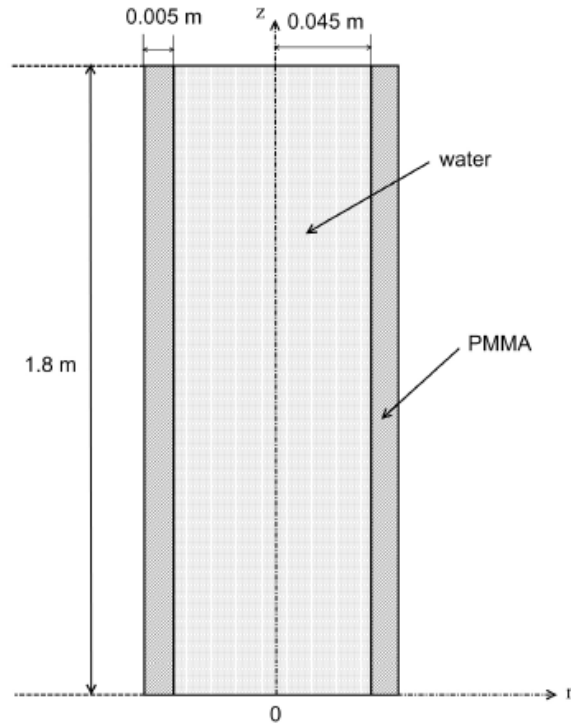


Figure 4.1: Schematic diagram of the water-filled PMMA tube (It is not drawn in scale).

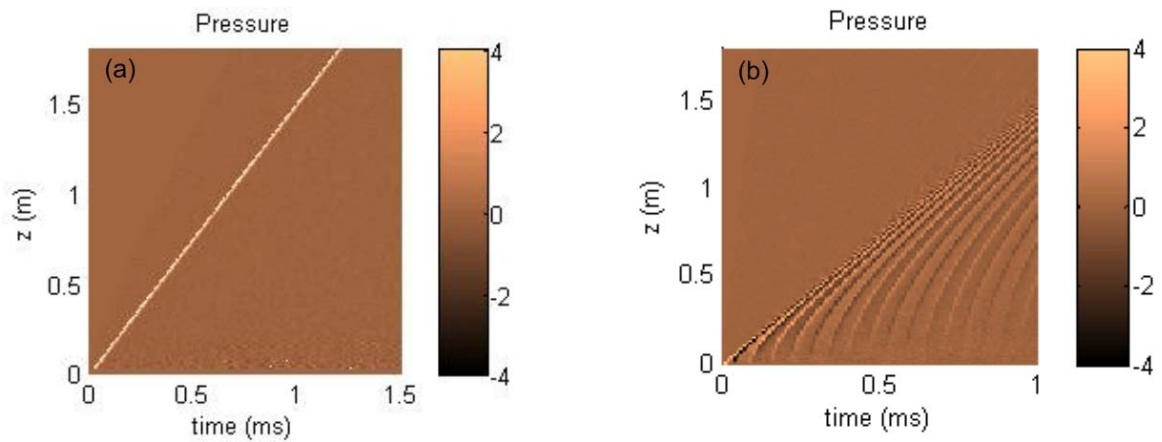


Figure 4.2: Pressure change in water (a) without coupling and (b) with coupling with the tube.

Figure 4.2 shows the pressure map for pure water column and water-filled PMMA tube. There is an obvious peak trace showing in both Figs 4.2(a) and 4.2(b). For the pure water column case (Fig. 4.2(a)), the acoustic signal has a constant speed of sound for different frequencies, because the pure water is a non-dispersion media. The group velocity equals to phase velocity in that case. Therefore, the sound

velocity can be obtained by calculating slope of the highlighted trace Fig. 4.2(a) directly. However, in the water-filled tube (Fig. 4.2(b)), dispersion occurs due to the coupling between tube and water. Phase velocity and group velocity may not be the same in that case. The slope of the highlighted trace in Fig. 4.2(b) just shows the group velocity band which has the maximum energy.

To investigate the sound velocity in a dispersion medium, one of the most accurate methods is the so-called wave number and angular frequency domain analysis ($k - \omega$) method which converts the pressure map to wave number and angular frequency domain by using a 2 dimensional Fourier-transform and highlights the potential propagation modes. As we know, the phase velocity is defined as $c_p = \omega/k$ and the group velocity is defined as $c_g = d\omega/dk$. Therefore, in $k - \omega$ domain, the value of every vertical coordinates on the highlighted trace divided by the value of the every horizontal coordinates equals phase velocity of that mode on that frequency, and the instantaneous slope of that position shows the relative group velocity.

Figure 4.3 show the 2-dimensional spectra of Figure 4.2. The coordinates used here is $k/2\pi$ and frequency, which are $1/2\pi$ multiple of wave number and angular frequency. Propagation modes are highlighted in these figures. In Figure 4.3 (a), the pure water column case (i.e. where no coupling is allowed between the water and the tube walls), only one obvious mode shows up, which is marked as EM1 (The term EMm is used to discriminate the mode obtained through the simulation with the mode ETm obtained through the theory). However, in Figure 4.3 (b), where the water is coupling to the tube, there are 3 modes, EM1, EM2 and EM3, are highlighted.

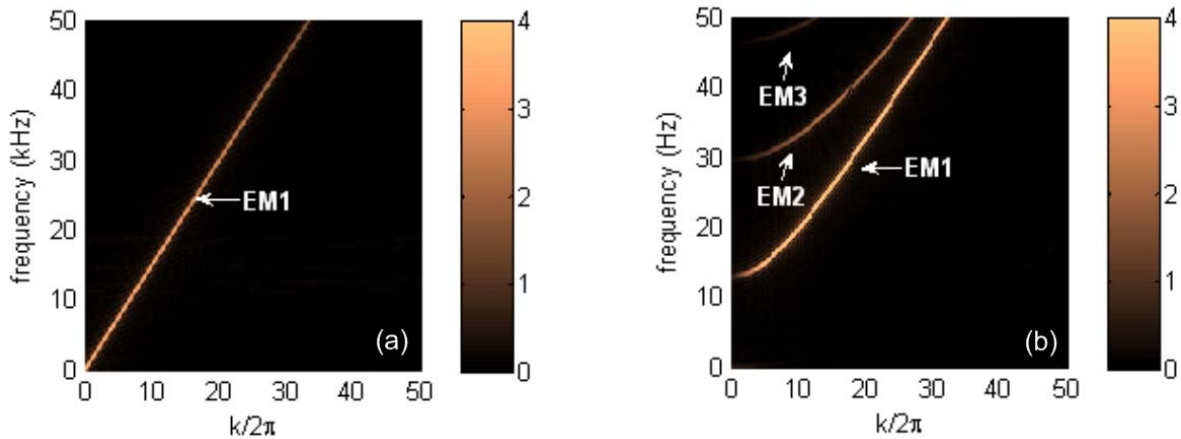


Figure 4.3: 2D pressure spectra in water (a) without coupling and (b) with coupling with PMMA tube. Color scale shows the absolute value of pressure spectrum

For the pure water case, the two velocities are shown in Figs. 4.4 (a) and (b).

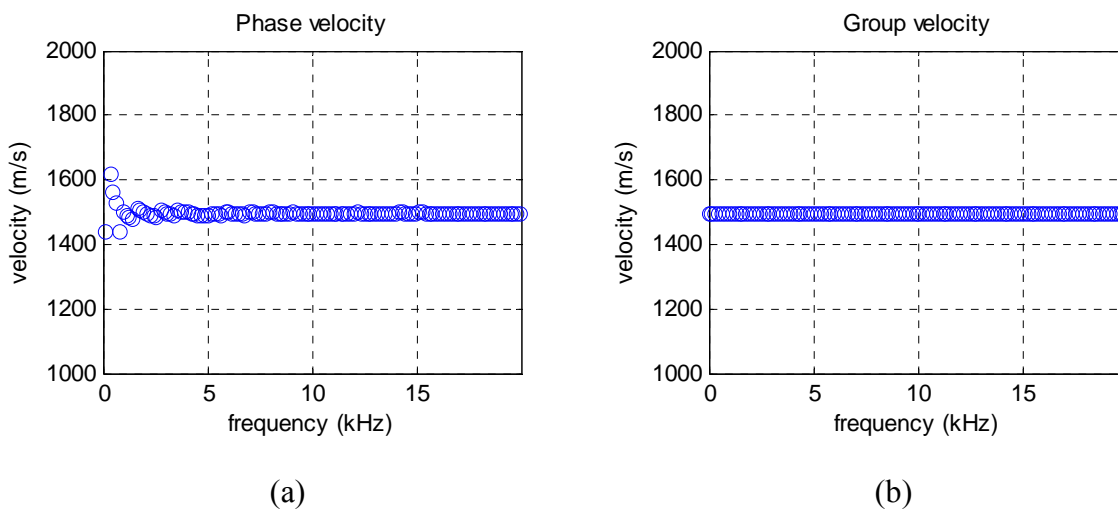


Figure 4.4: (a) Phase and (b) group velocities in water column

From Figure 4.4, both of the two velocities have a constant value in frequency domain. The phase and the group velocities are 1491 m/s and 1492 m/s respectively. They are nearly equal to each other and very close to the intrinsic velocity in the water (which is taken to be 1500 m/s in the simulation input parameters). This coherence means the medium is non-dispersive which is true for pure water. When the coupling is involved, results are shown in Figure 4.5.

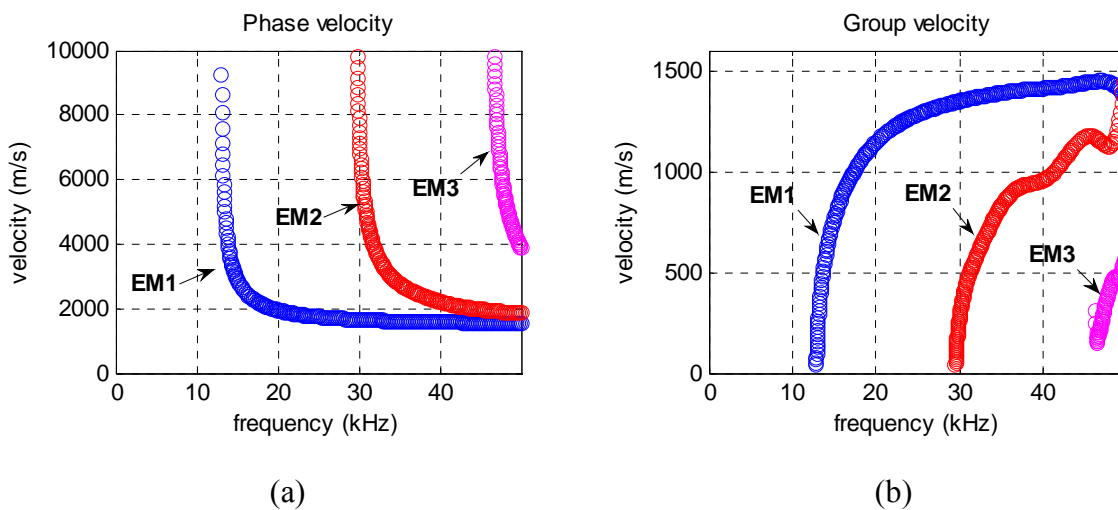


Figure 4.5: (a) Phase and (b) group velocities in water column coupled with PMMA tube.

From the Figure 4.5, three modes are picked up. Their velocities vary in frequency domain, which means that the coupling between the water and the tube causes dispersion.

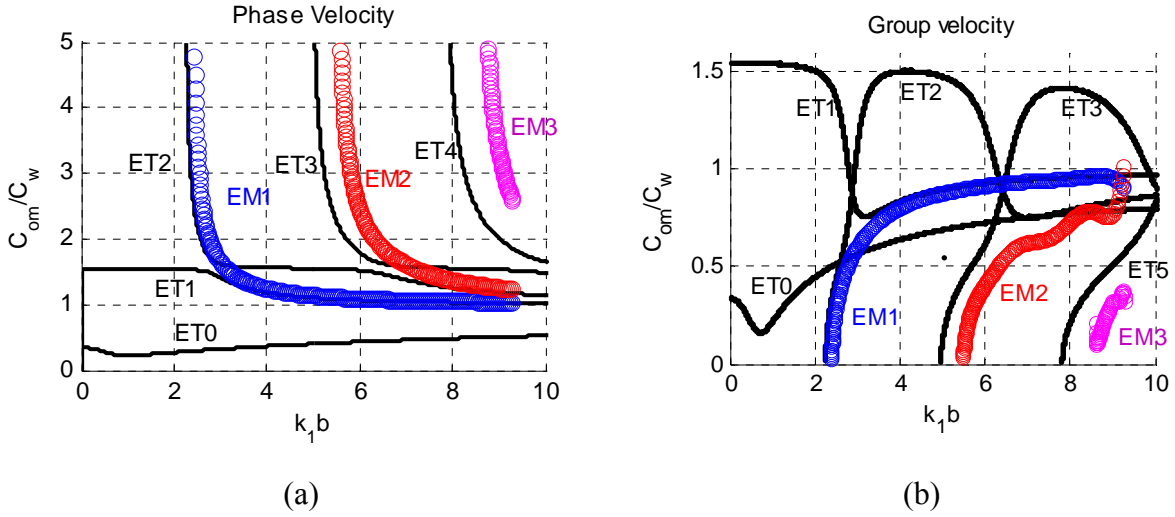


Figure 4.6: Theoretical (solid lines) and simulated (circles) results.

The simulation results are compared to theoretical results in Fig. 4.6. The first simulation mode (blue circles) matches to the ET1 theoretical mode when k_1b is larger than 3 and to the ET2 mode when k_1b is less than 3. The second simulation mode (red circles) matches to ET2 theoretical mode when k_1b is larger than 8 and to ET3 mode when k_1b is less than 8. This interesting phenomenon, where one simulation mode maps onto different parts of two theoretical modes, is exactly what we found in the experimental study and confused us at first: the numerical study enabled us to see physically what was behind this initially puzzling measurement.

To investigate this potentially confusing issue in more depth, we increased the number of samples taken along the tube and gave a much stronger excitation, conditions which are difficult to achieve in experiment. One result is shown in Figure 4.7. From Figure 4.7, we found there is an inconspicuous connection (circled by white line) between the EM2 and EM3 modes. That means the previous estimations using experimental and simulation results incorrectly separated these two parts into two different modes, because their connection is not noticeable. However, theoretically analysis can successfully find this weak connection by adjusting the searching range of (8). This resolves what at first we had taken to be a mismatch between the experimental measurements (Section V) and the predictions of the theory of Section III: using the simulations, we can see that there is in fact no discrepancy, and that they theory is accurate at predicting propagation (at least in a bubble free pipe).

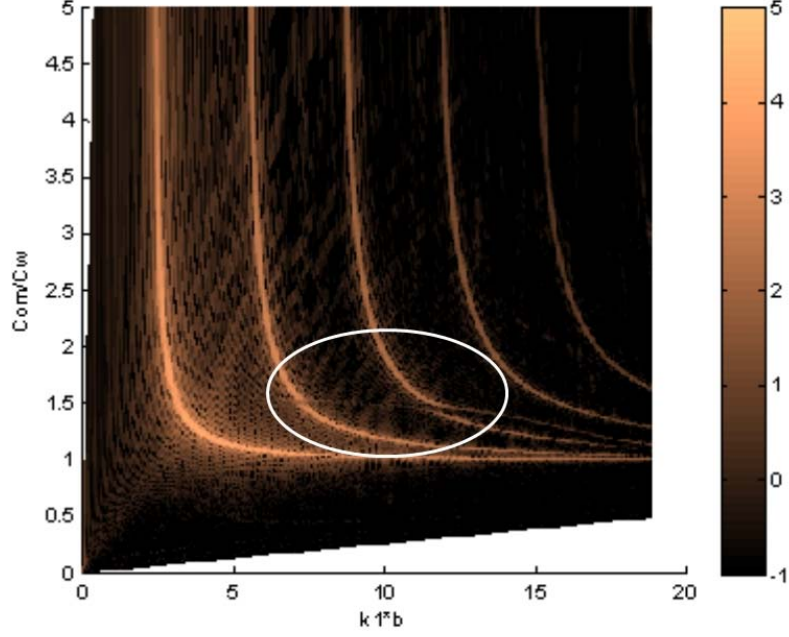


Figure 4.7: 2D pressure map highlighting the simulation modes.

IV-3. Test the methods used in experimental study

We have introduced the $k - \omega$ domain method in the last section, and used it to highlight the propagation modes. It can give us a very clear dispersion trace for each propagation mode, but it needs many measurement positions along the pipe to increase the resolution in the k domain.

There are also alternative methods to get the phase velocity and group velocity. For the phase velocity measurement, a phase spectrum (PS) method is widely used. Importantly, this method does not require full scan of the water from the bottom to the interface. If the wave is plane wave, the acoustic pressure obtained in z direction can be written as:

$$p(z, t) = \int_{-\infty}^{+\infty} \tilde{p}(f) e^{-\alpha(f)} e^{j2\pi f[t - z/c_p(f)]} df \quad (21)$$

where $\tilde{p}(f)$ is the time Fourier transform of acoustic pressure, $\alpha(f)$ is the attenuation coefficient, $c_p(f)$ is the phase velocity. By taking the acoustic signal in two positions, z_1 and z_2 , the phase velocity and attenuation coefficient can be obtained as:

$$\begin{aligned}
c_p(f) &= -\frac{2\pi f(z_2 - z_1)}{\text{Arg} \left[\frac{\tilde{p}(z_2, f)}{\tilde{p}(z_1, f)} \right]} \\
\alpha(f) &= -\frac{\ln \left[\frac{\tilde{p}(z_2, f)}{\tilde{p}(z_1, f)} \right]}{z_2 - z_1},
\end{aligned} \tag{22}$$

where $\text{Arg}[\tilde{p}(z_2, f)/\tilde{p}(z_1, f)]$ is the phase difference between the two signals recorded in z_1 and z_2 . This method does not need as many measurements as the k - ω method needs, but it has a problem in that the phase repeats every 2π . That means the phase difference always has an ambiguity of $2n\pi$ (where n is an integer). To overcome this problem, a time delay can be introduced to shift the two signals into one wavelength. Here, this time delay τ is obtained by checking the cross-correlation of these two signals. Then the second signal is shifted to:

$$q(z_2, t) = p(z_2, t + \tau). \tag{23}$$

The new signal's temporal Fourier-transform is:

$$\tilde{q}(z, f) = \tilde{p}(z, f)e^{j2\pi f\tau}. \tag{24}$$

Then the phase velocity can be expressed as:

$$c_p(f) = -\frac{2\pi f(z_2 - z_1)}{\text{Arg} \left[\frac{\tilde{p}(z_2, f)}{\tilde{p}(z_1, f)} \right] - 2\pi f\tau}. \tag{25}$$

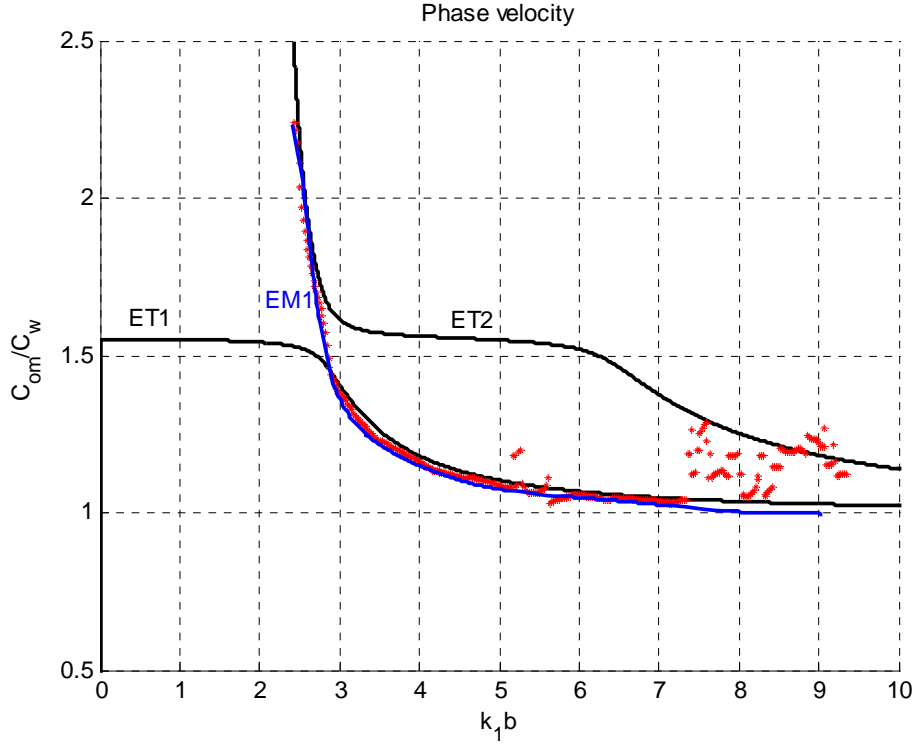


Figure 4.8: Phase velocity (Black: theoretical results; Blue: $k-\omega$ method; Red: phase spectrum method)

Figure 4.8 shows the phase velocity obtained by using $k-\omega$ method (blue line) and PS method (red circle). In the figure, PS method results show some arbitrary values when k_1b reaches 6 where is about 30 kHz in frequency domain. By checking Figure 4.5 we can find that this is the cut off frequency of the second simulation mode. Since the Fourier-transform takes contributions from all modes at a particular frequency, therefore, if these modes are mixed in time domain, they can not be separated using this method. However, when the frequency is less than 30 kHz, all the results responds to the simulation mode EM1 which is also shown in Figure 4.5.

The group velocity can be obtained by the phase velocity using Eq. (9). However, this method has a very associated large error, because the group velocity is converted from phase velocity and Eq. (9) enlarges the error of phase velocity (as demonstrated by the scatter in Fig. 4.9). Another alternative method is to pre-process the pressure signal using a band pass filter. Here, a FIR filter with a 100 Hz band width is used to process the signal shown in Figure 4.2 (b). The group velocity is obtained from the slope of the highlighted trace in processed pressure map. The result of this procedure is shown in Figure 4.9.

As shown in Figure 4.9, the group velocity obtained by converting phase velocity using Eq. (9) has a larger error than the group velocity that is obtained using when a band pass filter is used to pre-process the pressure signal, especially when k_1b is larger than 5. Hence in the experimental study reported in Section V, the PS method will be used to obtain the phase velocity only.

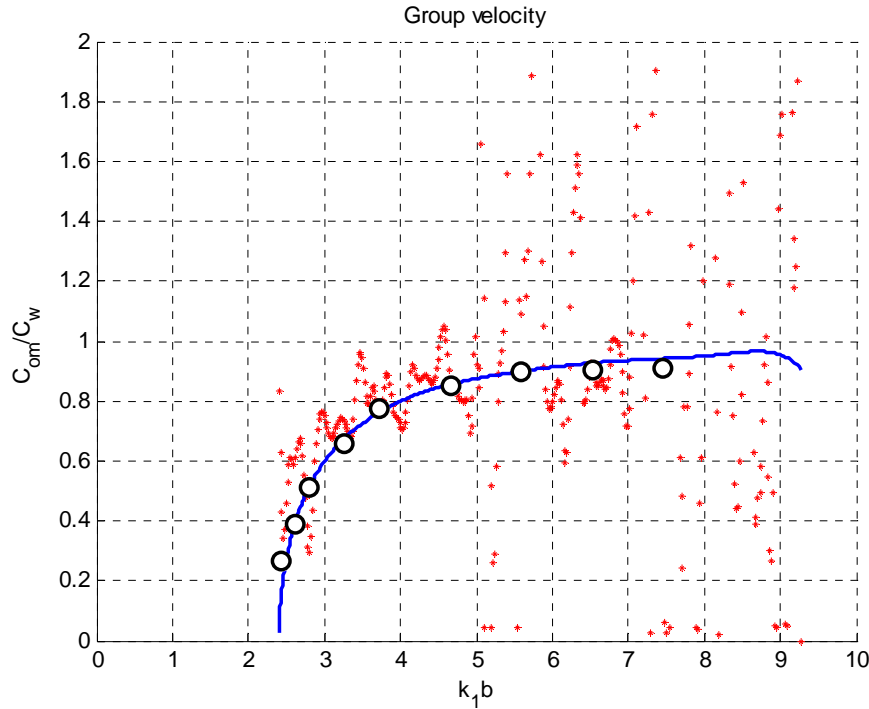


Figure 4.9: Group velocity (Blue line: k - ω method; Red star: Converted results using Eq. (9); Black circle: using band pass filter pre-process the pressure signal)

IV-4. Effect of bubbles on the propagation modes

The purpose of this part of investigation is to get an understanding of whether the presence of bubbles changes the propagation modes inside a water-filled PMMA tube.

There are two reasons motivate us to do this:

- a) The inversion method which will be used to estimate the bubble population inside a tube is influenced by the input phase velocity and attenuation. However, the phase velocity in tube relates to the mode. If the mode changes significantly when bubble presents, correction should be made to the inversion method.
- b) If the mode does change significantly with bubble's present, this characteristic may be useful to estimate the bubble population in practice.

The previous subsection showed how the mode speeds predicted by the theory of Section III agreed with those of the numerical experiment (and in Section V we shall show how these also agree with the measured data) for a bubble-free pipe. Hence, simulation is firstly conducted here to investigate the effect of the introduction of bubbles before the experimental studies which are relatively difficult.

The simulation is supposed to be conducted in bubbly-water-filled PMMA tube. However,

simulating thousands of bubble in water-filled tube is impractical here, because it introduces a computational load that is too great. To overcome this problem, a linear model, which describes how the density and speed of sound change when gas bubble presents in liquid, is used. This model is only applicable for insonification in the low frequency regime discussed in Section II, where the bubble population reduces the sound speed and this reduction depends only on the void fraction, and not the details of the bubble size distribution (see reference [28]). Based upon this model, the speed of sound in bubbly liquid, c_b , can be expressed as

$$c_b = \sqrt{\rho_g \Gamma + \rho_s (1 - \Gamma)} \times \sqrt{\frac{\Gamma}{\kappa p_0} + \frac{1 - \Gamma}{\rho_s c_s^2}} \quad (26)$$

where, ρ_g and ρ_s are the density of gas and non-gassy component respectively, Γ is void fraction, κ is the polytropic index of gas within the bubbles and p_0 is the static pressure at the position of the bubble. The density of bubbly medium can be expressed as:

$$\rho = \rho_g \Gamma + \rho_s (1 - \Gamma) \quad (27)$$

When the frequency of interest (ω) is far less than bubble's resonance frequency (ω_0), (26) can be simplified as:

$$c_b = c_s \left(1 - \frac{\Gamma c_s^2 \rho_s}{2\kappa p_0} \right) \quad (28)$$

Eq. (28) is the form presented in the reference [28]. From Eq. (26), if the characteristics of bubble medium and the surrounding medium are fixed, assuming the static pressure at bubble position is constant, the only parameter influencing the speed of sound is the void fraction. Here, Eqs. (26) and (27) are used roughly to estimate the speed of sound and density of bubbly water. These characteristics are then used to define a special medium, bubbly-water, which fills the PMMA tube. Four cases are investigated. Their parameters are shown in Table 2. It is important to emphasize that Eq. (28) and Table 2 do not give us the speed of sound of the bubbly medium in the pipe: rather they give us the speed of sound that would exist in the bubbly water if that bubbly water occupied an infinite unconfined 3D volume. We will call this value c_w

Table 2: Parameters for four simulation cases. The sound speeds shown are the low-frequency values for the speed of sound

that would exist in the bubbly water if that bubbly water occupied an infinite unconfined 3D volume (c_w).

	Void fraction	Speed of sound (m/s)	Density (kg/m ³)
a	0	1500	996
b	1e-5	1387	995.99
c	1e-4	913	995.9
d	3.3e-3	199	992.7

The largest void fraction investigated here is 3.3e-3. This is the experimental result measured when a large number of bubbles present in the tube. The $k - \omega$ (wave number to angular frequency) curves are shown in Figure 4.10.

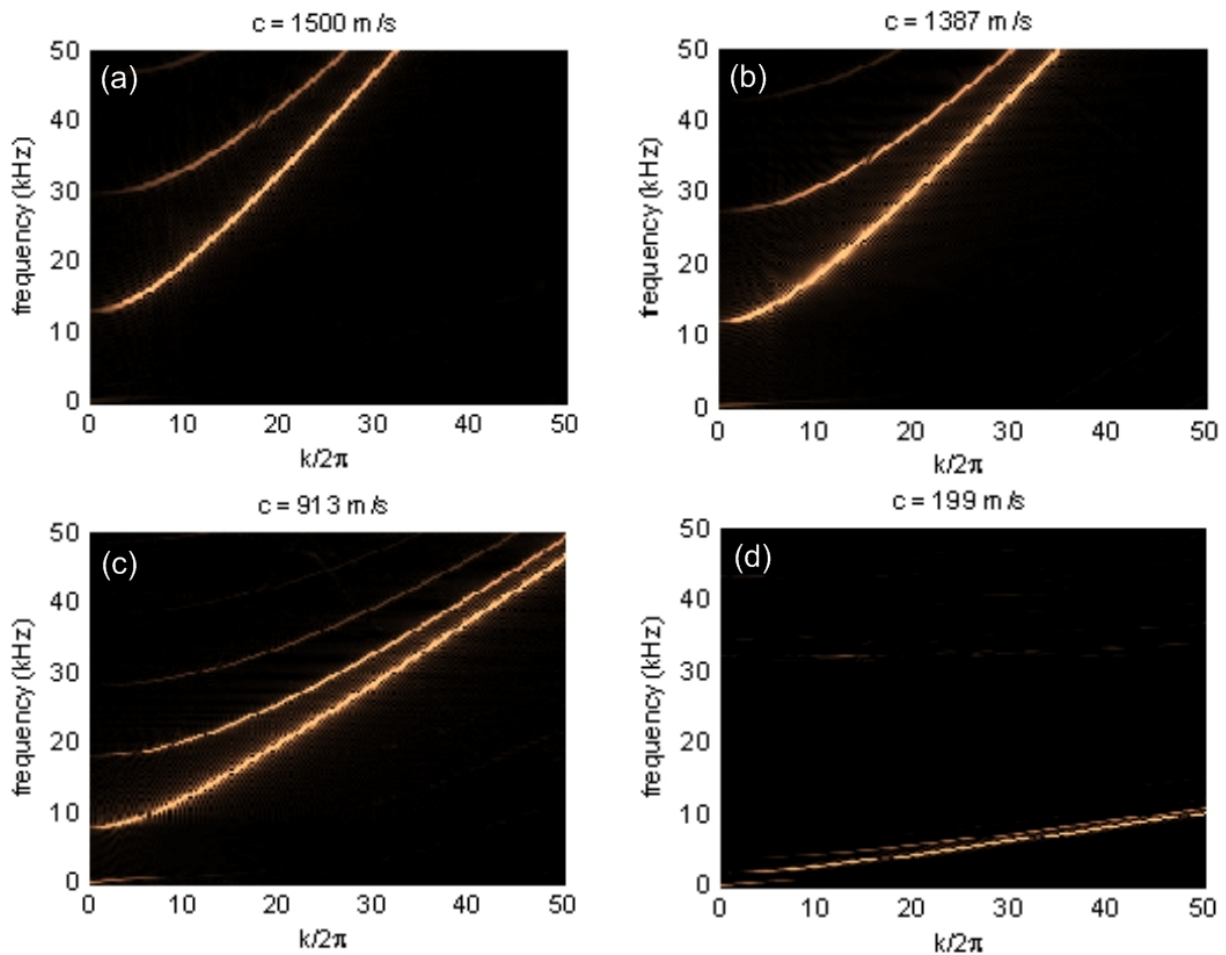


Figure 4.10: $k - \omega$ curves. The parameters for each panel are given in Table 2.

Figure 4.10 indicates clear changes to the $k - \omega$ curve between the four cases. This is because the $k - \omega$ curve is decided by the speed of sound in the medium, which changes significantly with void fraction (Table 2). The propagation modes are shown in Figure 4.11. Here the phase speed in each mode has been normalized to the speed of sound that would exist in the bubbly water if that bubbly water occupied an infinite unconfined 3D volume, which we will term c_w (i.e. the sound speed given in

Table 2). Note that the value of the normalization parameter, c_w , changes significantly between the four panels.

Using the insights gained from the simulation studies of Section IV-1, we can see that each highlighted trace consists of two parts: Using Figure 4.11(b) as an example, the ET2 mode (red) is partly shown in the first highlighted trace (when $k_1 b < 3$) and partly shown in the second high lighted trace (when $k_1 b > 7$). However, the connection between these two parts is not noticeable. Previous investigation shows that this connection part is not noticeable. Previous investigation shows that this connection part is not clear in experimental and simulation studies, but can be found in theoretical results. This characteristic may be used for bubble population estimation, but the inner connection of each mode is very difficult to excite. Hence, more investigation may be required to study how to excite these weak features, if they are expected to be used for bubble population estimation.

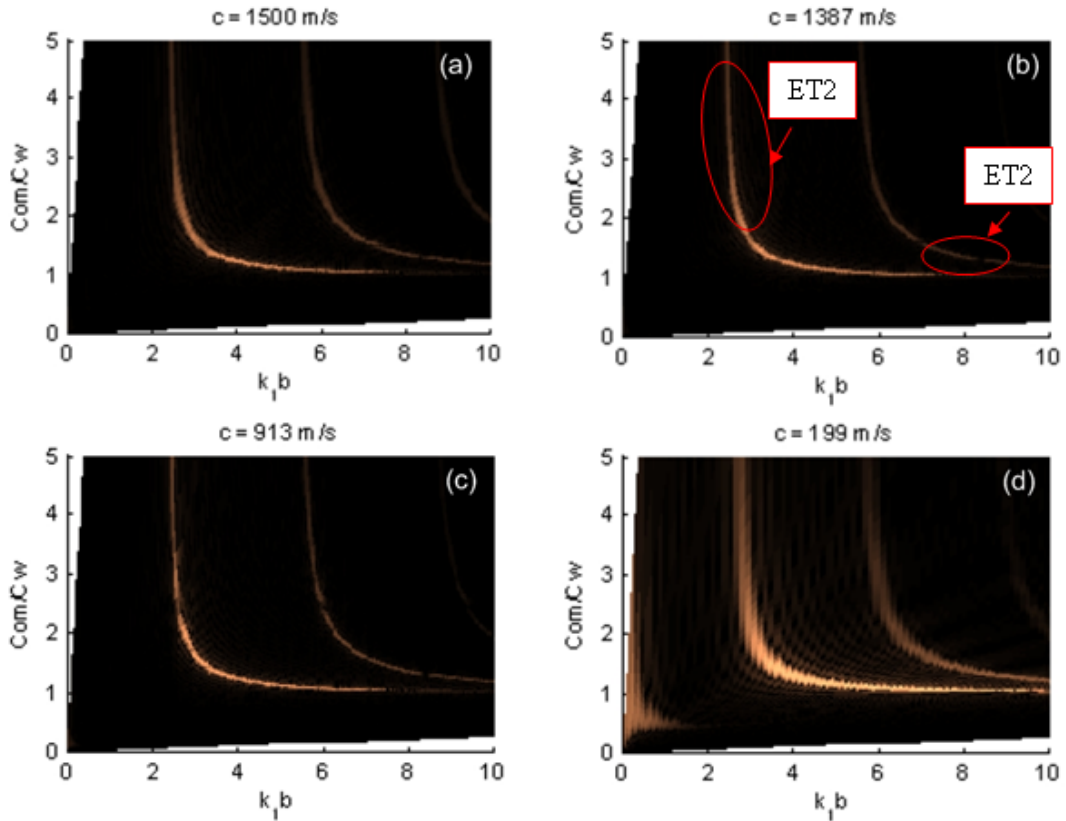


Figure 4.11: Normalized phase velocity (Highlighted traces show modes in the tube). The parameters for each panel are given in Table 2.

Despite the unclear inner connection of modes, the four figures in Figure 4.11 show similar traces. This is because the density of bubbly medium does not change much, and because the major variation (which is in the absolute values of the sound speeds) has been normalized out by referencing each panel to its particular value of c_w . When normalized by the speed of sound, which is the dominant factor influencing the sound in the liquid tube, the normalized phase speed in each mode does not change much. As a result, the intention of using the change of mode to estimated bubble population is

now seen as equivalent to estimating the speed of sound, if those unclear inner connections and break points are not considered. However, from a positive point of view, we can pay less attention to the changes of mode now, and focus on investigating how the presence of bubbles changes the speed of sound.

IV-5. Conclusions

The early simulations have been very successful in a number of ways:

- They have identified possible ambiguities in interpreting measured results, through the process of attributing observed data (albeit simulated in this case) with theoretically-predicted modes.
- They have identified ways in which use of fixed hydrophones intended for the project would tend to produce poorer data than would the moving hydrophone schematically illustrated in Figure 1.7 (the fixed hydrophone would tend to us the phase spectrum method, whilst the moving hydrophone could exploit the $k - \omega$ method). However we know that a moving hydrophone is not realistic, and therefore have used the simulations to find ways in which the data from a fixed hydrophone can be processed to improve its quality to similar levels to that which could be obtained using the moving hydrophone.

Section V will now proceed to use the findings developed so far in this report to the conduct of experimental measurements on the static test rig.

V. MEASUREMENTS AND RESULTS

This section examines to what extent we can detect the effect of bubbles on the acoustic waves propagating in the static rig, and include the development of some non-acoustic techniques to characterize the bubble population. These experiments can be seen as the preliminary stages for the next phase of work, in which a theory will be developed for mode propagation in a pipe of bubbly water. To validate this theory, its predictions will be compared to measured acoustic data when the bubble population (independently measured using non-acoustic techniques) is used as input to the theory. After such validation, the stage will be set to invert the acoustic propagation theory to determine the bubble population.

In these preliminary stages, after a discussion of the experimental techniques (Section V-1), Section V-2 discusses acoustic mode sound speed measurements in a bubble-free pipe, before Section V-3 discusses similar measurements in a pipe of bubbly water. Section V-4 discusses attenuation measurements in a pipe of bubbly water, and Section V-5 discusses the acoustic inversion based upon the measurement in Section V-4. Section V-6 discusses the non-acoustic measurements of the bubble population.

V-1. Experimental facilities

Experiments are carried out in a vertical water-filled PMMA tube of 2 m length, 3.5 inch inner diameter, and 0.5 cm wall thickness. The tube material is PMMA (also known as Perspex). The published properties of PMMA and water are shown in Table 3 [12]. These are the values that are used in the calculations reported in this paper, although it is recognized that it is possible that the properties of the real materials may depart from these published values. Because the material properties of plastics can vary even in the same material, we cannot be certain that the values listed in Table 3 are the actual values that our PMMA possesses unless we measure the elastic constants directly.

Table 3: Elastic property of PMMA and water.

Material	Density (g/cm ³)	Longitudinal velocity (km/s)	Shear Velocity (km/s)	Poisson's ratio
PMMA	1.19	2.690	1.340	0.335
Water	1.00	1.479		

Wright et al. measured the elastic constants of the glassy polymers with several samples of the Perspex and the polystyrene [29]. Their measurements showed that the density for Perspex is 1.19 g/cm³ which is identical to the value in Table 3. They also measured longitudinal and shear speeds both

in isotropic and anisotropic Perspex at 25 °C. Poisson's ratio can be calculated from the relationship between longitudinal and shear speeds. Isotropic Perspex had 2.689 km/s of longitudinal velocity and 1.326 km/s of shear velocity, which returns the corresponding Poisson's ratio as 0.339. For the isotropic Perspex, the elastic properties match the values in Table 3 up to the first or the second decimal points. In the case of the anisotropic Perspex, those values were not consistent with our values. One of their samples which gave the biggest change in the elastic constants had a range of the longitudinal speed from 2.604 km/s to 3.033 km/s and a range of the shear speed from 1.318 km/s to 1.388 km/s. Hence, the Poisson's ratio varies from 0.328 to 0.368. Because it is not known yet if our material is isotropic or anisotropic, it is predicted that the elastic constants of our Perspex should be located within this range. Figure 5.1 shows the modal dispersion curve with different choice of the elastic constants both in ET0 and ET1 modes. The black lines are calculation with our original values in Table 3. The blue curves are another calculation obtained from the lowest values of longitudinal and shear speeds of 2.604 km/s and 1.318 km/s respectively in their samples. The red curves are the other calculation obtained from the highest values of longitudinal and shear speeds of 3.033 km/s and 1.388 km/s respectively.

As shown in Figure 5.1, admitting the variance of the elastic constants, the sound speed change in each mode is negligible over most of the range. For ET1 mode, the phase velocities at the higher frequency range of $kb \geq 3$ for three cases are nearly the same. Although the differences between the calculated wave speed for the ET0 mode are increasing with increasing frequency at the high-frequency limits of Fig. 5.1, the variance in the phase velocity of ET0 mode is less than 5 percent at these frequencies. This is smaller than the $\sim 10\%$ differences that can be seen at the low frequency range of $kb \leq 3$ for ET1 mode. Therefore, it is sufficient to use the values in Table 3 in the future experiments which will be performed higher frequency range than the current experiment.

The allowed ranges for the variation of the elastic parameters of PMMA shown in Table 3 are translated in Fig. 5.1 in to variations in the predicted sound speeds for the ET0 and ET1. For the range of frequencies covered by the plot, at two modes show opposite trends in response to this variation in input parameters. The ET1 mode shows about 10% variation at the lowest frequencies, the variation reducing at the higher frequencies. The phase velocities for ET1 show very little variation in the plot at frequencies greater than those at the 'knee' for the mode which occurs for ET1 at $kb \sim 3$ (which corresponds to a drive frequency of 16 Hz). In contrast the ET0 mode shows small variation at lowest frequencies but the variation in predicted sound speed tends to increase with increasing frequency as we approach the highest frequencies shown on the plot (reaching $\sim 5\%$ at $kb \sim 18$, which corresponds to a drive frequency of 95 Hz). For the current experiments, we have not yet detected the ET0 mode, and until we do then the variation in the material properties shown in Table 3 will not significantly affect the results provided that:

- (i) The data are taken at frequencies greater than those of the 'knee' of each mode; and
- (ii) at frequencies greater than $kb \sim 18$ the mode speeds do not begin to diverge again.

Issue (i) has implications, because the introduction of bubbles into the predictive theory for bubbles is simplest in the low-frequency limit (Section IV-4), but it is here that uncertainties in material properties are greatest unless one is restricted to the ET0 mode, which has proven to be difficult to observe in practice.

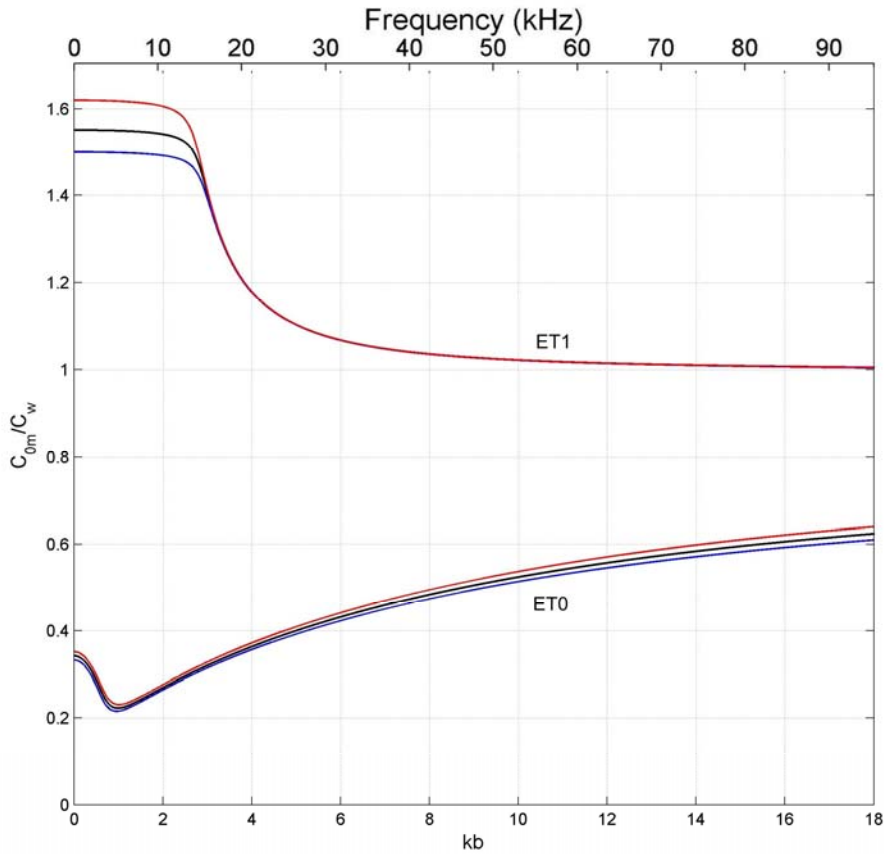


Figure 5.1: Modal dispersion curves with different choice of the elastic constants of Perspex. The black curves are a recalculation based upon the values listed in Table 3. The blue curves are calculation obtained from the values of longitudinal and shear speeds of 2.604 km/s and 1.318 km/s respectively. The red curves are calculation obtained from the values of longitudinal and shear speeds of 3.033 km/s and 1.388 km/s respectively. Changes of the longitudinal and shear speeds as input parameters in this calculation are bigger in the red curves (increase of both speeds) than in the blue curves (decrease of both speeds). However, the resulting variation of the calculated phase speeds between each modes look similar. Hence, it seems that the decrease of the longitudinal and shear speeds of the material may result in more variation of the calculation.

Figures 5.2 and 5.3 show the static test rig and block diagram of the experimental setup respectively. The middle of the three tubes is the one which is used in the current tests (the one on the right is a spare and use for duplicate testing, the one of the left has now been shipped to Precision Acoustics Ltd.-See Fig. 1.6). As shown in Fig. 5.2 and 5.3, the tube stands vertically with the help of wooden stand and clamp. An input burst signal, shown in Fig. 5.4(a), is generated by the function generator (PM 5133 produced by Philips) with a burst mode triggered by the pulse generator (PG 73N produced

by Lyons instruments). The signal is amplified by the power amplifier (Model 2100L produced by ENI , which works well at the frequency range from 10 kHz to 12 MHz) before it is transmitted to the transducer (project ref. 4008, Serial number 18852 produced by Neptune Sonar Ltd) which is fixed up at the bottom of the tube. The amplified signal is shown in Fig. 5.4(b). The transducer then sends the burst signal into the filled water via the rubber membrane which closes the lower end of the pipe. The signal transmitted by transducer is collected near the transducer and shown in Fig. 5.4(c). A hydrophone (a Brüel & Kjaer 8103, having about 1 cm diameter) is used as a receiver inside the tube. It is connected to the charge amplifier (Type 2635 produced by Brüel & Kjaer). The signal from the hydrophone is recorded by the oscilloscope which is also triggered by the pulse generator PG 73N. Signals collected by hydrophone at $z = 1$ m position in bubble-free and bubbly water are shown in Fig. 5.4(d) and 5.4(e).

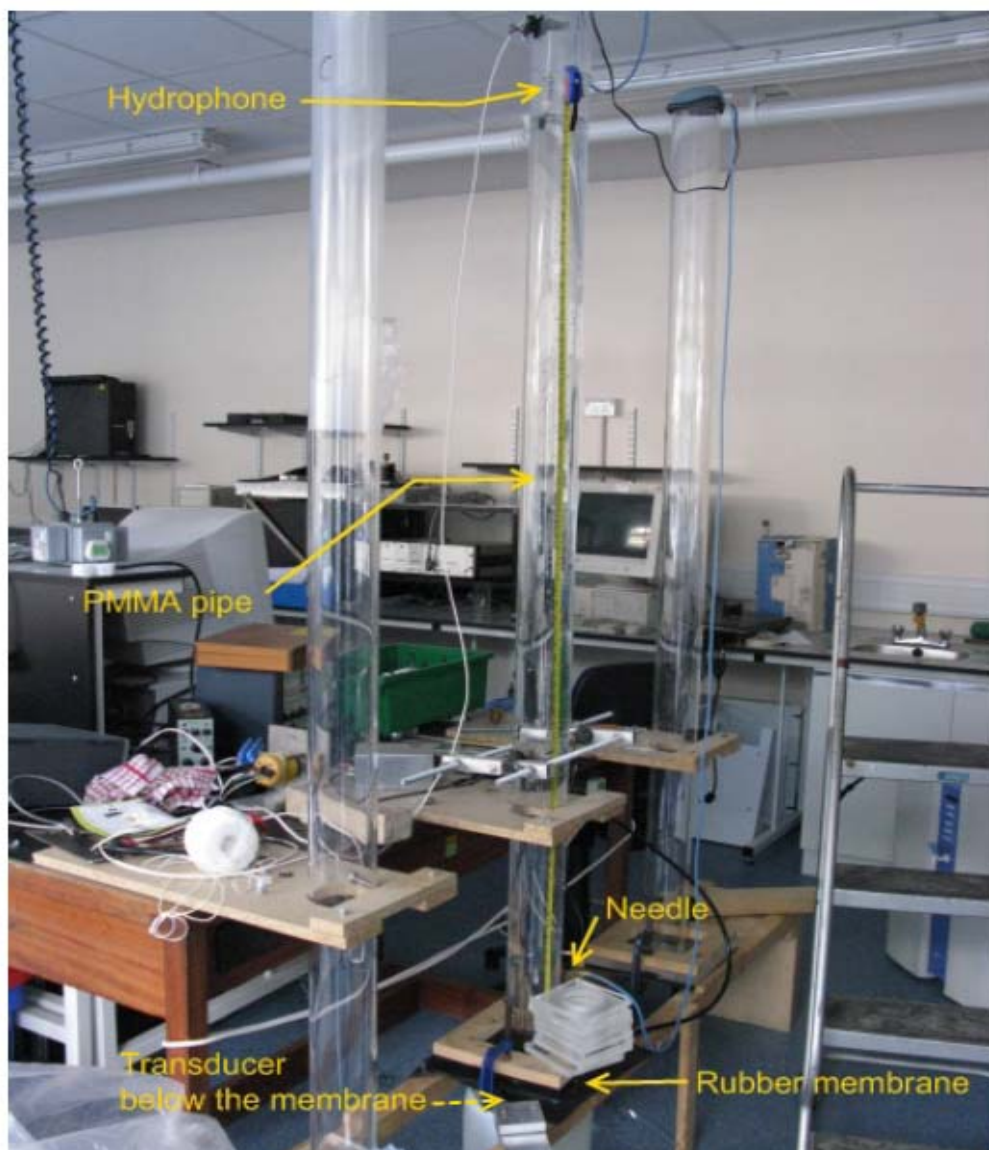


Figure 5.2: Picture of the clamped vertical pipe. It stands on the wooden stand. The transducer is positioned in the bottom of the pipe insulated by the rubber membrane.

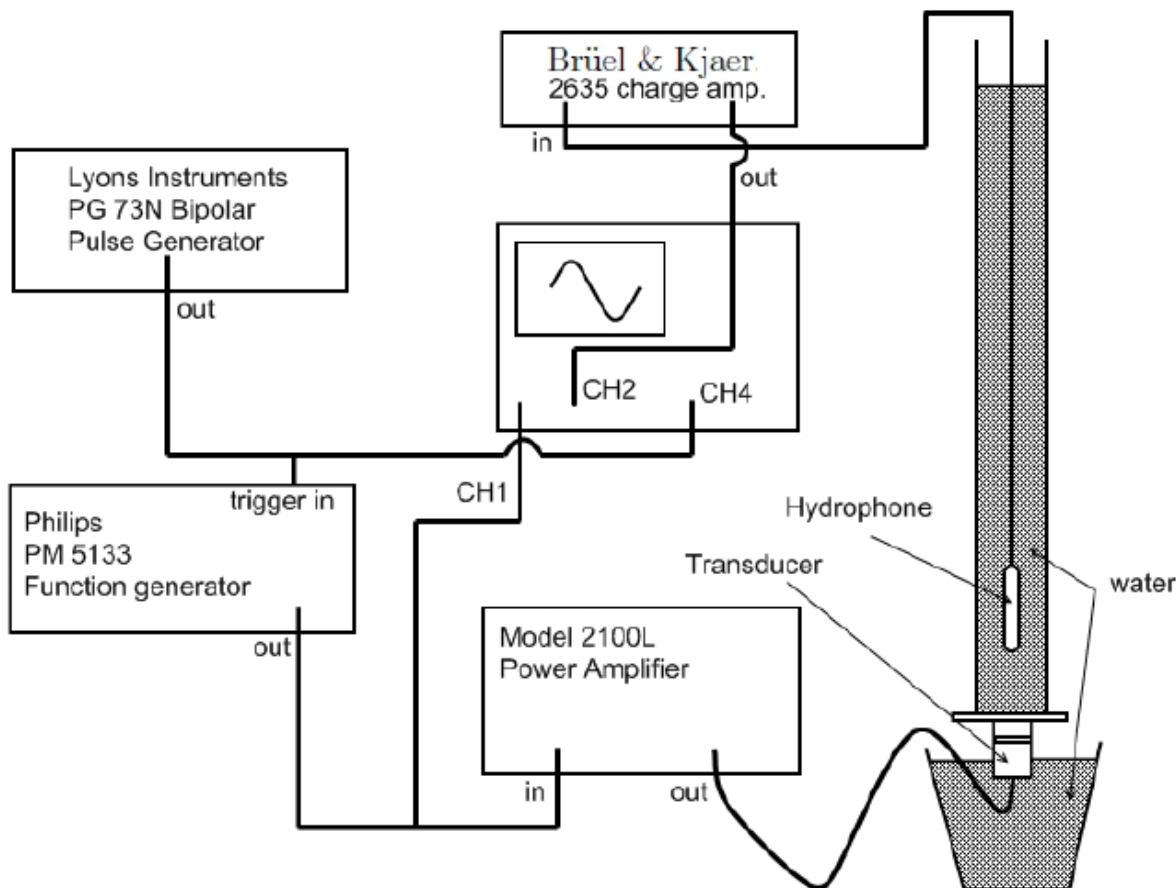


Figure 5.3. Block diagram of the experimental setup for the measurement of the water propagation in the liquid.

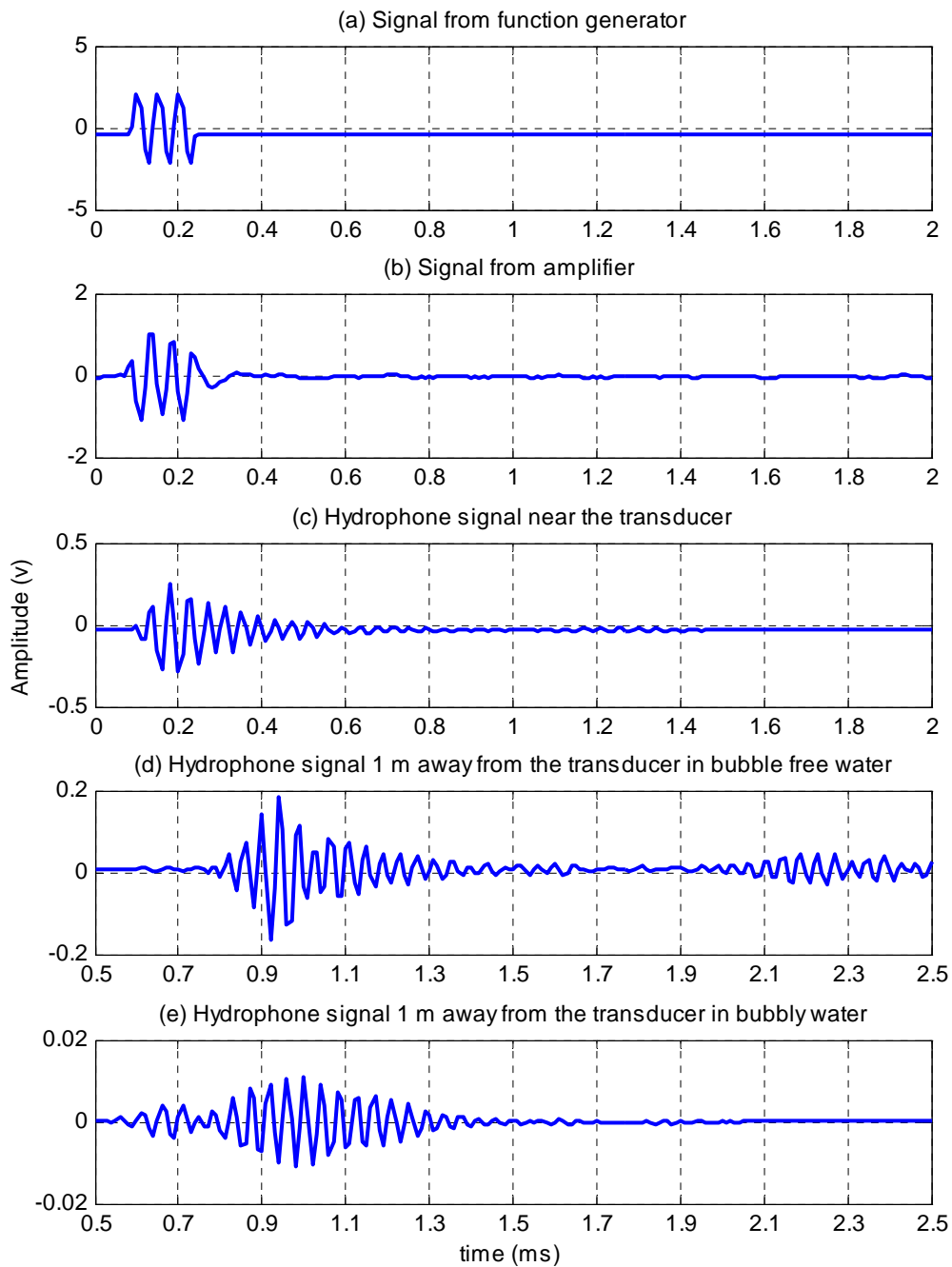


Figure 5.4. (a) Signal from function generator; (b) Signal from amplifier; (c) Hydrophone signal near the transducer; (d) Hydrophone signal 1 m away from the transducer in pure water; (e) Hydrophone signal 1 m away from the transducer in bubbly water. Second pulse shown in later time around 2.2 ms of (d) is reflected wave by the top surface of the liquid cylinder (water-air interface), which is heavily suppressed in bubbly water case as shown in (e).

The measurements are made in both bubble-free and bubbly water. Air injection was used to generate

bubbles in the water for the static rig (the flow rig will use the Venturi system discussed in Section I although injection may also be added if mm-sized bubbles are specifically required). A lumbar puncture needle, which is of 90 mm length and 0.6 mm outer diameter, is mounted at the lower part of the tube as shown in Figure 5.2. The needle connects to an air pump which injects air into the water. However, this method cannot in static water be used to generate bubbles smaller than a certain size (typically O (100 microns radius), dependent on the size of needle, injection pressure and the liquid properties; for our experimental setting, this size is about several-mm diameter). This is because, as the bore of the needle is reduced in an effort to generate smaller bubbles, those smaller bubbles rise more slowly away from the needle under buoyancy forces. As a result, a critical size is reached whereby the bubble which is newly-released from the needle does not travel sufficiently far from it by the time the success bubble grows, and the two merge (Figure 5.4). Multiple mergings can occur from a series of success bubbles, so that the eventual bubble that is released into the liquid is an amalgamation of many smaller bubbles [30].

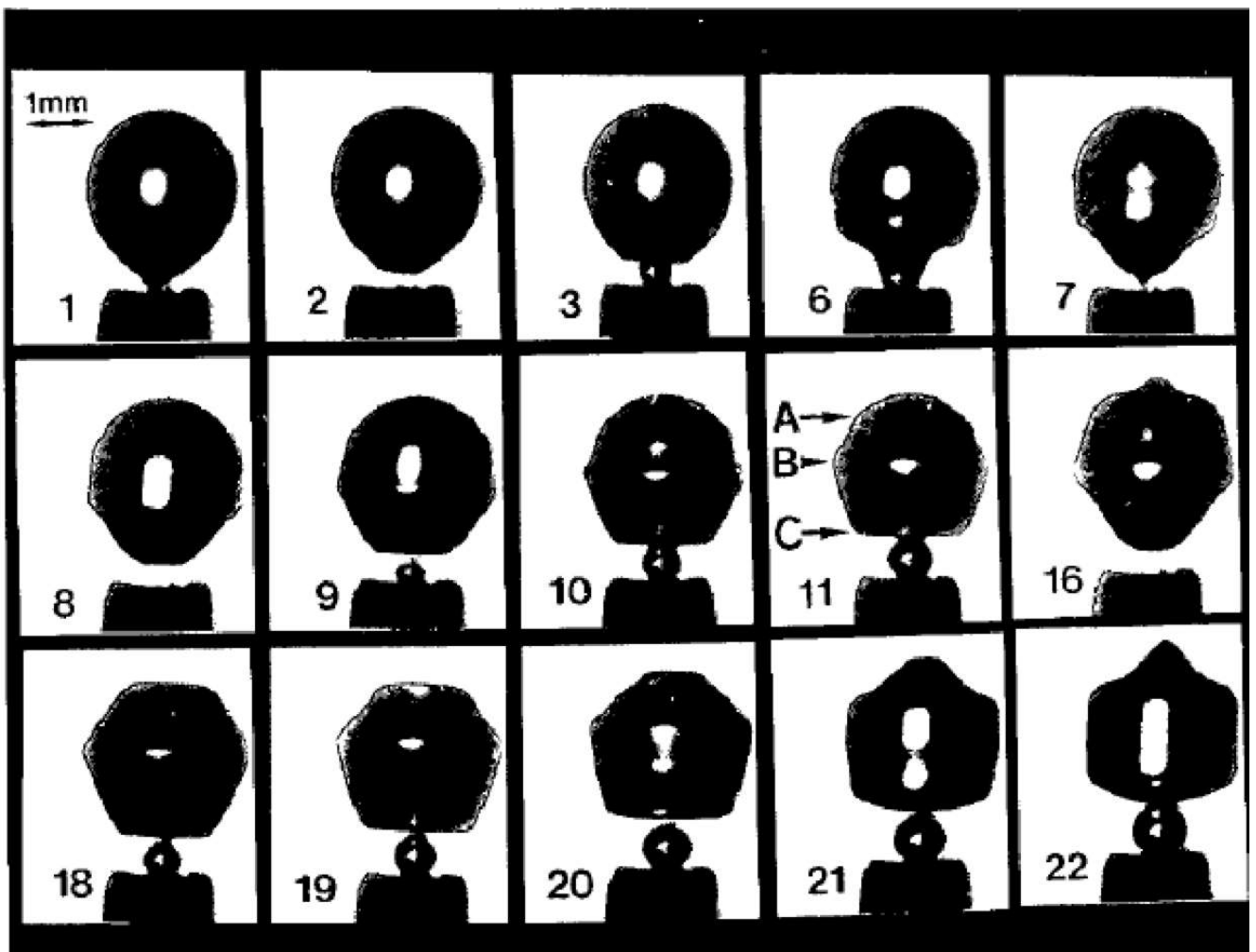


Figure 5.5. A high speed photographic sequence (interframe time = 0.24 ms, gas flow rate ~ 0.1 ml/s) of air bubbles release into water through a steel nozzle of internal diameter 0.5 mm, and external diameter 1.6 mm. This picture was taken from the reference [30].

Bubbles which are small enough to dissipate the shock waves at ORNL are key to the project under

consideration here (which is not to say that larger bubbles will not have some key role, for example in protecting the solid wall by coating it with a pressure release surface). To generate smaller bubbles using the present equipments, a vibration device is introduced to vibrate the needle. Shear forces at the needle tip mean that success bubbles are distributed further from the newly-released ones. A schematic diagram of how to generate the smaller bubble is shown in Figure 5.6.

Touching the needle with an ultrasonic horn proved to be ineffective. A commercial vibrator proved to be an effective but expensive option that was too bulky for convenient use. In the tests reported here, a vibration motor from a mobile phone is used as the vibration device, as it is compact and cost effective. Two mobile phone vibration motors are shown in Figure 5.7. They are different types, but can give the same vibration effect, which is about 10000 rpm when they are driven under 4 volts (the vibration frequency is dependent on the drive voltage). Careful tuning of the length of the needle inserted through the bug, and the position of the vibrator, allows the vibration displacement amplitude at the needle tip to be maximized.

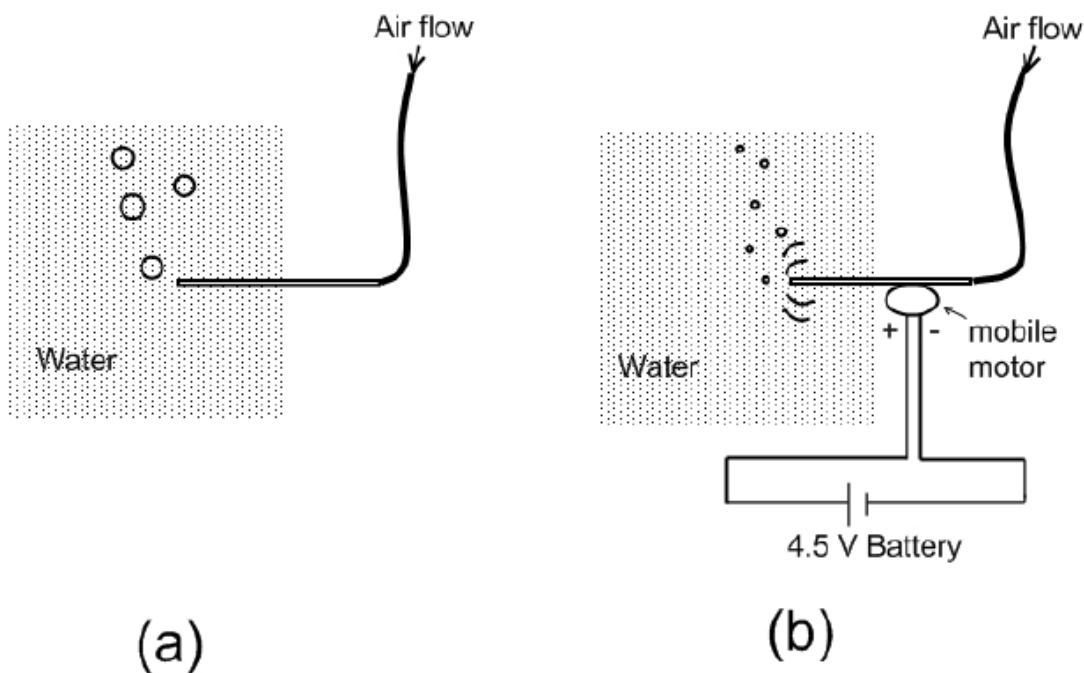
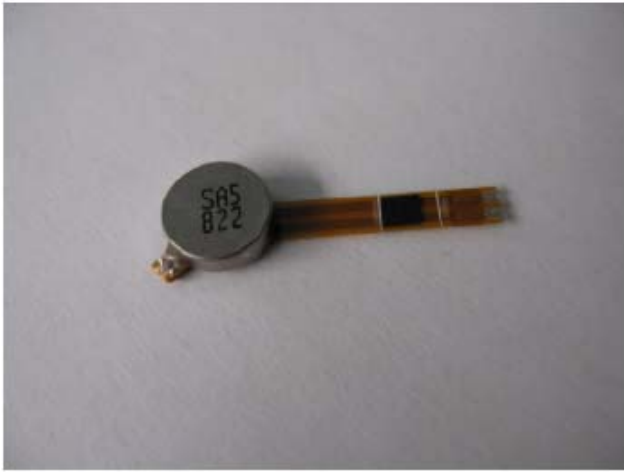


Figure 5.6. Schematic diagram of generation of small bubbles using mobile vibration motor



Disk motor

(a)



Cylindrical shape motor

(b)

Figure 5.7: Mobile phone vibration motors.



(a)



(b)

Figure 5.8: Bubbles generated (a) before and (b) after the onset of mobile vibration motor. The conditions (air flow, needle etc.) are otherwise identical in the two cases.

Figure 5.8 shows the bubbles generated inside the tube (a) without the driving of the motor and (b) with the driving of the motor. The usual size of the bubble without the motor driving is about mm order. When the vibration motor is used, the bubble size turns to be less than 0.6 mm in diameter. Hence, this is a very effective way to generate small bubbles in the water.

When bubbles are generated inside the liquid, knowing the gas volume void fraction is important because the sound speed and attenuation in the bubbly media are very sensitive to slight changes in the void fraction, as will be shown in the subsequent sections. There are several ways in the measurement of the void fraction. The easiest and the simplest method of doing this is just measuring the volume change of the bubble mixture before and the after bubble injection as illustrated in Fig. 5.9. The more bubble there are inside the static rig, the greater the change of height of the water column, Δh . Because the cross section of the water column is constant along the tube, the gas volume void fraction, Γ , is simply given by $\Gamma = \Delta h / (h + \Delta h) \approx \Delta h / h$, where $\Delta h \ll h$.

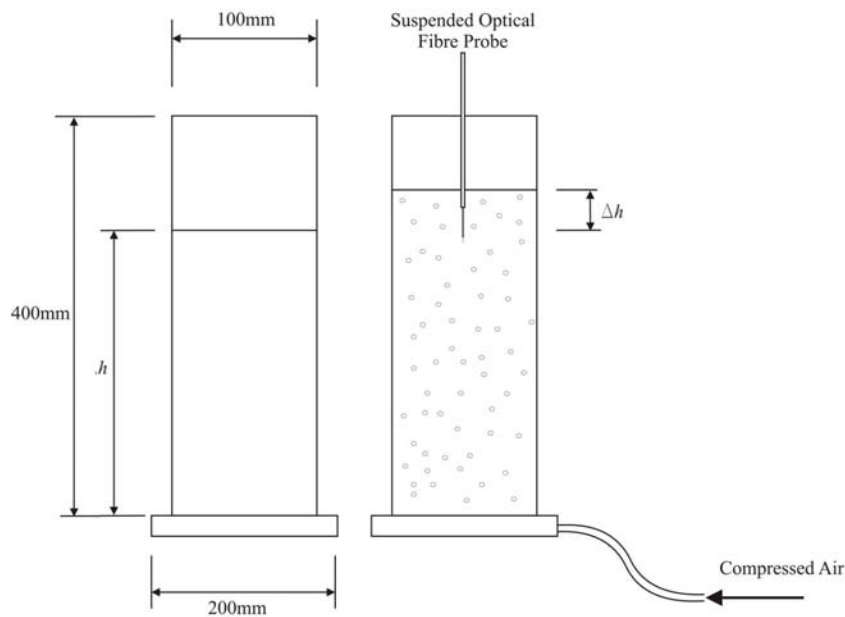


Fig. 5.9: Volume change caused by the bubble injection [31].

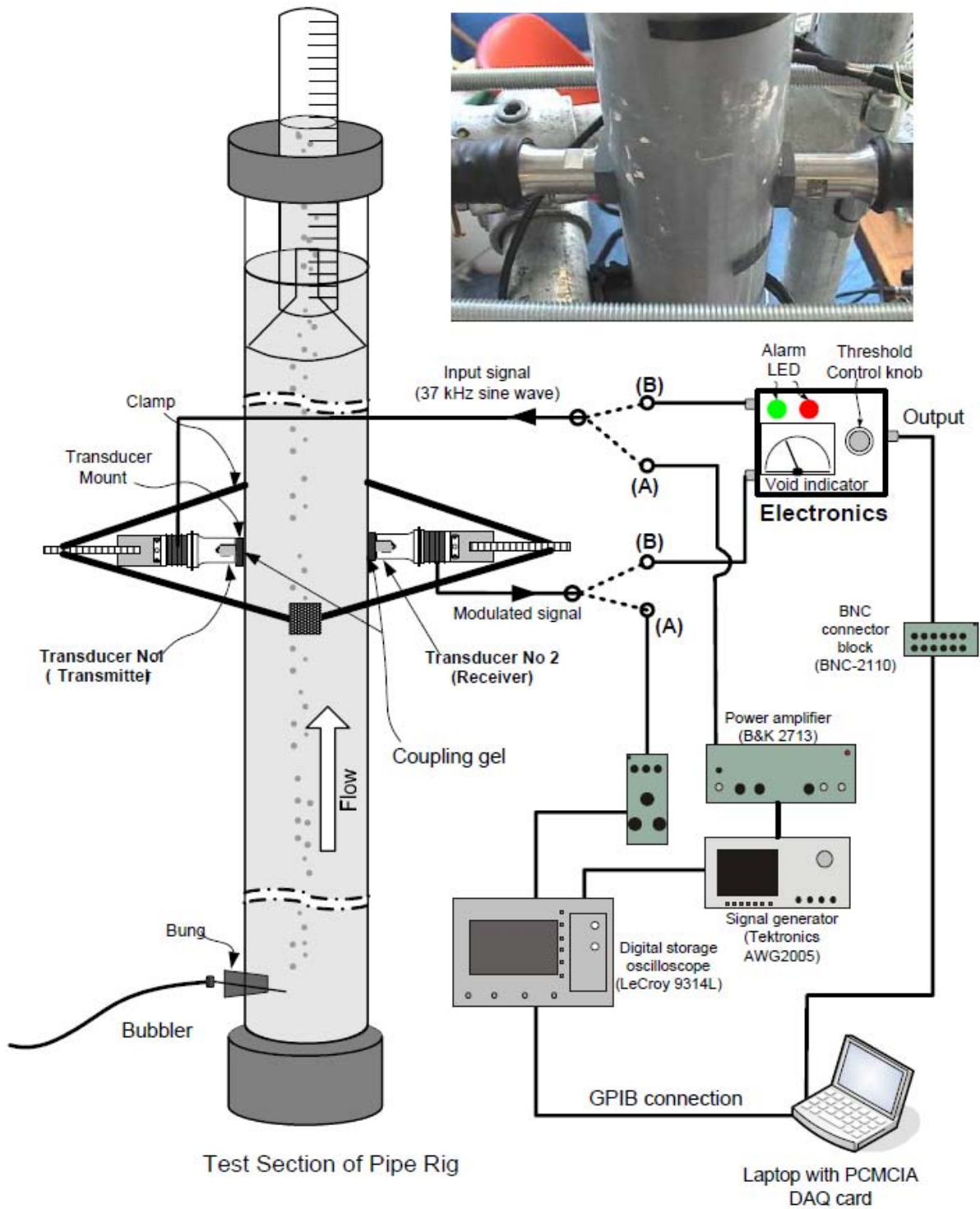


Fig. 5.10: Schematic diagram explaining the measurement technique of gas volume void fraction when the volume change of the mixture is not clearly observable. An initially liquid-filled measuring cylinder is inverted and collects the gas over a period of time. The void fraction in the water column can then be calculated [32]. The figure also shows a schematic of operation of an ultrasonic system (with associated electronics) which has been tried on the rig (where bubbles passing between an ultrasonic source and receiver disturb the beam), although details of this technique will not be reported in detail in this report.

The smaller the void fraction the less reliable this method becomes. Therefore if the void fraction becomes too small for the above method to be employed (or if the volume change is hard to be recognize because the tube bore is too wide), there is an alternative method of measuring volume change by putting a measuring cylinder (which has much smaller radius than the tube) into the water column. The initially liquid-filled measuring cylinder is inverted and collects the gas over a period of time using a funnel as shown in Fig. 5.10. Owing to the smaller diameter of the measuring cylinder, the volume change of the mixture can be easily observed by measuring the volume of gas collected over a given time (which then must be converted to give the volume present in the water column).

V-2. Sound velocity measurements in bubble-free water

The protocol for measuring the sound velocity in bubble free water is as follows. The environmental conditions are measured, including the atmospheric pressure at the time of the experiment, and the liquid and air temperatures. Surfactant was added to the water. The acoustic pressure is recorded in the time domain at the center of the tube as the hydrophone depth varied from the source transducer ($z = 0$ m) to near the air-water interface (which was located at $z = 1.8$ m). The phase velocity is then obtained by processing the pressure signals, using the k - ω method initially. After that, the alternative processing methods are used to obtain varying estimates of the sound speed: specifically, the PS method and the band pass filter method are also used to obtain the phase and group velocities. These processing methods were introduced in Section IV-3.

Figure 5.11 shows the signal measured at $z = 1.0$ m when the nominal frequency of the function generator is 20 kHz. Several large peaks are displayed as a function of the recorded time. The earliest and the largest peak is labeled the path0 reflection. The later peaks are labeled the path1, path2, path3, and path4 reflections in turn. It is obvious that there is direct signal (path0 reflection) from the source transducer to the hydrophone, and that this is followed by the reflected signals (path0, 1, 2, 3, ...). The first reflection comes from the air-water interface, and later reflections are multiples which also include reflection from the bottom membrane of the tube as the pulse 'bounces' back and forth inside the tube. According to the number of reflections from the air/water interface or the membrane, the terms path0, 1, 2, 3, ... are used. Thus, path0 reflection which is the direct signal from the transducer is shown in the earliest time. Path1 reflection is the reflected wave from the air-water interface.

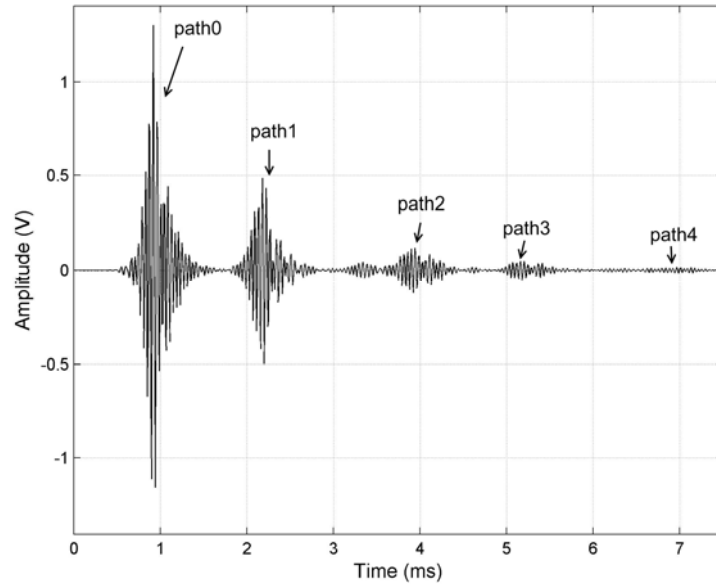


Figure 5.11: Recorded signal at $z = 1$ m of the hydrophone position in bubble-free water in the pipe. Dominant peaks display path 0, 1, 2, 3 and 4 reflections in turns.

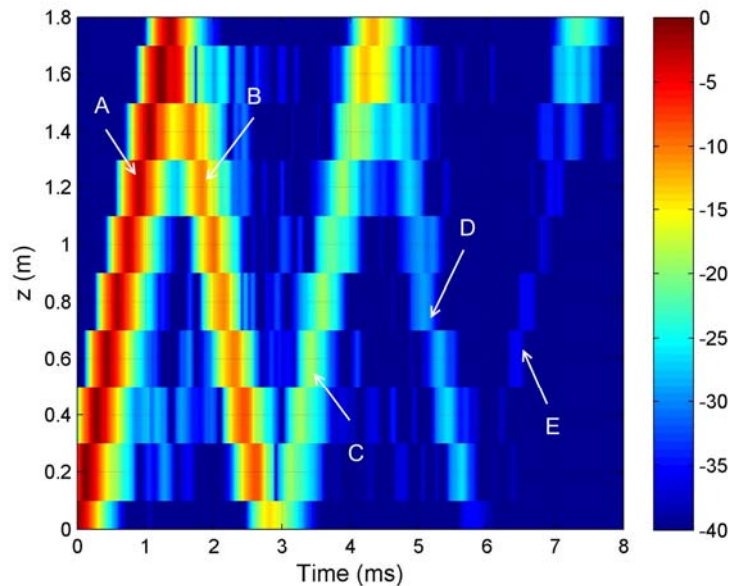


Figure 5.12: Time series of detected pressure inside the bubble-free liquid tube as a function of the hydrophone position when the driving frequency of the function generator is 20 kHz. It is simple from this picture to determine the direction in which each pulse is propagating, but this will not be so simple when there are a few discrete hydrophones fixed in place in the tube (as opposed to the moving hydrophone system shown in Fig. 1.7).

As the order of the reflection increases, the amplitudes of the peaks are decreasing because of propagation losses and because of some losses associated with reflection either by the air-water interface or by the bottom of the tube. Figure 5.12 shows the pressure profile measured by the hydrophone. It is obtained by stacking many time histories (like the one shown in Fig 5.11) for varying hydrophone positions. Thus, Fig. 5.11 corresponds to the horizontal slice of Fig. 5.12 at $z = 1.0$ m. In order to focus on the data of interest, each signal in Fig. 5.12 was correlated with the signal replica taken from the best clean and smooth path0 reflection part among the recorded signals. The central frequency of the burst signal was set to be 20 kHz (note however that this is the frequency of the electrical signal supplied to the transducer, and not necessarily the frequency of the signals in the water (see later)). The horizontal axis of the figure is time in ms and the vertical axis of the figure is distance in m between the hydrophone and the transducer. Path0 reflection is labelled as A. Path1 reflection (just behind the path0 reflection indicated as B) is the reflected wave from the air-water interface. Hence, when the position of the hydrophone is near the interface ($z = 1.8$ m), the path1 reflection and path0 reflection are merged. The wave reflected from the air-water interface (which causes signal B when it passes the hydrophone travelling downwards for the first time) is then reflected by the bottom membrane of the tube. That is the path2 reflection and is labelled as C. For the same as caused the path0 and path1 reflections to merge at the top of the tube ($z = 1.8$ m), so too do the path1 and path2 reflections are merge together at the base of the tube ($z = 0$ m). In the figure, bounces up to the path4 reflection (indicated as E) can be observed.

Although the preceding theory explained in Section III-1 suggested that at least two modes should exist inside the tube in this frequency range, only one mode is clear in the measurement. The shapes of A, B, C, D, and E are nearly symmetrical with each other and have slopes of similar magnitude, indicating that these signals all correspond to the same mode. It is believed that those are the ET1 mode. Because the ET0 mode is slower than the ET1 mode (as shown either in Fig. 3.2 or Fig. 3.3), if there exists an ET0 mode, it should bifurcate at the coordinates of (0 ms, 0 m) and be recorded in the time series as a slower feature in Fig. 5.12. However no such feature is clearly visible. Hence, only ET1 mode was treated in the report.

Although the transducer is driven at 20 kHz, the peak frequency of the signals in Fig. 5.12 is not the same as this frequency. This fact is clearly shown in Fig. 5.13. The figure shows the spectra of the output signal from the function generator, the amplified signal by the power amplifier which drives the transducer, and the directly measured signal by the hydrophone at the nearly contacting point of the hydrophone with the bottom membrane. All the pictures in the left and right columns are the spectra at 10 kHz and 20 kHz of the frequency of the function generator respectively. The spectra of the output of the generator and the amplified signals by the power amplifier have spectral peaks nearly at the driving frequencies of the function generator as shown in Figs. 5.13(a) – (d). But, the spectra of the directly measured signal by the hydrophone do not have their spectral peaks be located at the driving frequencies as shown in Figs. 5.13(e)-(f). In Fig. 5.13(e), the spectral peak is located around 11.5 kHz and slightly shifted from 10 kHz of the driving frequency. Another anomaly in Fig. 5.13(e) is that two

big peaks more than 50% of the biggest peak are observed around 20 – 30 kHz where the spectra shown in Figs. 5.13(a) and (c) have small peaks (less than 10% of their largest peaks in that frequency range). This is caused by the localized frequency response of the transducer. According to the specification of the transducer, its resonant frequency is 24.5 kHz and it has a good frequency response from 20 to 30 kHz. Outside of this region, the response decreases abruptly. Hence, although the driving frequency is 10 kHz in Fig. 5.13(e), the frequency components below 20 kHz were suppressed and the frequency components between 20 kHz and 30 kHz were magnified. This tendency is clearer in the right column of the picture. In Fig. 5.13(f), the spectral peak is located around 24.5 kHz although the driving frequency is 20 kHz. The spectral peaks in Fig. 5.13(b) and (d) are close to 20 kHz and several peaks are around 30% of their biggest peaks are shown in the low frequency range of 10 kHz. But, in the spectrum in Fig. 5.13(f), all the frequency components around 10 kHz is sufficiently suppressed and less than 5% of the spectral peak around 24.5 kHz. Therefore, the trace shown in Figure 5.12 has spectral peak around 24.5 kHz although the driving frequency of the function generator is 20 kHz.

A $k - \omega$ method is first adopted to obtain the velocities. The 2-dimensional pressure spectrum is shown in Figure 5.14(a), where several dominant modes are highlighted. They are isolated and shown in Figure 5.14(b).

The phase velocities obtained from the extraction shown in Fig. 5.14(b) are displayed in Fig. 5.15. $k - \omega$ method was used in the measurement of the phase velocity. Solid curves are theoretical calculations and the blank circles are the measurements. Our measurements are quite close to the theory but slightly less, which could be accounted for by the adjusting material properties of PMMA. Measurement of the ET2 mode in the high frequency range has more errors than in low frequency range of the same mode. The same trend is seen in the ET3 mode. The ET0, ET4, and higher modes are not investigated. Nevertheless the experiment shows the modal dispersion relation of the modes inside the liquid cylinder.

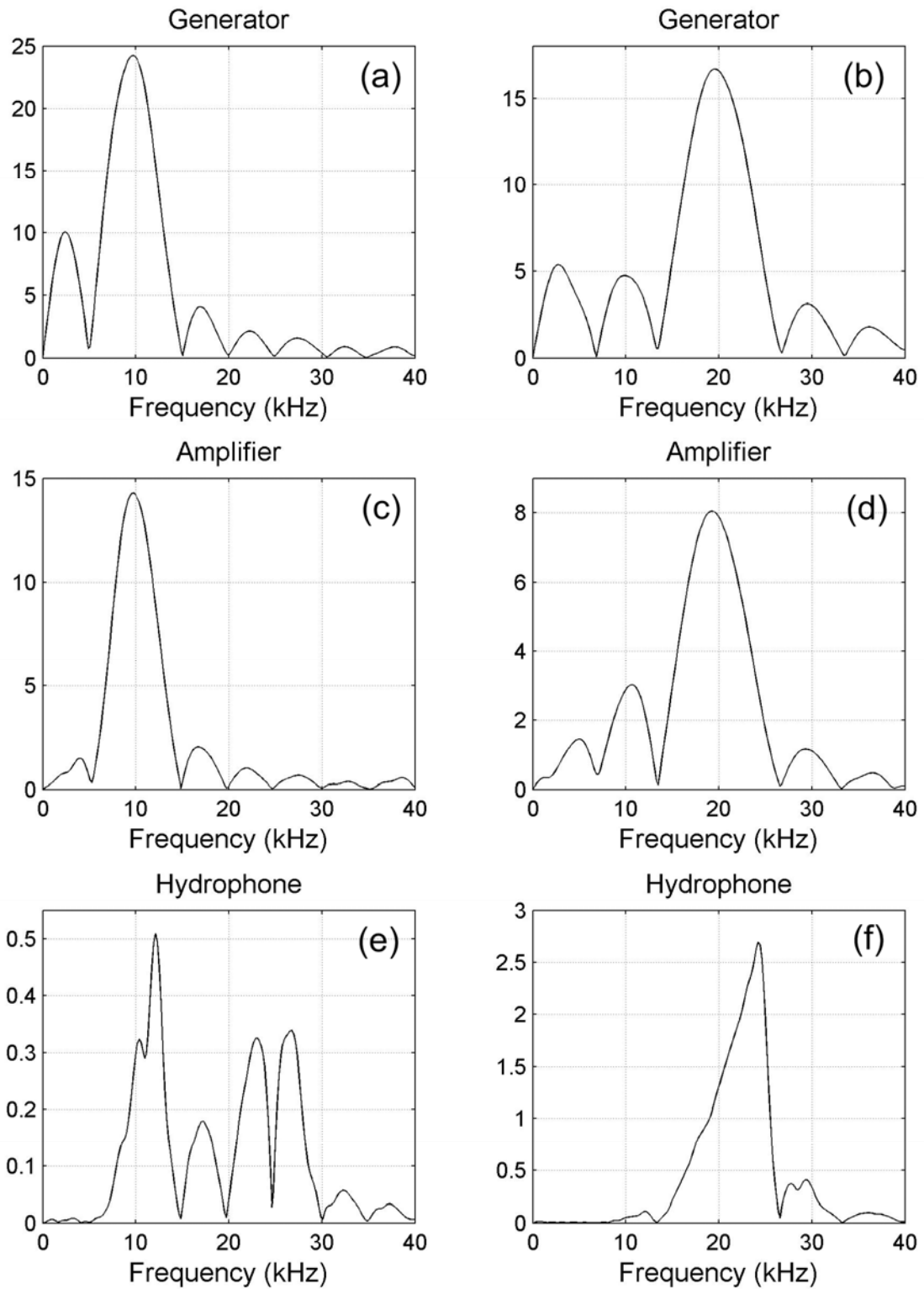


Figure 5.13: Spectra of the output signal in bubble-free liquid cylinder from (a) and (b) the function generator, (c) and (d) the amplified signal by the power amplifier which drives the transducer, and (e) and (f) the directly measured signal by the hydrophone at 10 kHz (left column) and 20 kHz (right column) of the driving frequency of the function generator.

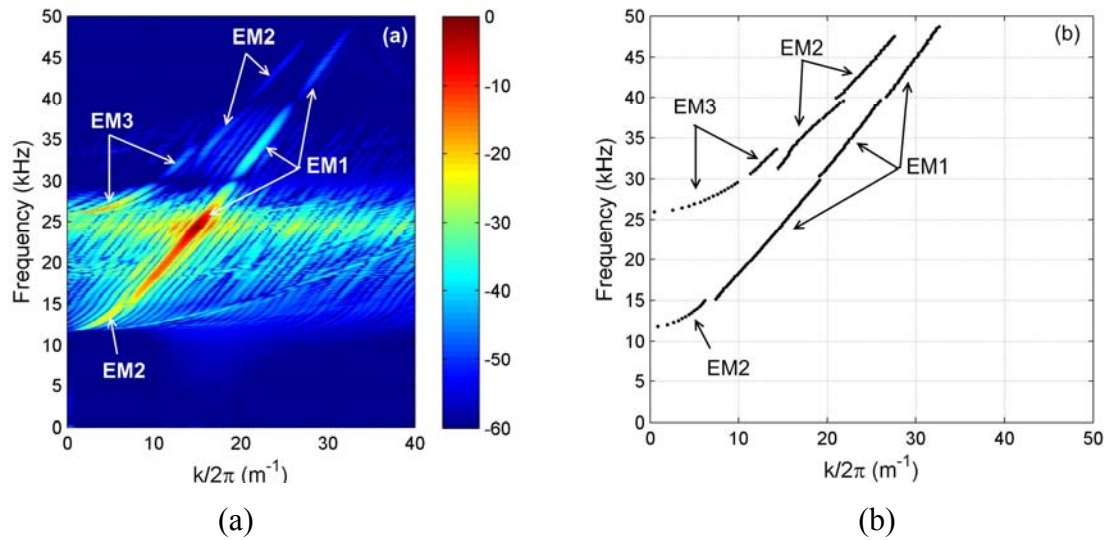


Figure 5.14: (a) 2D pressure spectrum. (b) Dominant mode determined from the data of Fig. 3.2 for measurements in bubble-free water in the pipe.

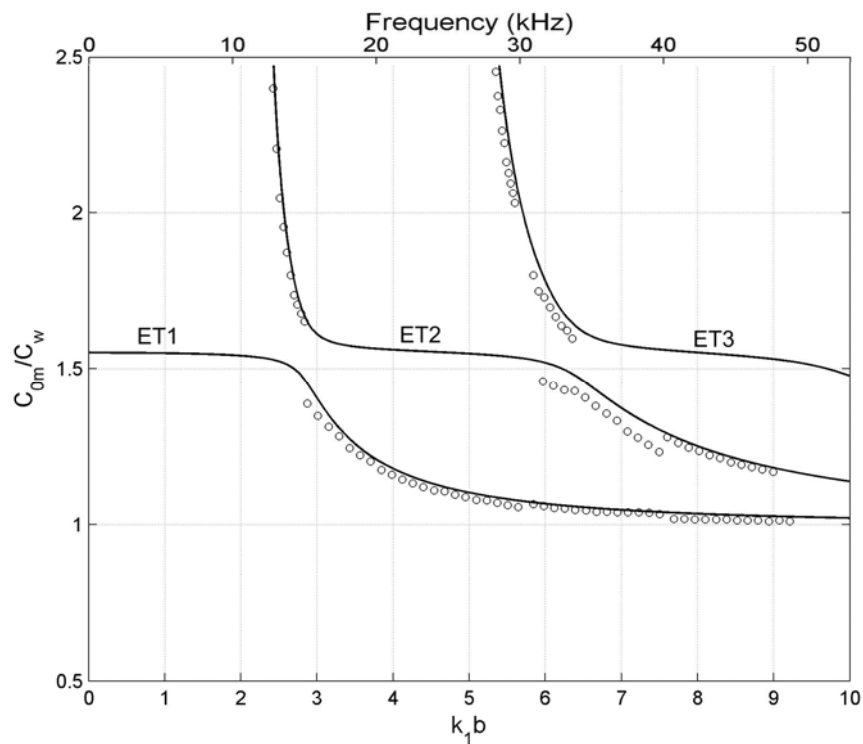


Figure 5.15 Theoretical calculations (solid curve) and the measurements (blank circle) calculated from Fig. 5.14 for the mode phase velocities in bubble-free water in the pipe. k - ω method was used in the measurement of the phase speed.

V-3. Sound velocity measurements in bubbly water

The same experiment as described in Section V-2, was carried out in bubbly water by injecting air into the tube through the vibrating needle system described earlier. The void fraction simply measured by the volume change in the water column before and after the bubble injection is 0.33 % as shown in Figs. 5.9 and 5.10. Although this method was the one used to determine void fraction at the time the acoustic data of this subsection were taken, since then superior methods (e.g. μ CORT, Section V-6) have been under development which will give the bubble size distribution. In order to compare the effects by big bubbles and small bubbles, two different sizes of bubbles were tested. At first big bubbles were injected. Figure 5.16(a) shows the pressure profile at 20 kHz of excitation. Comparing this figure with Fig. 5.12, the bubble-free case, it is obvious that the presence of bubbles suppresses the reflection by the interface. The higher orders of reflection are not seen because the presence of the bubbles attenuates the reverberations inside the tube. Thus the path1 and or path2 reflections are suppressed and only path0 reflection is dominant. The slope of path0 reflection which tells the group velocity at the peak frequency around 24.5 kHz is similar as that of Fig. 5.12, but it is less than that by approximately by 8 %. Figure 5.16(b) shows the spectrum of the time series of Fig. 5.16(a) in $k - \omega$ space. Comparing this with the non-bubbly spectrum shown in Fig. 5.14(a), many similar features are observed. However, they are not identical. The presence of the bubbles distorts the features in the low wavenumber (long wave length) region.

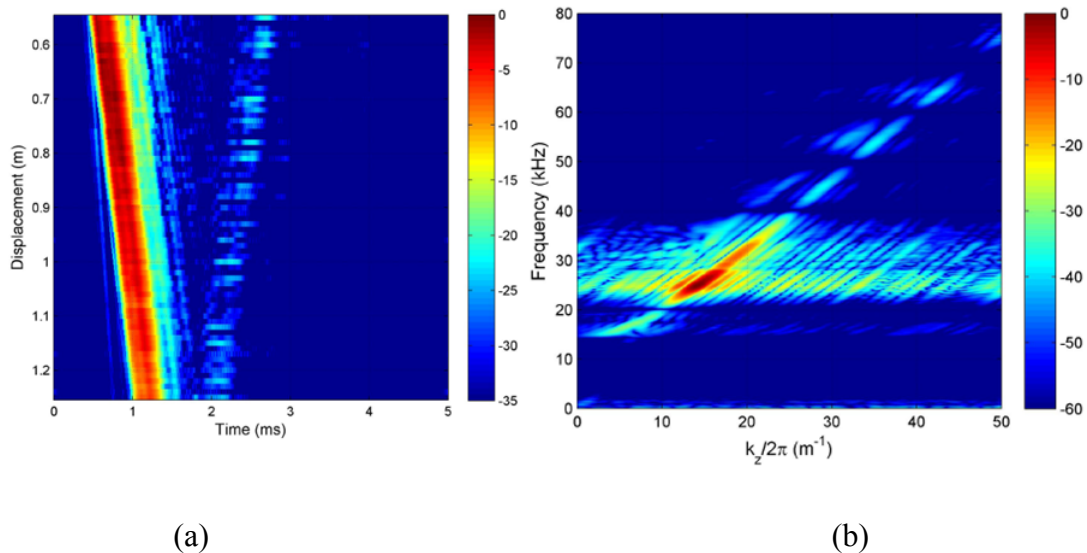


Figure 5.16: (a) Pressure profile in the bubbly water inside the tube as a function of the hydrophone position when the acoustic excitation is 20 kHz and (b) 2D spectrum of (a). The order of magnitude of the bubble radius is a mm.

Extracted modes from Fig. 5.16(b) are converted into phase velocities to compare the change of the dispersion between bubbly and non-bubbly cases as shown in Fig. 5.17. The solid lines show the calculated modes speeds for dispersion in the bubble-free case and the blank circles show the extracted mode data from Fig. 5.16(b). Compare this figure with Fig. 5.15. It is clear that the presence of bubbles changes the phase speed of each mode. Comparing Fig. 5.17 with Fig. 5.15, high frequency behavior of ET1 mode at $kb > 7.5$ (about 40 kHz) is nearly the same as the measurement of the non-bubbly case. This means that the introduction of this size of bubble distribution does not affect the phase speed of this mode at this frequency range. This is not unexpected from the discussion in Section III-2, where it was explained that for bubbles in an infinite 3D body of liquid, at frequencies much greater than resonance the bubbles tend not to affect the sound speed because they do not pulsate significantly. However, as expected, a change of phase speed is clearly seen in the range less than that frequency. Measurement of the ET1 mode shows an increased phase speed compared to the bubble-free case. But for the ET2 mode, the phase speed becomes bigger at $kb < 3.4$ (about 18 kHz) and $kb > 6.6$ (about 35 kHz). Although, measurements of the ET2 mode are not seen between the range $3.4 < kb < 6.6$, it is clear that the phase speed becomes smaller at this range. Hence, this size of bubble population distorts the phase speed of modes.

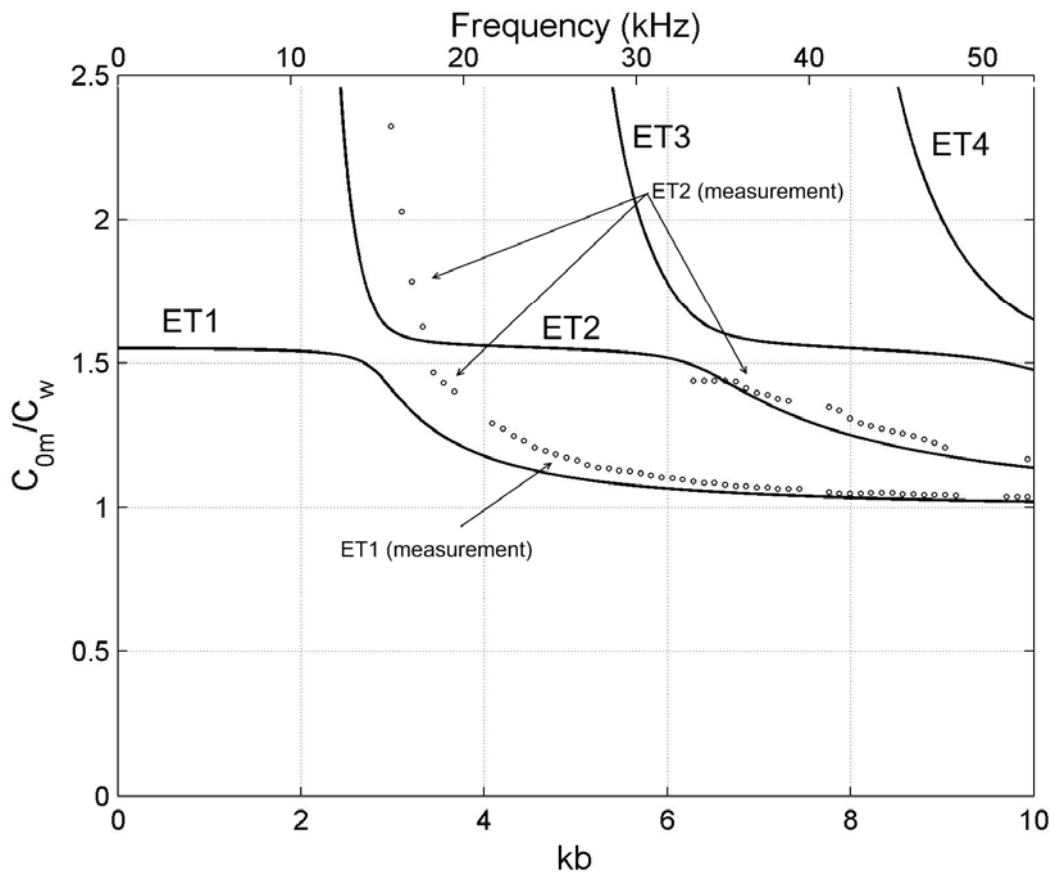


Figure 5.17: Theoretical calculations (solid curve) and the measurements (blank circle) calculated from Fig. 5.16. Compare this with Fig. 5.15. The order of magnitude of the bubble radius is a mm.

The ET3 mode and the higher modes are not observed in the measurements, which may be due to the high attenuation. Although it is not certain if that is really due to the attenuation of mode, attenuation coefficients of each mode for the bubbly case inside the liquid tube will be calculated in the future. To provide a comparison of the bubble size effect on the change of the sound speed, small bubbles were introduced at this time. The typical order of magnitude of the bubble radius is 0.1 mm which is 10 times smaller than the previous case shown in Figs. 5.16 and 5.17. The measured pressure profile and its spectrum are shown in Fig. 5.18. Compare this with Fig. 5.16. In the pressure profile shown in (a), it is obvious that the reverberation from the top interface is sufficiently suppressed, which means heavy attenuation. Because the bubble size is smaller than in the big bubble case, the number of bubbles inside the tube increased under the constant air-flow injection into the pipe. Furthermore, the smaller size of bubbles makes them closer to resonance with the sound field. The greater number of near-resonant bubbles causes increased attenuation which will be clearly shown in the next section. Comparing the spectrum shown in (b) with the spectrum of non-bubbly case in Fig. 5.14(a), it is more distorted than the big bubble case. Thus, the change of phase speed is predicted to be more severe than the big bubble case.

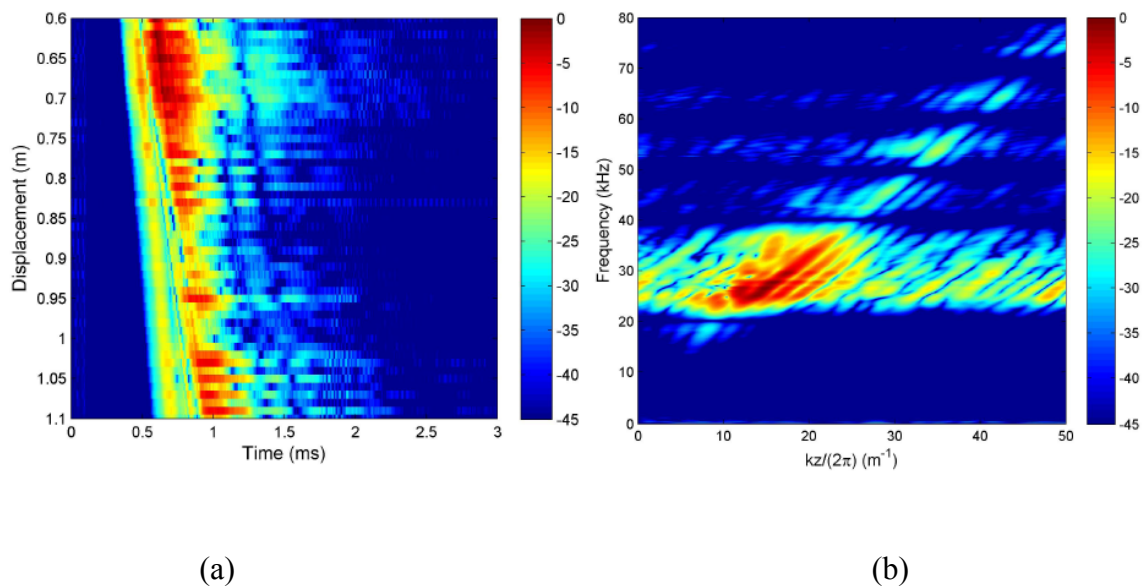


Figure 5.18: (a) Pressure profile in the bubbly water inside the tube as a function of the hydrophone position when the acoustic excitation is 20 kHz and (b) 2D spectrum of (a). The order of magnitude of the bubble radius is 0.1 mm. The condition to generate this size of bubbles (air flow, needle, etc.) is identical to the condition used in Fig. 5.16 except the onset of the mobile phone motor.

Figure 5.19 shows the phase speed of each mode calculated from the spectrum in Fig. 5.18(b). Compare this figure with the results of big bubble case (Fig. 5.17). In the small bubble case, it is clear

that the presence of bubble changes the phase speed of each mode. Comparing this with Fig. 5.15, the high frequency behavior of the ET1 mode at $kb > 9.5$ (about 50 kHz) in this bubbly case (Fig. 5.19) is nearly the same as the measurement of the non-bubbly case (Fig. 5.15). This frequency is higher than that of big bubble case because resonance frequency for small bubbles is higher than big bubbles. Measurement of the ET1 mode gives increased phase speed. Comparing the predicted (and hence currently bubble-free) phase speed of the ET1 mode with the measured data of for bubbly water in Fig. 5.17, the measured phase speeds for the ET1 mode for small bubble case are slightly larger than the measured ET1 mode for big bubble case. But for ET2 mode, only the branch which has lower phase speed than non-bubbly case was detected in the range of $7.9 < kb < 9.2$ (about from 42 kHz to 49 kHz). In the frequency range less than $kb < 7.9$ (about 42 kHz), the locus of the ET2 mode is difficult to detect because it was not seen or buried under aliased signals or noise. Instead, the ET3 mode (which was not clearly seen in the big bubble case of Fig. 5.17) can now be seen in the small-bubble case of Fig. 5.19. At the moment, the ET3 mode seems to have bigger phase speeds than the non-bubbly case all through the frequency range. More investigations for higher modes including ET3 mode are necessary in the future works.

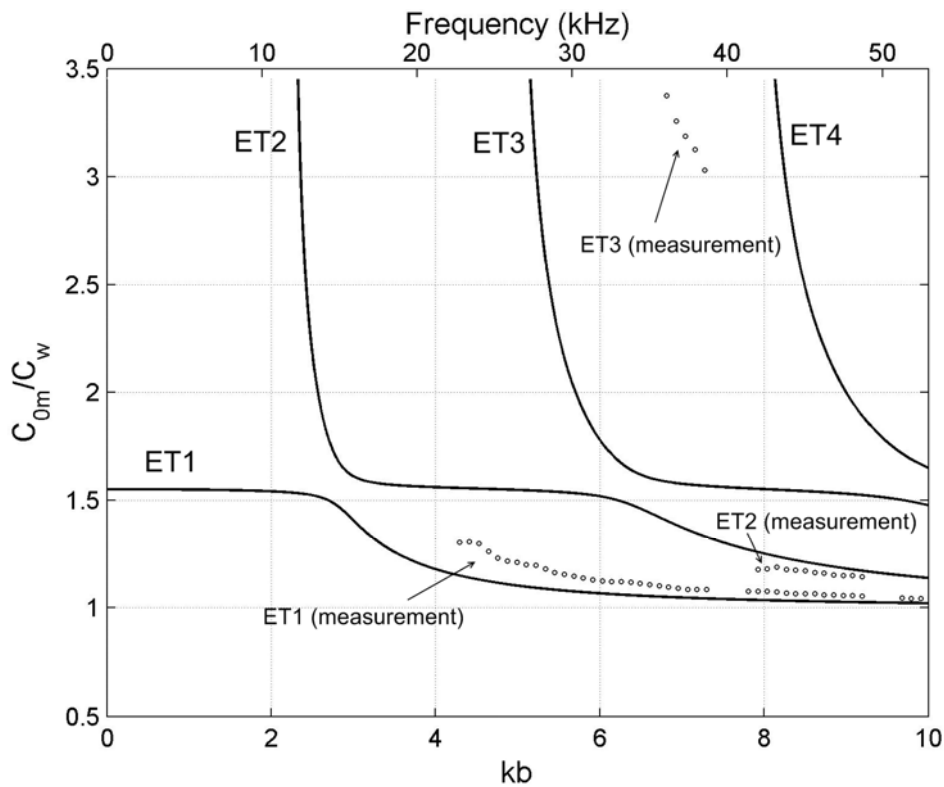


Figure 5.19: Theoretical calculations (solid curve) and the measurements (blank circle) calculated from Fig. 5.18. Compare this with Figs. 5.15 and 5.17. The order of magnitude of the bubble radius is 0.1 mm.

V-4. Attenuation coefficients measurements in bubbly water

As referred from Section III-4, the presence of bubbles causes the attenuation of wave propagation in the media. It depends on the size and the number of bubbles contained in the media. Hence, knowing bubble spectrum is an important factor to determine the attenuation. The size of bubbles is related to the frequency band where the attenuation occurs the most. For a given size profile in a population, an increase in the number of bubbles suppress the amplitude of the propagating waves more, which is clear in Fig. 5.20. This figure is the series of the photos of generated bubbles and the corresponding measured amplitude by hydrophone in water inside the PMMA tube. The source transducer is mounted at the bottom of the tube. Bubbles are injected through the needle located about 18 cm above the bottom. The injected bubbles rise due to the buoyancy and continuous injection fills the region between needle and the top surface with air bubbles. Small bubbles are generated by shaking the mobile motor attached on the needle as shown in Fig. 5.6. The hydrophone is located about 26 cm above the needle. Thus, the distance between acoustic source and the receiver is about 44 cm. When the motor does not shake, big bubbles that are usually mm order come out from the needle as shown in Fig. 5.20(a). The corresponding measured pressure by the hydrophone shown on the screen of the oscilloscope is Fig. 5.20(b). When a switch was on to activate the motor, smaller bubbles are generated as shown in Fig. 5.20(c). Since, the air flow through the needle is constant, the gas volume void fraction is not changing. Instead, the number of bubbles increases because the size of the bubbles decreased. Looking at the corresponding measured pressure on the scope is shown in Fig. 5.20(d) and it is clear that the amplitude decreased by nearly 50 %. When the voltage to the motor was further increased, much smaller sizes of bubbles are generated and the number of bubbles increases as shown in Fig. 5.20(e). The recorded wave pressure on the scope is indistinguishable from the white noise. This demonstrates how changing the size and number of bubbles can affect the attenuation: as we proceed from (a) to (e), not only does the number of bubbles increase, but their size decreases and tends to be closer to that which is resonant with the projected wave.

Attenuation coefficients were measured for the data set already shown in the measurement of the phase speed, Figs. 5.17 and 5.19. During the measurement, the air flow through the needle was not changed. Hence, the number of bubbles in the small bubble case is much higher than that in the big bubble case. Relating gas volume void fraction Γ with the equilibrium bubble radius R_0 and the number of bubbles per volume n_b , $\Gamma = \frac{4\pi}{3}n_b R_0^3$ is satisfied under the assumption of the spherical shape of bubbles. So, for a fixed gas volume void fraction, the number of bubbles per unit volume is proportional to the cube of the equilibrium bubble radius. The usual bubble size of big bubble case is a mm and it is 10 times bigger than the usual bubble size of small bubble case, which is 0.1 mm order. Therefore, the number of bubbles in the small bubble case is estimated as 1000 times higher than the number of bubbles in big bubble case. As shown in Fig. 5.20, the increased number of small bubbles cause the heavier attenuation. The measured attenuation coefficient is shown in Fig. 5.21 in dB per unit length as a function of frequency. As expected, the attenuation coefficient in the small bubble case is

measured to be bigger than that in the big bubble case across most of the frequency range. Above around 17 kHz, the attenuation coefficient for small bubble case is 3-5 times larger than that for big bubble case.

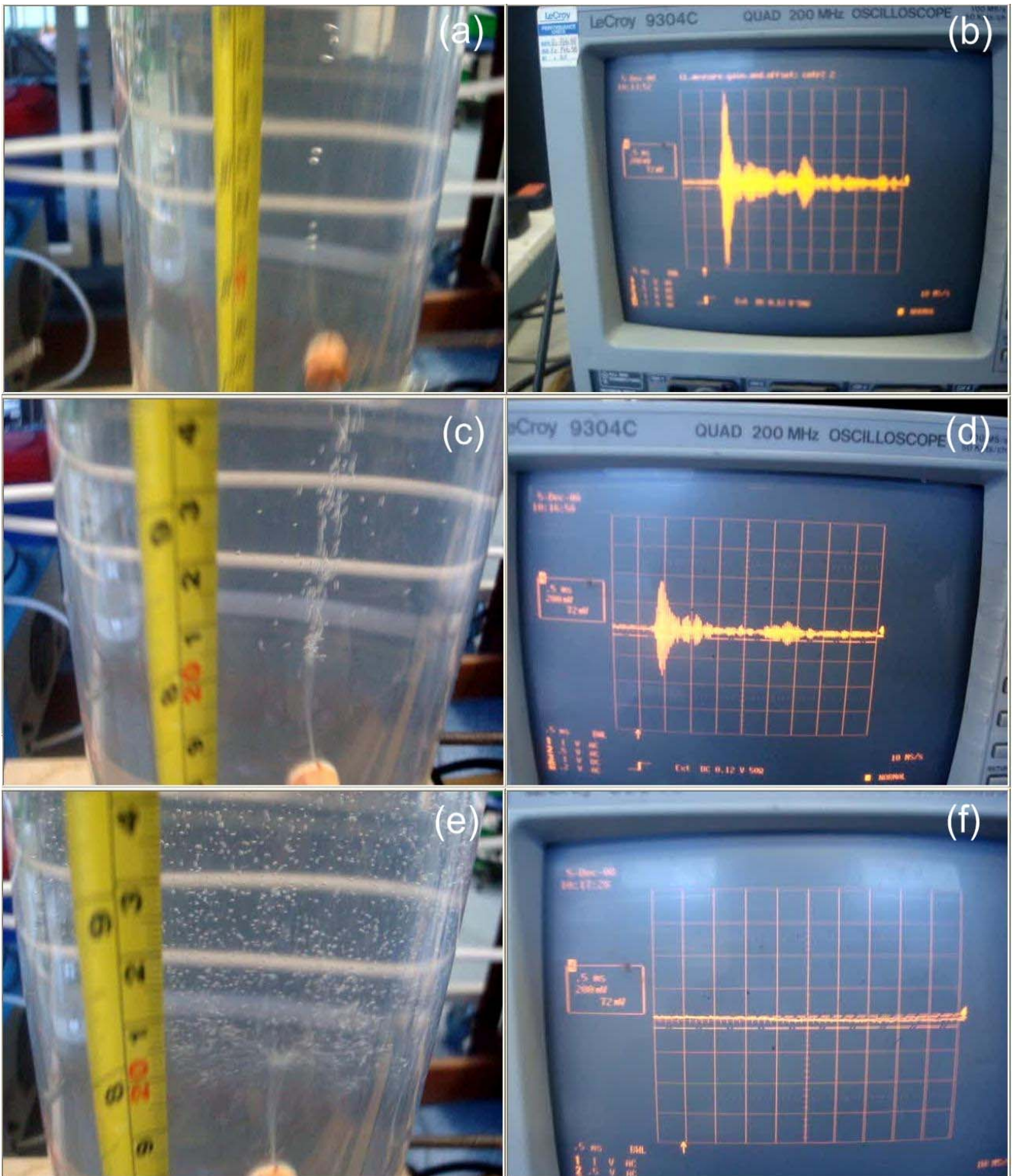


Figure 5.20: Series of photos of the injected bubbles in (a), (c), and (e) and the photos of the corresponding measured pressure by hydrophone shown on the screen of the oscilloscope in (b), (d), and (f). Amplitude change by the number of bubbles is clearly seen in the picture.

The theory of Section III-1 for bubble-free water in the PMMA pipe predicts that each mode suffers from different damping during propagation. Fig. 5.21 is obtained by considering spectrum of path0 contribution in the time series. Hence, it is possible that the spectrum contains several modes in it, that is, this figure only shows the attenuation for the mixed modes. Hence, it is not clear which mode suffers attenuation the most at particular frequency range. In the future, the attenuation of the individual mode needs to be extracted from this figure and the information of that associated with the dispersion curve will be used to infer the bubble spectrum contained in the liquid.

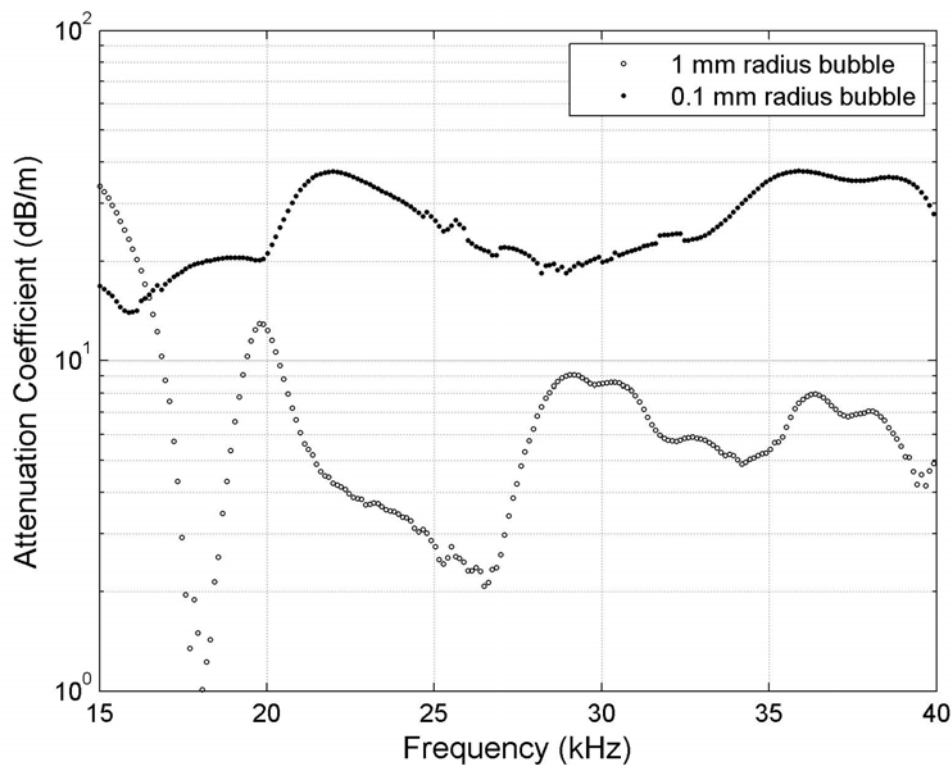


Figure 5.21: Measurement of attenuation coefficient in dB scale. Big bubble and small bubble cases correspond to Figs. 5.17 and 5.19 respectively.

V-5. Bubble spectrum through acoustic inversion

For bubbles in an infinite 3D body of liquid, it is not difficult to infer a bubble spectrum through the inversion algorithm referred in Section III-5. This process requires the regularization to minimize the error caused by ill-posed problem in linear inversion. Figure 5.22 shows the calculated bubble spectrum by using measurement of the attenuation coefficients for the small bubble case (black dots in Fig. 5.21) obtained from Eq. (19). The peak of this bubble spectrum is located around 0.15 mm range

of radius, which is the typical bubble radius for small bubble case as referred in the Fig. 5.19. At the moment, Fig. 5.22 is a preliminary result and several things should be resolved in this bubble spectrum. The main thing is that the algorithm assumes that the bubbles exist in an infinite 3D body of liquid: since the data was taken in a pipe, inaccuracies are expected, and indeed Fig. 5.22 shows an anomalously high density of bubbles of mm size order.

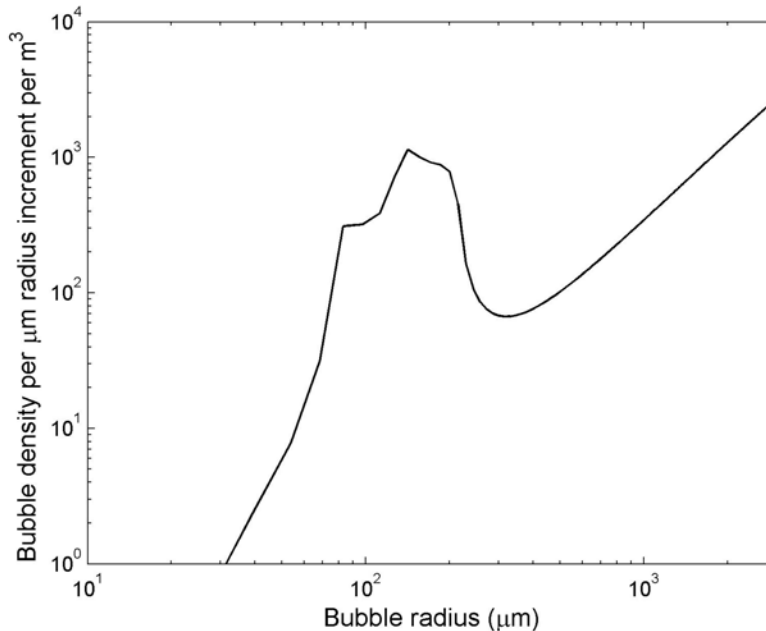


Figure 5.22: Preliminary bubble spectrum obtained from acoustic inversion. Experimental measurement of the attenuation in this calculation is data for small bubble case (shown as black dots in Fig. 5.21).

V-6. Bubble spectrum through μ CORT Method

Bubble distributions were estimated through a new photographic method, named μ CORT (Multi-Color Rising Time), which will be compared with the bubble density spectra obtained by other methods (and used to validate the eventual theory for acoustic propagation in a pipe of bubbly water). It might be thought that photographic imaging represents a straightforward method of counting the number of bubbles taken in the picture with measurement of corresponding size from the image [28]. This can indeed be achieved, provided that one is prepared only to measure accurately over a limited size range, and furthermore it usually requires controlled conditions which favor photography (such that its use in situ is not always easy). Whilst the first restriction is a fundamental result of the compromise between field of view and resolution, the second restriction manifests itself through a range of issues (the need to photograph through curved pipe walls; the presence of spurious reflections and glint from the walls; cracks and distorting imperfections in the pipe). Blurring is also problematic. It is a basic limitation caused by a finite depth of field. Blurring may also be caused by bubble movement, and although to some extent use of a brief flash can mitigate against this, a strong flash can

cause glinting errors (not only in terms of reflections from non-bubble objects which are counted as bubbles, but also because the bubble wall is usually then seen through highlights from the flash, so that when the image is thresholded to measure the bubble size, it is the highlight and not the whole bubble which is counted).

In this project a photographic technique was designed which suffers none of these limitations. The μ CORT method resolves such problem and provides an easy way of counting bubbles across a greatly increased range of radii, with greatly reduced problems caused by limited depth of field and greatly reduced requirements for resolution. Figure 5.23 shows the test rig with μ CORT apparatus. Two strobe lights are mounted at different sides of camera. A picture taken under relatively long exposure of the camera with two successively flash strobe lights of different colors to trace the movement of bubbles in the picture (although indeed the correlation image processing means that the two flashes need not even be of different colour, although this helps greatly for the human eye to visualize how the processing works). A bubble need not be well in focus or well-resolved, since its size is determined from its rise time which can be calculated from a very indistinct image. The detail of this method is described in Appendix E.

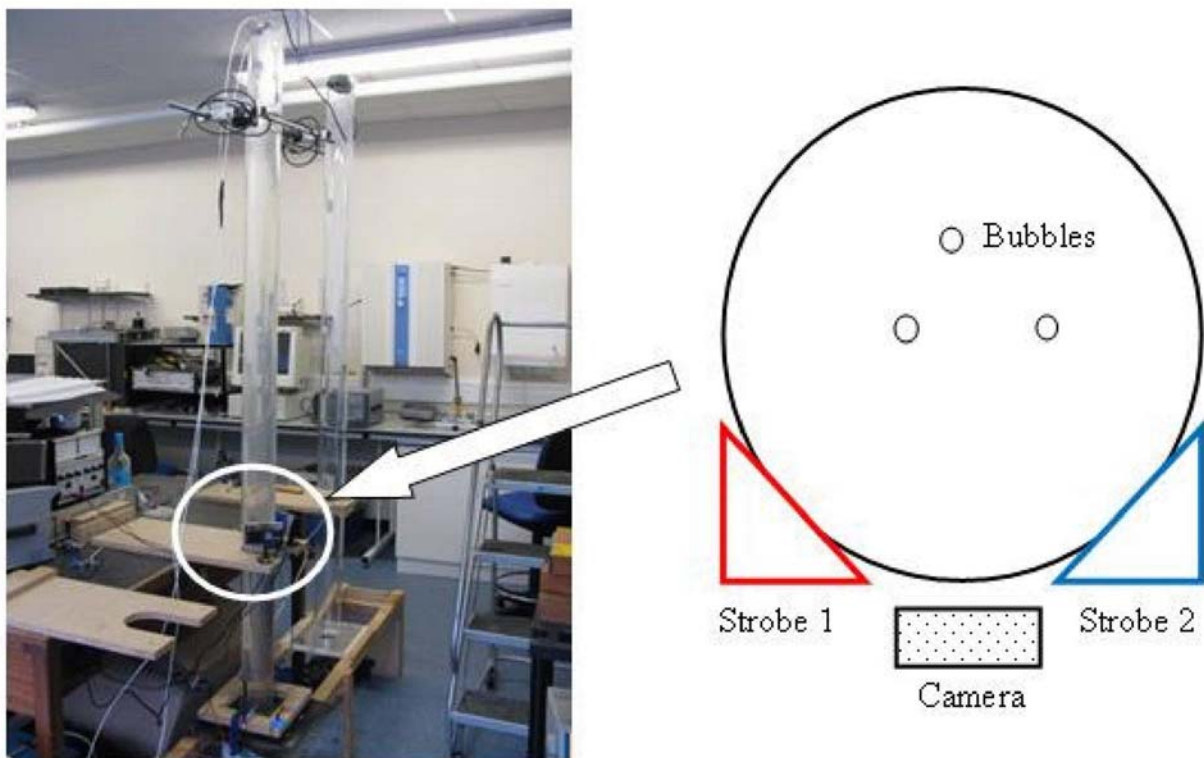


Figure 5.23: Test rig setting up is shown on the left. On the right, a plan view schematic is given for the pip cross-section at the position of the stroboscopes.



Figure 5.24: Original photo taken in experiment with the setup shown in Fig. 5.23.

Figure 5.24 shows an example of the original photo taken in the experiment. From Figure 5.24, the bubble distribution is not even in the tube. Most of them are in the right part of the photo. This is caused by the needle position from where the small bubbles generated. By using the μ CORT method, we obtained the bubble size distribution shown in Figure 5.25 through automated image processing which can rapidly process many frames. The bubbles counted in this images ranged in radius from $60\ \mu\text{m}$ to $1.5\ \text{mm}$, but it can be extended to a range from several μm to several mm , which is a larger size range than imaging techniques provide (e.g. Deane and Stokes [33] detected bubbles photographically in the radius range from 0.2 to $2\ \text{mm}$). The corresponding gas volume void fraction calculated from this distribution is 1.67×10^{-4} . Using this distribution, we can get the extra attenuation which this population would generate in an infinite 3D volume of bubbly water through Eq. (E-1). This attenuation is shown in Figure 5.26 in blue line. This picture also shows the experimental result in red line, as measured in the pipe. Because of the bandwidth limitations of the sound source, we cannot give an experimental result in the frequency band less than $20\ \text{kHz}$. The μ CORT method has only just been developed, and so application of the results is as yet in an early stage. However we expect it to be a powerful tool in obtaining the input bubble distribution for the theory we will develop, a theory which will be validated through measurement of the acoustic sound speed and attenuation in the pipe and, afterwards, inverted to provide estimates of the bubble population in opaque media where μ CORT cannot be used.

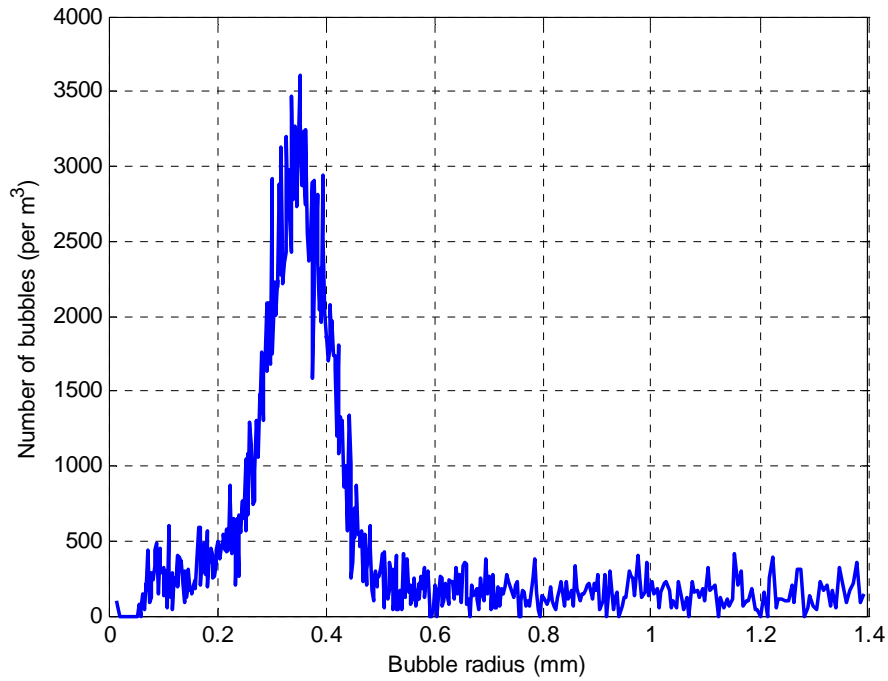


Figure 5.25: Bubble size distribution

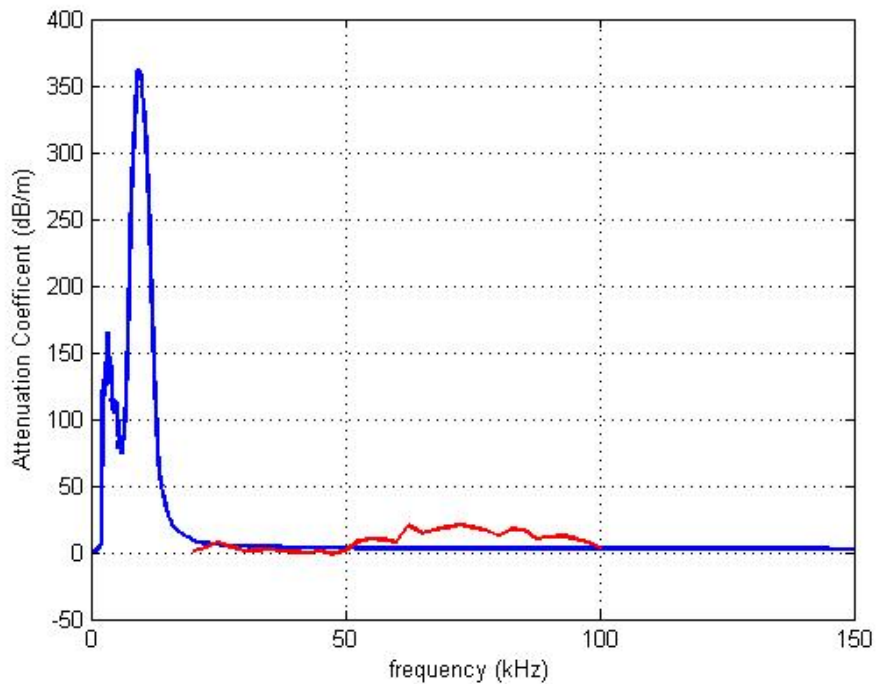


Figure 5.26: Attenuation coefficient indicating the extra attenuation which bubbles would generate compared to bubble free water. The blue line shows the theoretical result by using bubble size distribution obtain by μ CORT method as input for the theory of Eq. (15). Therefore it assumes that all the bubbles exist in an infinite 3D volume of liquid. The red line shows the measured attenuation for the bubbles in the pipe, determined using the phase spectrum method. Therefore the underlying assumptions of the theory do not yet match the experimental results, and the frequency ranges of the two datasets are different.

VI. CONCLUSION AND FUTURE WORK

Theoretical, numerical and experimental investigations have been carried out to lay the foundation for estimating the bubble population in a static PMMA tube which is filled with bubble-free or bubbly water. This was done as the first step to implement techniques for bubble detection in the test rig where liquid circulates inside. Acoustic features in the tube have been examined and tested and the results show that:

1. Owing to the coupling between tube and water, the acoustic signal is dispersive during the propagation;
2. Several modes can be found by checking the 2D pressure spectrum. The dominant mode matches the theoretical ET1 mode when the frequency is greater than 15 kHz. The existence of modes inside the liquid tube was also checked and predicted using a Finite Element model.
3. The $k - \omega$ method can separate the modes in the wave number and angular frequency domain, and give an accurate result focusing on a particular mode.
4. The presence of bubbles suppressed the path1 and higher order reflected waves, affected the wave speed, and caused attenuation of the propagating waves.
5. Bubble distributions were estimated using optical fibre and photographic methods. Phase speed changes and the attenuation coefficients were calculated for bulk bubbly water based on these bubble distributions (using a theory which assumes that the bubbles existed in an infinite 3D body of liquid).
6. Phase velocities and attenuation coefficients were measured in the liquid tube with two different bubble distributions.

Current studies being undertaken in the following areas:

1. Numerical and experimental investigations into the acoustic wave propagation in bubbly-water-filled PMMA tube by combining phase speed or attenuation coefficients in bulk bubbly water with the characteristic equation of the modal dispersion curve in non-bubbly water inside the tube.
2. Upgrading the measurement technique of phase speed and attenuation coefficients by PS method in order to apply the method into the test rig.
3. Acoustic inversion technique to estimation of bubble distribution present inside the tube.
4. Other acoustic techniques for obtaining the bubble size distribution by using multiple transducers.
5. Comparisons and calibrations between bubble spectra obtained from optical fibre method, photographic method, and acoustic inversions.

The longer-term view of this project is that we are on schedule to deliver the contracted bubble sensors to ORNL. Fitting these to the mercury-filled test loop and getting them working is undoubtedly challenging, but we do not foresee at this stage any problems that we should currently be taking steps

to circumvent. Reflecting on the larger activity of mitigating cavitation damage by bubble injection in mercury, one task which is outside of this project, but may require early consideration, is how to provide the mercury with a population of small bubbles within the target section given the high density and surface tension of mercury (see Figure E7, Appendix 7, which qualifies by how much the rise speed of helium bubbles in mercury exceeds that of air bubbles in water, as a function of bubble size).

In the future, experiments will be performed in the test rig which simulates the circulation of the liquid mercury in the Spallation Neutron Source (SNS) system in the Oak Ridge National Laboratory. The following pictures show the current test rig being built at ISVR. Figure 6.1(a) shows the main pipe lines where liquid flows along in the indicated directions. The circled component will, it is hoped, be replaced by a mimic of the test section (see Appendix G), if timing and costs are appropriate. However, because it is specially designed, it needs more time to be completed. Hence, at the moment, the test rig will work using the circled junction shown in Figure 6.1(a). Figure 6.1(b) shows Venturi section (denoted as V) and pressurized reservoir (denoted as R) to generate bubbles in the test rig. The liquid pump (denoted as P) transports the flow between the reservoir and the water tank (denoted as T). A console (denoted as C) controls the activation of this apparatus.

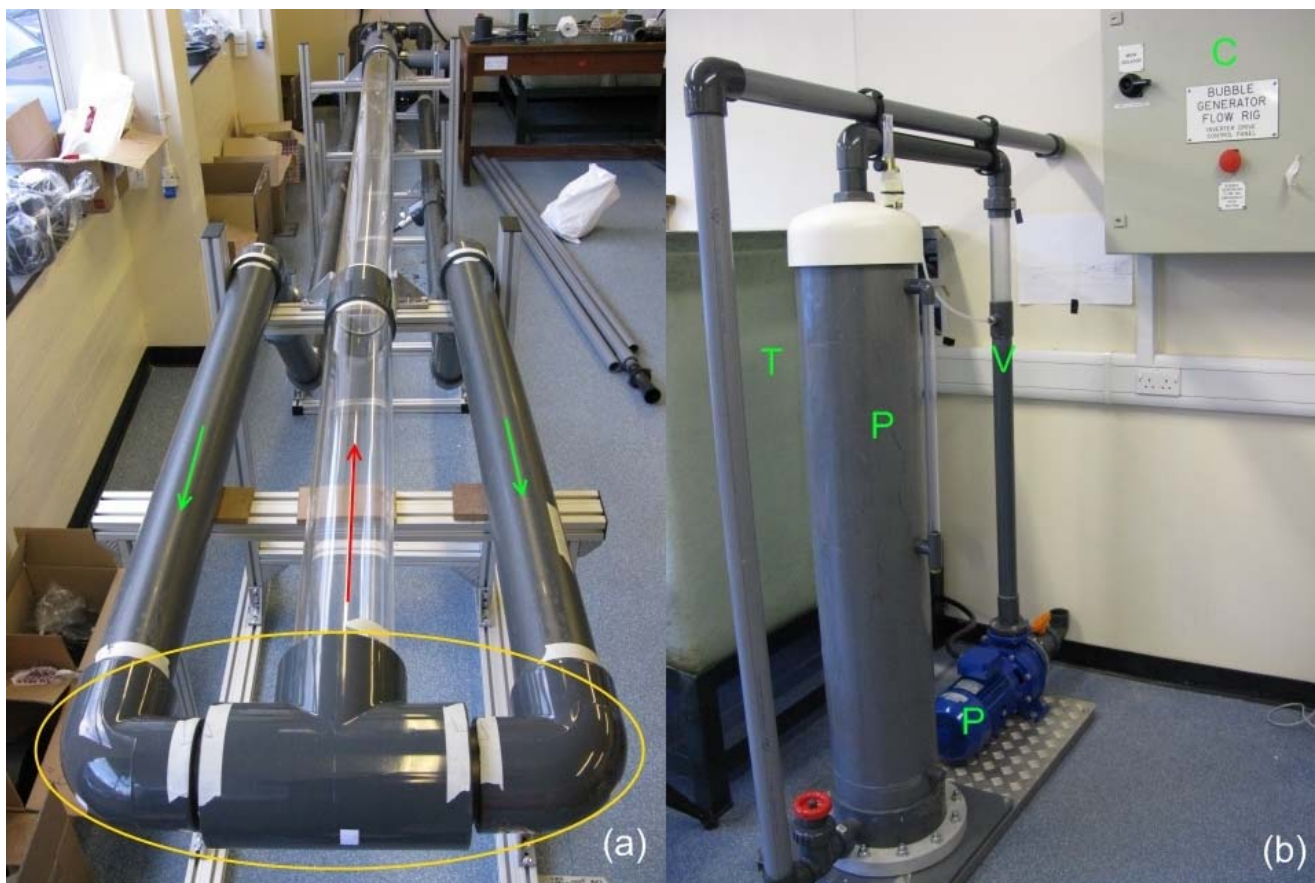


Figure 6.1: (a) Test rig which is being built currently and (b) bubble generating system.

Figure 6.2 shows the water tank which will contain the bubbly mixture that will have been generated by the bubble generator shown in Fig. 6.1(b). On the opposite side of the tank to the bubble generator, which is hidden by the tank, there is a recirculation pump. The upper left corner is a picture of it. Recirculation pump controls the flow between water tank and the flow rig. Hence, there exist two connections associated with the water tank. One is a connection with bubble generator and the other is a connection with the test rig. Water contained in the water tank is transported to bubble generator and bubbles are added in the water after passing through the generator. In the water tank, buoyancy removes the larger bubbles, allowing the smaller bubbles to be pumped into the flow rig.



Figure 6.2: Water tank connected with bubble generator and the test rig. The opposite side of the water tank to the bubble generator which is hidden by the tank is shown at the upper left corner of this photo. Recirculation pump (denoted as RP) circulates bubbly water flow between water tank and the test rig.

Figure 6.3 shows the outlet of the flow which is indicated as red arrow in Fig. 6.1. As told previously, at the end of two inlets and one outlet of the test rig, a chamber will be attached. The size of outlet is bigger than inlets. Bubble detection will be implemented along the outlet and it was made as

transparent in order to see the presence of bubbles inside the tube. At the end of the outlet (indicated as E), a broadband acoustic source will be attached. Four hydrophones, two ultrasonic sources and a receiver for an ultrasonic envelope monitor and a modulation-frequency sensor, and one optical fibre will be installed along the tube indicated as an ellipse. They will be built under the COBUST principle (Characterization Bubbles Using Simultaneous Techniques), where the use of multiple simultaneous sensors provides a more reliable estimate of the bubble population [23, 24].



Figure 6.3: A broad band acoustic source will be attached at the end of outlet of the test rig (denoted as E). Four hydrophones, ultrasonic source and receiver, and optical fiber will be installed along the pipe.

APPENDIX A: DERIVATION OF DISPERSION RELATION

Displacement vector \vec{u} can be expressed in terms of scalar potential ϕ and vector potential $\vec{\psi}$ as $\vec{u} = \nabla\phi + \nabla \times \vec{\psi}$ and they satisfy the Helmholtz equation as shown in Eq. (1). Assuming the z-dependence of each potential as $\exp(ik_z z)$, Eq. (1) is expressed in the axisymmetric cylindrical coordinates as follows [11].

$$\frac{\partial^2 \phi}{\partial r^2} + \frac{1}{r} \frac{\partial \phi}{\partial r} + q_c^2 \phi = 0 \quad (\text{A-1})$$

$$\frac{\partial^2 \psi_r}{\partial r^2} + \frac{1}{r} \frac{\partial \psi_r}{\partial r} + \left(q_s^2 - \frac{1}{r^2} \right) \psi_r = 0 \quad (\text{A-2})$$

$$\frac{\partial^2 \psi_\theta}{\partial r^2} + \frac{1}{r} \frac{\partial \psi_\theta}{\partial r} + \left(q_s^2 - \frac{1}{r^2} \right) \psi_\theta = 0 \quad (\text{A-3})$$

$$\frac{\partial^2 \psi_z}{\partial r^2} + \frac{1}{r} \frac{\partial \psi_z}{\partial r} + q_s^2 \psi_z = 0, \quad (\text{A-4})$$

where $q_c^2 = k_c^2 - k_z^2$ and $q_s^2 = k_s^2 - k_z^2$. Solution of above equation is well known Bessel function. The solutions of Eqs. (A-1) and (A-4) are zeroth order Bessel functions and the solutions of Eqs. (A-2) and (A-3) are first order Bessel functions. Each Bessel function can be expressed either in terms of $J_n(x)$, $Y_n(x)$, and Hankel functions. At any case, denote the Bessel functions of Eq. (A-1) as $\zeta_n(q_c r)$ and the Bessel functions of Eqs. (A-2)-(A-4) as $\xi_n(q_s r)$. Because the term of $\exp[i(k_z z - \omega t)]$ is common at every term, the expression from now on omits that common term. Thus, gradient of the scalar potential in axisymmetric case becomes:

$$\begin{aligned} \nabla \phi &= \frac{\partial \phi}{\partial r} \hat{r} + \frac{\partial \phi}{\partial z} \hat{z} = \phi_0 \frac{\partial \zeta_0(q_c r)}{\partial r} \hat{r} + ik_z \phi_0 \zeta_0(q_c r) \hat{z} \\ &= -q_c \phi_0 \zeta_1(q_c r) \hat{r} + ik_z \phi_0 \zeta_0(q_c r) \hat{z}. \end{aligned} \quad (\text{A-5})$$

The property of the Bessel function such as $\zeta_n'(x) = -\zeta_{n+1}(x) + n/x \zeta_n(x)$ was used in the previous equation. Likewise, curl of the vector potential in axisymmetric case becomes:

$$\begin{aligned} \nabla \times \vec{\psi} &= -\frac{\partial \psi_\theta}{\partial z} \hat{r} + \frac{1}{r} \frac{\partial(r\psi_\theta)}{\partial r} \hat{z} = -ik_z C_2 \xi_1(q_s r) \hat{r} + C_2 \left(\frac{\xi_1(q_s r)}{r} + \frac{\partial \xi_1(q_s r)}{\partial r} \right) \hat{z} \\ &= -ik_z C_2 \xi_1(q_s r) \hat{r} + C_2 q_s \xi_0(q_s r) \hat{z}, \end{aligned} \quad (\text{A-6})$$

where C_i is a constant of each element of vector potential. In the above equation, another property of the Bessel function such as $\xi_n'(x) = \xi_{n-1}(x) - n/x \xi_n(x)$ was used. Therefore, the displacement vector \vec{u} becomes:

$$\vec{u} = -[q_c \phi_0 \zeta_1(q_c r) + i k_z C_2 \xi_1(q_s r)] \hat{r} + [i k_z \phi_0 \zeta_0(q_c r) + C_2 q_s \xi_0(q_s r)] \hat{z}. \quad (\text{A-7})$$

Thus, radial displacement is composed of first order Bessel functions and the axial displacement consists of zeroth order Bessel functions. In cylindrical coordinates, the stress components are described in terms of displacement as:

$$\tau_{rr} = \lambda \left(\frac{\partial u_r}{\partial r} + \frac{u_r}{r} + \frac{1}{r} \frac{\partial u_\theta}{\partial \theta} + \frac{\partial u_z}{\partial z} \right) + 2\mu \frac{\partial u_r}{\partial r}, \quad (\text{A-8})$$

$$\tau_{r\theta} = \mu \left(\frac{1}{r} \frac{\partial u_r}{\partial \theta} + \frac{\partial u_\theta}{\partial r} - \frac{u_\theta}{r} \right), \quad (\text{A-9})$$

$$\tau_{rz} = \mu \left(\frac{\partial u_r}{\partial z} + \frac{\partial u_z}{\partial r} \right), \quad (\text{A-10})$$

where μ and λ are Lamé constants. In the axisymmetric cylindrical coordinates, all the terms derived with respect to angle θ vanishes and the resulting stress components are:

$$\begin{aligned} \tau_{rr} = & -\lambda \phi_0 (q_c^2 + k_z^2) \zeta_0(q_c r) - 2\mu [\phi_0 q_c^2 \zeta_0(q_c r) + i C_2 q_s k_z \xi_0(q_s r)] \\ & + 2\mu \left[\phi_0 \frac{q_c}{r} \zeta_1(q_c r) + i C_2 \frac{k_z}{r} \xi_1(q_s r) \right] \end{aligned} \quad (\text{A-11})$$

$$\tau_{r\theta} = 0 \quad (\text{A-12})$$

$$\tau_{rz} = \mu [-2i \phi_0 q_c k_z \zeta_1(q_c r) + C_2 (k_z^2 - q_s^2) \xi_1(q_s r)] \quad (\text{A-13})$$

Therefore, from Eqs. (A-7), (A-11)-(A-14), in axi-symmetric coordinates, each displacement and tensor element in water (scripted as ‘ ω ’) or in an elastic material (scripted as ‘ e ’) can be expressed as follows.

$$\vec{u}_\omega = -q_\omega [A J_1(q_\omega r) + B Y_1(q_\omega r)] \hat{r} + i k_z [A J_0(q_\omega r) + B Y_0(q_\omega r)] \hat{z} \quad (\text{A-14})$$

$$\begin{aligned} \vec{u}_e = & -\{q_c [C J_1(q_c r) + D Y_1(q_c r)] + i k_z [E J_1(q_s r) + F Y_1(q_s r)]\} \hat{r} \\ & + \{i k_z [C J_0(q_c r) + D Y_0(q_c r)] + q_s [E J_0(q_s r) + F Y_0(q_s r)]\} \hat{z} \end{aligned} \quad (\text{A-15})$$

$$\tau_{rr}^\omega = -\lambda_\omega (q_\omega^2 + k_z^2) [A J_0(q_\omega r) + B Y_0(q_\omega r)] \quad (\text{A-16})$$

$$\tau_{rz}^\omega = 0 \quad (\text{A-17})$$

$$\begin{aligned} \tau_{rr}^e = & -\lambda_e (q_c^2 + k_z^2) [C J_0(q_c r) + D Y_0(q_c r)] \\ & - 2\mu_e \{q_c^2 [C J_0(q_c r) + D Y_0(q_c r)] + i q_s k_z [E J_0(q_s r) + F Y_0(q_s r)]\} \end{aligned} \quad (\text{A-18})$$

$$\begin{aligned} & + 2\mu_e \left\{ \frac{q_c}{r} [C J_1(q_c r) + D Y_1(q_c r)] + i \frac{k_z}{r} [E J_1(q_s r) + F Y_1(q_s r)] \right\} \\ \tau_{rz}^e = & \mu_e \{-2i q_c k_z [C J_1(q_c r) + D Y_1(q_c r)] + (k_z^2 - q_s^2) [E J_1(q_s r) + F Y_1(q_s r)]\} \end{aligned} \quad (\text{A-19})$$

In the geometry of Fig. 3.1, there exist three boundary conditions which above equations should satisfy. Those are continuity of normal displacement and normal stress components, and vanish of shear stress components. At first, think about the vanish of shear stress tensor τ_{rz} . Because water initially satisfies this condition from Eq. (A-17), Eq. (A-19) should be zero either at $r = b$ and $r = d$, which is:

$$C[iq_c k_z J_1(q_c b)] + D[iq_c k_z Y_1(q_c b)] + E[-(k_z^2 - k_s^2/2)J_1(q_s b)] + F[-(k_z^2 - k_s^2/2)Y_1(q_s b)] = 0 \quad (\text{A-20})$$

$$C[iq_c k_z J_1(q_c d)] + D[iq_c k_z Y_1(q_c d)] + E[-(k_z^2 - k_s^2/2)J_1(q_s d)] + F[-(k_z^2 - k_s^2/2)Y_1(q_s d)] = 0, \quad (\text{A-21})$$

which correspond to Eqs. (4b) and (4c) in Lafleur's paper[10]. The remaining two boundary conditions say the continuity of normal displacement and stress. So, at the boundary $r = b$, following relation are satisfied.

$$\begin{aligned} [q_w J_1(q_w b)]A &= [q_c J_1(q_c b)]C + [q_c Y_1(q_c b)]D \\ &\quad + [ik_z J_1(q_s b)]E + [ik_z Y_1(q_s b)]F \quad (\text{A-22}) \\ -[\lambda_w(q_w^2 + k_z^2)J_0(q_w b)]A &= \left[-\lambda_e(q_c^2 + k_z^2)J_0(q_c b) - 2\mu_e q_c^2 J_0(q_c b) + 2\mu_e \frac{q_c}{b} J_1(q_c b) \right] C \\ &\quad + \left[-\lambda_e(q_c^2 + k_z^2)Y_0(q_c b) - 2\mu_e q_c^2 Y_0(q_c b) + 2\mu_e \frac{q_c}{b} Y_1(q_c b) \right] \\ &\quad + \left[-2\mu_e i q_s k_z J_0(q_s b) + 2\mu_e i \frac{k_z}{b} J_1(q_s b) \right] E \\ &\quad + \left[-2\mu_e i q_s k_z Y_0(q_s b) + 2\mu_e i \frac{k_z}{b} Y_1(q_s b) \right] F \quad (\text{A-23}) \end{aligned}$$

Dividing l.h.s. and r.h.s. of Eq. (A-23) by each term of Eq. (A-22), the coefficient A can be eliminated. The resulting expression is complicated but the term associated with coefficient C is similar as the term associated with coefficient D except the substitution of the function J_n with Y_n . it is the same story for the terms associated with E and F . Following term is the term associated with either C obtained from above equations.

$$-[\lambda_e(q_c^2 + k_z^2) + 2\mu_e q_c^2]J_0(q_c b) + \left[2\mu_e \frac{q_c}{b} + \frac{\lambda_w(q_w^2 + k_z^2)q_c J_0(q_w b)}{q_w J_1(q_w b)} \right] J_1(q_c b) \quad (\text{A-24})$$

Because Lamé constants are related to the density ρ , shear velocity C_s , and Poisson's ratio ν such as:

$$\lambda_w = \rho_w C_w^2, \quad \lambda_e = \frac{2\nu}{1-2\nu} \rho_e C_s^2, \quad \mu_e = \rho_e C_s^2. \quad (\text{A-25})$$

Eq. (A-24) can be reduced as follows using the relation of $(C_c / C_s)^2 = 2(1-\nu)/(1-2\nu)$

$$2\rho_e C_s^2 \left[k_z^2 - \frac{k_s^2}{2} \right] J_0(q_c b) + 2\rho_e C_s^2 \left[\frac{1 + Qb}{b} \right] q_c J_1(q_c b), \quad (\text{A-26})$$

where

$$Q = \frac{\rho_w \omega^2 J_0(q_w b)}{2\rho_e C_s^2 q_w J_1(q_w b)}$$

Likewise, the term associated either with E becomes:

$$-2\mu_e i k_z q_s J_0(q_s b) + \left[2\mu_e \frac{i k_z}{b} + i k_z \frac{\lambda_w (q_w^2 + k_z^2) J_0(q_w b)}{q_w J_1(q_w b)} \right] J_1(q_s b) \quad (\text{A-27})$$

and this can be reduced as

$$2\rho_e C_s^2 [-i k_z q_s] J_0(q_s b) + 2\rho_e C_s^2 i k_z \left[\frac{1 + Qb}{b} \right] J_1(q_s b). \quad (\text{A-28})$$

Therefore, following equation is satisfied

$$\begin{aligned} & C \left[P J_0(q_c b) + q_c \frac{1 + Qb}{b} J_1(q_c b) \right] + D \left[P Y_0(q_c b) + q_c \frac{1 + Qb}{b} Y_1(q_c b) \right] \\ & + E \left[-i k_z q_s J_0(q_s b) + i k_z \frac{1 + Qb}{b} J_1(q_s b) \right] + F \left[-i k_z q_s Y_0(q_s b) + i k_z \frac{1 + Qb}{b} Y_1(q_s b) \right] \\ & = 0, \end{aligned} \quad (\text{A-29})$$

which is equivalent to Eq. (4d) in Lafleur's paper. In the above equation $P = k_z^2 - k_s^2/2$. At the boundary $r = d$, elastic material contacts with air or vacuum. In that case, the resulting equation is similar as Eq. (A-30) with substitution of ρ_w with ρ_a embedded in the expression of Q as shown in Eq. (A-26). The script a represents surrounding material. In the ideal case, the system is in vacuum. In the real system, surrounding material may be air. At any case, the density of surrounding substances is zero or tiny, which means $\rho_a \rightarrow 0$. Thus, the term Q vanishes at $r = d$. Therefore, the resulting equation is as follows:

$$\begin{aligned}
& C \left[P J_0(q_c d) + \frac{q_c}{d} J_1(q_c d) \right] + D \left[P Y_0(q_c d) + \frac{q_c}{d} Y_1(q_c d) \right] \\
& + E \left[-i k_z q_s J_0(q_s d) + \frac{i k_z}{d} J_1(q_s d) \right] + F \left[-i k_z q_s Y_0(q_s d) + \frac{i k_z}{d} Y_1(q_s d) \right] \\
& = 0,
\end{aligned} \tag{A-30}$$

which is equivalent to Eq. (4a) in Lafleur's paper[10]. Now, from Eqs. (A-20), (A-21), (A-30), and (A-31), the characteristic equation for non-trivial solutions is determined which is the determinant of 4×4 matrix. The resulting characteristic equation is shown in Eq. (8) in Section III.

All existing modes are denoted as ETm by Del Grosso [9], which means E as an *elastic* wall and T as finite *thickness*. It is helpful to understand the shape of each mode by investigating displacement profile of each mode. Displacement vector in the liquid is as shown in Eq. (A-14) with the constant $B = 0$. Radial vector is described as the first order of Bessel function of the first kind and the axial vector is described as the zeroth order of Bessel function of the first kind. Normalize above with respect to the axial displacement at the center of the cylinder ($r=0$), the normalized displacement becomes:

$$\vec{u}_w^{norm} = \frac{i q_w}{k_z} J_1(q_w r) \hat{r} + J_0(q_w r) \hat{z}, \tag{A-31}$$

Hence, for a given frequency, each mode has certain value of k_z and it is possible to depict the displacement profile as a function of radius r . Figures A1-A8 show this normalized displacements of each mode at certain frequency indicated on each picture. At every picture, (a) shows the magnitude of the normalized radial displacement and (b) shows the magnitude of the normalized axial displacement. From these figures, it is clear that the higher mode, the more number of local maxima or minima in the profile.

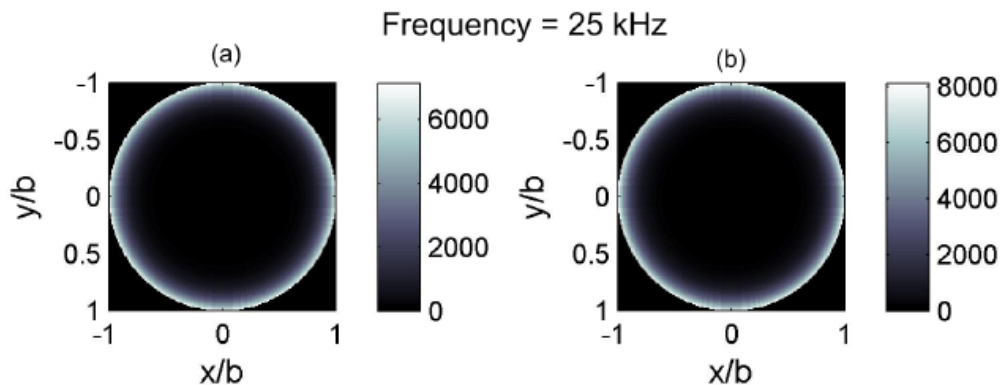


Figure A1: Magnitude of the (a) radial displacement and (b) axial displacement of ET0 mode. Magnitude at this mode increases severely at the interface of the tube wall ($r/b = \sqrt{x^2 + y^2} / b = 1$).

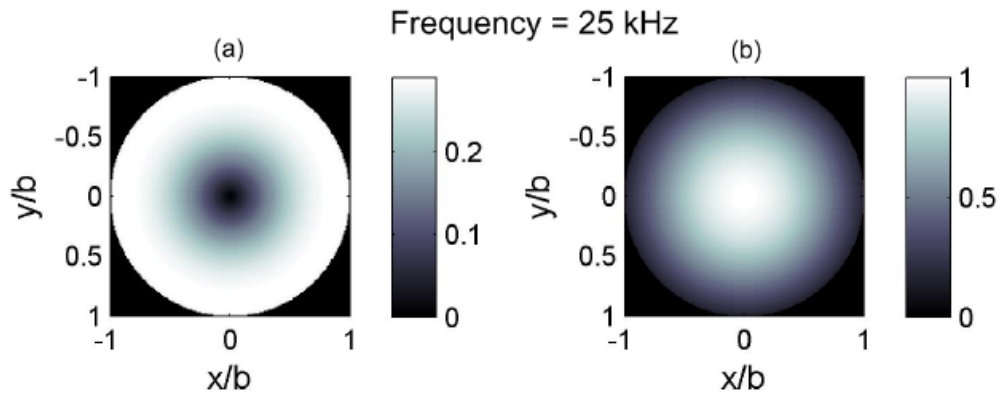


Figure A2: Magnitude of the (a) radial displacement and (b) axial displacement of ET1 mode.

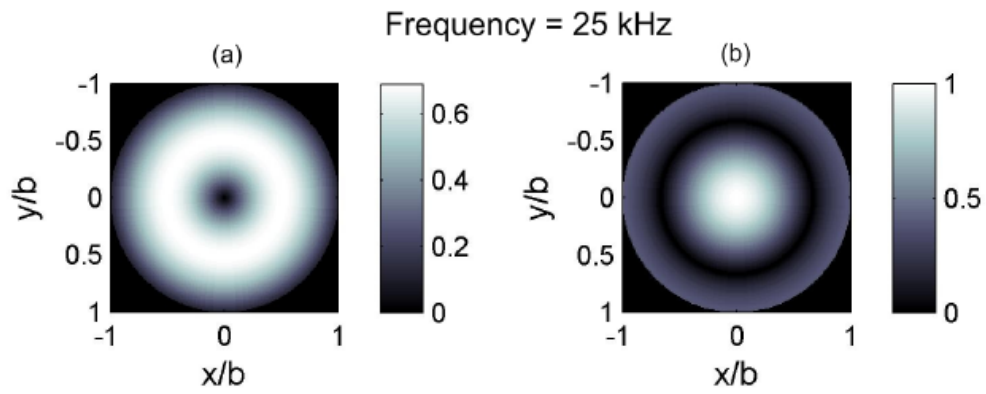


Figure A3: Magnitude of the (a) radial displacement and (b) axial displacement of ET2 mode.

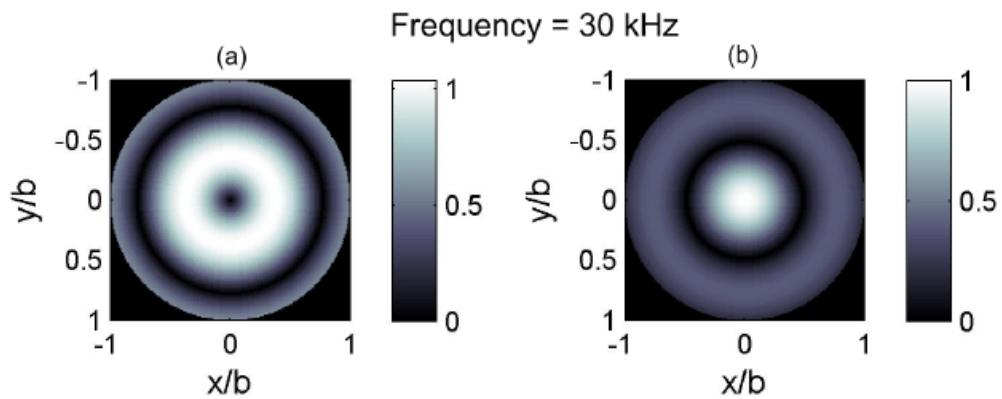


Figure A4: Magnitude of the (a) radial displacement and (b) axial displacement of ET3 mode.

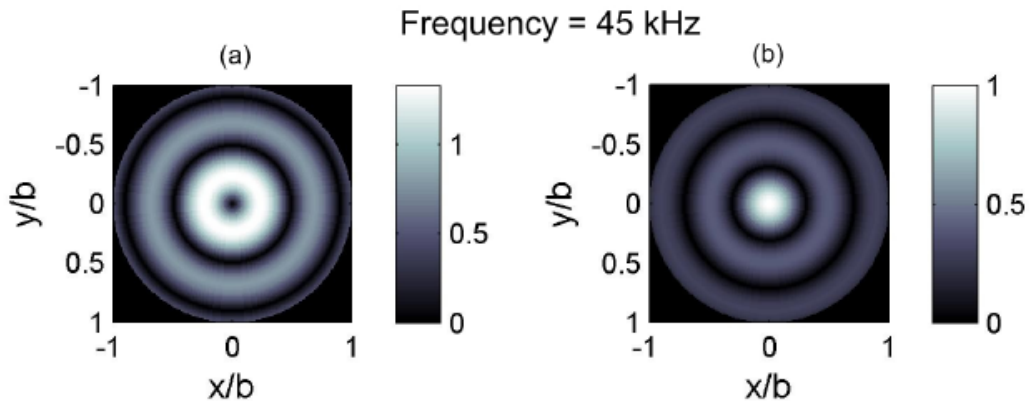


Figure A5: Magnitude of the (a) radial displacement and (b) axial displacement of ET4 mode.

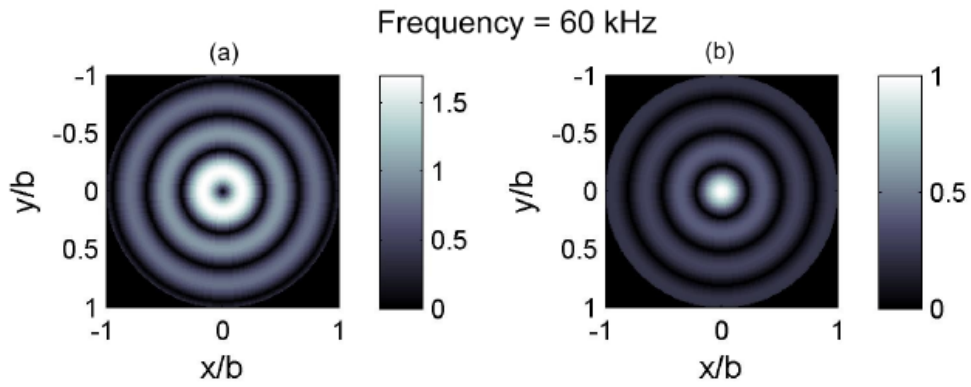


Figure A6: Magnitude of the (a) radial displacement and (b) axial displacement of ET5 mode.

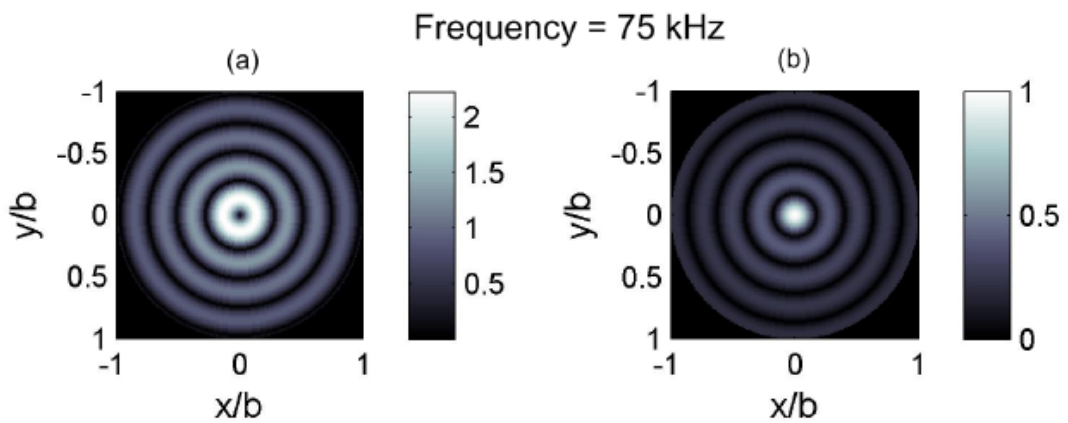


Figure A7: Magnitude of the (a) radial displacement and (b) axial displacement of ET6 mode.

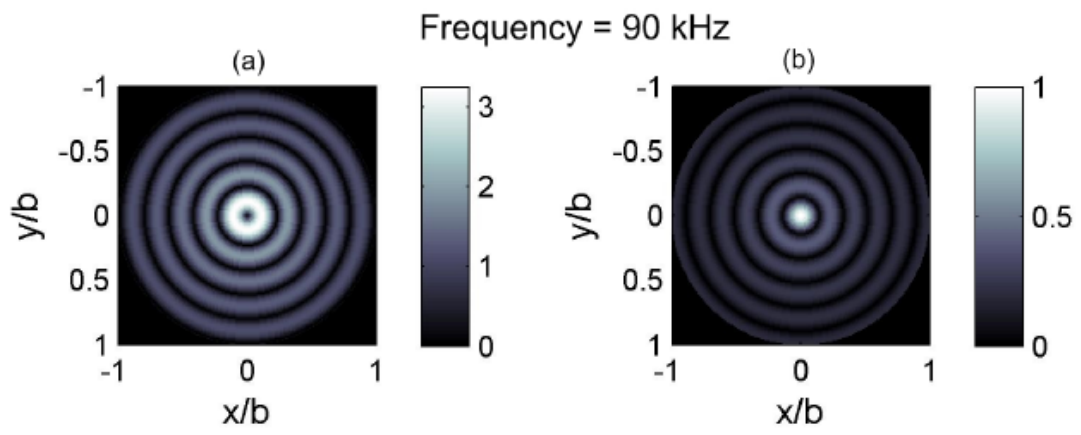


Figure A8: Magnitude of the (a) radial displacement and (b) axial displacement of ET7 mode.

APPENDIX B: CHARACTERISTIC EQUATION AT THE ZERO FREQUENCY LIMIT

At the zero frequency limit, the characteristic Eq. (8) can be reduced as follow, which is the expression shown in Lafleur's paper [10]:

$$Ex^4 + Fx^2 + G = 0, \quad (\text{B-1})$$

where

$$\begin{aligned} x &= k_z/q_w, \\ E &= (3\beta - 4\alpha)y, \\ F &= -4\gamma_0(\beta - \alpha) - [(3\beta - 4\alpha)(1 + \gamma_0) + \beta(\beta - \alpha)]y, \\ G &= \beta^2\gamma_0 + \beta(\beta - \alpha)(1 + \gamma_0)y, \\ \alpha &= (C_w/C_c)^2, \quad \beta = (C_w/C_s)^2, \quad \gamma_0 = \beta\rho_w/\rho_e, \\ y &= \frac{d^2}{b^2} - 1. \end{aligned}$$

It is fourth order polynomial equation and easy to solve because it has perfect quadratic form. Substituting $X = x^2$, above equation is reduced as a simple quadratic equation. Then the maximum number of real solution for X is two. Call those as just a and b . Because $X = x^2$, the solution x becomes $x = \pm a, \pm b$ if a and b are all positive. Because only positive solution has meaning, the maximum number of real solution to Eq. (B-1) is at most two ($+a$ and $+b$). Above corresponds to the Lafleur's result except for the expression of γ_0 . The expression in his paper has typographical error for this quantity, which will be verified in this section.

The small argument approximation of Bessel function is described as [34]:

$$\begin{aligned} J_n(z) &\rightarrow \frac{1}{n!} \left(\frac{z}{2}\right)^n \\ Y_n(z) &\rightarrow \begin{cases} \frac{2}{\pi} [\ln \frac{z}{2} + \delta], & (n = 0) \\ -\frac{(n-1)!}{\pi} \left(\frac{2}{z}\right)^n, & (n > 0) \end{cases} \end{aligned} \quad (\text{B-2})$$

where $\delta = 0.57721\dots$ is Euler-Mascheroni constant. So, at zero frequency limit, evaluating $L_{mn}(z)$ defined in Eq. (B-2), it converges to:

$$\begin{aligned}
L_{00}(z) &\rightarrow \frac{2}{\pi} \ln\left(\frac{b}{d}\right) \\
L_{01}(z) &\rightarrow -\frac{2}{\pi bz} - \frac{bz}{\pi} \left[\ln \frac{dz}{2} + \delta \right] \\
L_{10}(z) &\rightarrow \frac{2}{\pi dz} + \frac{dz}{\pi} \left[\ln \frac{dz}{2} + \delta \right] \\
L_{11}(z) &\rightarrow \frac{1}{\pi} \left(\frac{b}{d} - \frac{d}{b} \right).
\end{aligned} \tag{B-3}$$

At zero frequency limit where $\gamma \rightarrow 0$, the second terms in second and third lines in Eq. (B-3) converge to zero. This can be easily shown by L'hospital's rule. Defining $y = d^2/b^2 - 1$ and substituting this into Eq. (B-3), following expression is obtained.

$$\begin{aligned}
L_{00}(z) &\rightarrow -\frac{1}{\pi} \ln(y+1) \\
L_{01}(z) &\rightarrow -\frac{2}{\pi bz} \\
L_{10}(z) &\rightarrow \frac{2}{\pi dz} \\
L_{11}(z) &\rightarrow -\frac{y}{\pi\sqrt{y+1}}.
\end{aligned} \tag{B-4}$$

Then, using Eq. (B-4), the second term in Eq. (8) is reduced to:

$$[L_{11}(q_c)L_{00}(q_s)] \frac{bd}{2} \left(\frac{\pi k_z q_c q_s}{2P} \right)^2 \rightarrow \frac{bdy \ln(y+1)}{2\pi^2\sqrt{y+1}} \left(\frac{\pi k_z q_c q_s}{2P} \right)^2. \tag{B-5}$$

Using the expression in Eq. (B-1), q_c , q_s , k_z , P can be expressed as:

$$\begin{aligned}
q_c &= \frac{\omega}{C_w} \sqrt{\alpha - x^2}, \quad q_s = \frac{\omega}{C_w} \sqrt{\beta - x^2}, \quad k_z = \frac{\omega}{C_w} x \\
P &= \frac{\omega^2}{C_w^2} \left(x^2 - \frac{\beta}{2} \right).
\end{aligned} \tag{B-6}$$

Hence, in the zero frequency limit, Eq. (B-5) becomes:

$$\lim_{\omega \rightarrow 0} \frac{bdy \ln(y+1)}{2\pi^2 \sqrt{y+1}} \left(\frac{\pi\omega x \sqrt{\alpha-x^2} \sqrt{\beta-x^2}}{2C_w(x^2-\beta/2)} \right)^2 \rightarrow 0, \quad (\text{B-7})$$

because it is linear function of frequency. Likewise, the third term in Eq. (8) also approaches zero in the zero frequency limit. The fourth term in Eq. (8) becomes:

$$\begin{aligned} & [L_{10}(q_c)L_{01}(q_s) + L_{01}(q_c)L_{10}(q_s)] \left(\frac{bd\pi^2 q_c q_s}{8} \right) \\ & \rightarrow \left[-\frac{4}{\pi^2 bd q_c q_s} - \frac{4}{\pi^2 bd q_c q_s} \right] \times \left(\frac{bd\pi^2 q_c q_s}{8} \right) = -1. \end{aligned} \quad (\text{B-8})$$

The quantity Q in the fifth term in Eq. (8) is defined in Eq. (7) and it approaches following expression at zero frequency limit using the expression in Eq. (B-1).

$$Q \rightarrow \frac{\rho_w \omega^2}{\rho_e C_s^2 q_w^2 b} = \frac{\gamma_0}{b(1-x^2)}, \quad (\text{B-9})$$

where $\gamma_0 = \beta \rho_\omega / \rho_e$ and related to the quantity γ in Lafleur's paper [10] as $\gamma_0 = \beta^2 / \gamma$. The fifth term in Eq. (8) becomes:

$$\begin{aligned} & [bL_{11}(q_c)L_{10}(q_s) + d(1+Qb)L_{11}(q_c)L_{01}(q_s)] \left(\frac{\pi^2 q_c^2 q_s}{8P} - \frac{\pi^2 q_c^2 k_z^2 q_s}{8P^2} \right) \\ & \rightarrow \left[-\frac{2by}{\pi^2 dq_s \sqrt{y+1}} + d \left(1 + \frac{\gamma_0}{1-x^2} \right) \frac{2y}{\pi^2 b q_s \sqrt{y+1}} \right] \left(\frac{\pi^2 q_c^2 q_s}{8P} - \frac{\pi^2 q_c^2 k_z^2 q_s}{8P^2} \right) \\ & = -\frac{\beta y (\alpha - x^2) [y(1-x^2) + \gamma_0(y+1)]}{8(y+1)(1-x^2)(x^2-\beta/2)^2}. \end{aligned} \quad (\text{B-10})$$

Likewise, the remaining sixth and seventh terms in Eq. (8) become:

$$[bL_{11}(q_s)L_{10}(q_c) + d(1 + Qb)L_{11}(q_s)L_{01}(q_c)] \left(\frac{\pi^2 q_c q_s}{8k_z^2} - \frac{\pi^2 q_c}{8} \right) \rightarrow -\frac{\beta y [y(1 - x^2) + \gamma_0(y + 1)]}{8x^2(y + 1)(1 - x^2)} \quad (\text{B-11})$$

$$[(1 + Qb)L_{11}(q_s)L_{11}(q_c)] \left(\frac{\pi^2 q_c^2}{8k_z^2} + \frac{\pi^2 q_c^2 k_z^2}{8P^2} - \frac{\pi^2 q_c^2}{4P} \right) \rightarrow \frac{\beta^2 y^2 (\alpha - x^2) [(1 - x^2) + \gamma_0]}{32x^2(y + 1)(1 - x^2)(x^2 - \beta/2)^2}. \quad (\text{B-12})$$

Therefore, Eq. (8) becomes:

$$1 - 1 - \frac{\beta y (\alpha - x^2) [y(1 - x^2) + \gamma_0(y + 1)]}{8(y + 1)(1 - x^2)(x^2 - \beta/2)^2} - \frac{\beta y [y(1 - x^2) + \gamma_0(y + 1)]}{8x^2(y + 1)(1 - x^2)} + \frac{\beta^2 y^2 (\alpha - x^2) [(1 - x^2) + \gamma_0]}{32x^2(y + 1)(1 - x^2)(x^2 - \beta/2)^2} = 0. \quad (\text{B-13})$$

Above equation can be rewritten as:

$$4[x^2(\alpha - x^2) + (x^2 - \beta/2)^2][y(1 - x^2) + \gamma_0(y + 1)] - \beta y (\alpha - x^2) [(1 - x^2) + \gamma_0] = 0. \quad (\text{B-14})$$

Arranging above equation in terms of the power of x,

$$(3\beta - 4\alpha)yx^4 - \{4\gamma_0(\beta - \alpha) + [(3\beta - 4\alpha)(1 + \gamma_0) + \beta(\beta - \alpha)]y\}x^2 + \beta^2\gamma_0 + \beta(\beta - \alpha)(1 + \gamma_0)y = 0. \quad (\text{B-15})$$

Hence, solving Eq. (B-15) for the aluminum case in Lafleur's paper, the normalized phase velocity $1/x$ becomes 0.9213 and 3.5085 respectively. This corresponds to Fig. 3 in his paper and resolves the discrepancy caused by his original expression. Solving above for the PVC case in Lafleur's paper, the solution becomes $1/x = 0.2724, 1.0044$ and it's closer to Fig. 4 than the previous solution obtained. So, it is certain that Eq. (B-15) is the correct expression for the characteristic equation in zero frequency limit. Applying this to our PMMA tube, the solution becomes $1/x = 0.3426, 1.5517$. Comparing this result with Fig. 2.2, the solution 1.5517 and 0.3426 correspond to the theoretical curves in the figure.

APPENDIX C: DERIVATION OF SOUND SPEED IN BUBBLY MIXTURE

Denote Γ as gas volume fraction. Then, the average density of the mixture can be written as

$$\rho_m = \rho_w(1-\Gamma) + \rho_g\Gamma, \quad (\text{C-1})$$

where ρ_w and ρ_g are densities of liquid and gas respectively. Compressibility of the material, κ , is defined by

$$\kappa = -\frac{1}{V} \frac{\Delta V}{\Delta p}, \quad (\text{C-2})$$

where V is volume of the material and $\Delta p = -P_A e^{i\omega t}$ is pressure change and P_A is magnitude of acoustic pressure. Suppose there exist n_b identical bubbles per volume and each bubble has a volume of $V_1(t)$. Since, bubbles under the excitation of acoustic source is not stable, volume of each bubble is a function of time. Then, the compressibility of the bubbles can be expressed

$$\kappa_b = \frac{n_b \Delta V_1(t)}{P_A e^{-i\omega t}}, \quad (\text{C-3})$$

Assuming all the bubbles are spherical and change of the bubble volume from its equilibrium radius, R_0 , as tiny, the change of the volume of each bubble can be approximated as

$$\Delta V_1(t) \approx 4\pi R_0^2 R_d, \quad (\text{C-4})$$

where R_d is displaced radius. Pulsating bubbles can be described in terms of a linear forced damped oscillator as follows.

$$\ddot{R}_d + 2\beta\dot{R}_d + \omega_0^2 R_d = \frac{P_A 4\pi R_0^2}{m} e^{i\omega t}, \quad (\text{C-5})$$

where β is total damping parameter described in Section III-2, ω_0 is resonance frequency, and $m = 4\pi R_0^3 \rho_w$ is radiation mass. Assuming time dependence of R_d as $e^{i\omega t}$, displaced radius R_d can be obtained from Eq. (C-5) as follows.

$$R_d = \frac{P_A e^{i\omega t}}{\rho_w R_0} \frac{1}{\omega_0^2 - \omega^2 + 2i\beta\omega}, \quad (\text{C-6})$$

Then, substituting Eqs. (C-4) and (C-6) into Eq. (C-3), the expression for the compressibility of bubbles is reduced to:

$$\kappa_b = \frac{4\pi R_0 n_b}{\rho_w (\omega_0^2 - \omega^2 + 2i\beta\omega)}, \quad (\text{C-7})$$

Thus, speed of sound in the bubble mixture, c_m , can be approximated as:

$$\frac{1}{c_m^2} = [\gamma\rho_g + (1-\gamma)\rho_w] [\kappa_w + \kappa_b] \approx \rho_w \left[\frac{1}{\rho_w c_w^2} + \frac{4\pi R_0 n_b}{\rho_w (\omega_0^2 - \omega^2 + 2i\beta\omega)} \right], \quad (\text{C-8})$$

Arranging above equation, finally, we can get the following equation which is identical to Eq. (36) of the reference [15] for the single distribution bubbly media.

$$\frac{c_w^2}{c_m^2} \approx 1 + \frac{4\pi c_w^2 R_0 n_b}{\omega_0^2 - \omega^2 + 2i\beta\omega}, \quad (\text{C-9})$$

For the mixed distribution of bubbles in the media, above equation is expressed in terms of integral with respect to bubble spectrum.

APPENDIX D: MEASUREMENT OF BUBBLES USING OPTICAL FIBER

Figure D1 shows the block diagram for the measurement of the bubbles using optical fiber. Air compressor injects gas to generate bubble inside the cylindrical tube filled with water. At the open end of the tube, an optical fiber is mounted in which the invisible light is propagating. The tip of the optical fiber has conical shape which is specially produced. Refractive index of the optical fiber was especially chosen so that when there is no bubble, propagating light is transmitted through the water and if there exists bubble which touches the optical fiber, then the light is reflected back through the fiber. Refractive index and the apex angle of the fiber are set as special which satisfies the internal reflection condition when bubble touches the tip of the fiber. Reflected light is measured by the oscilloscope and the trace is stored into the PC.

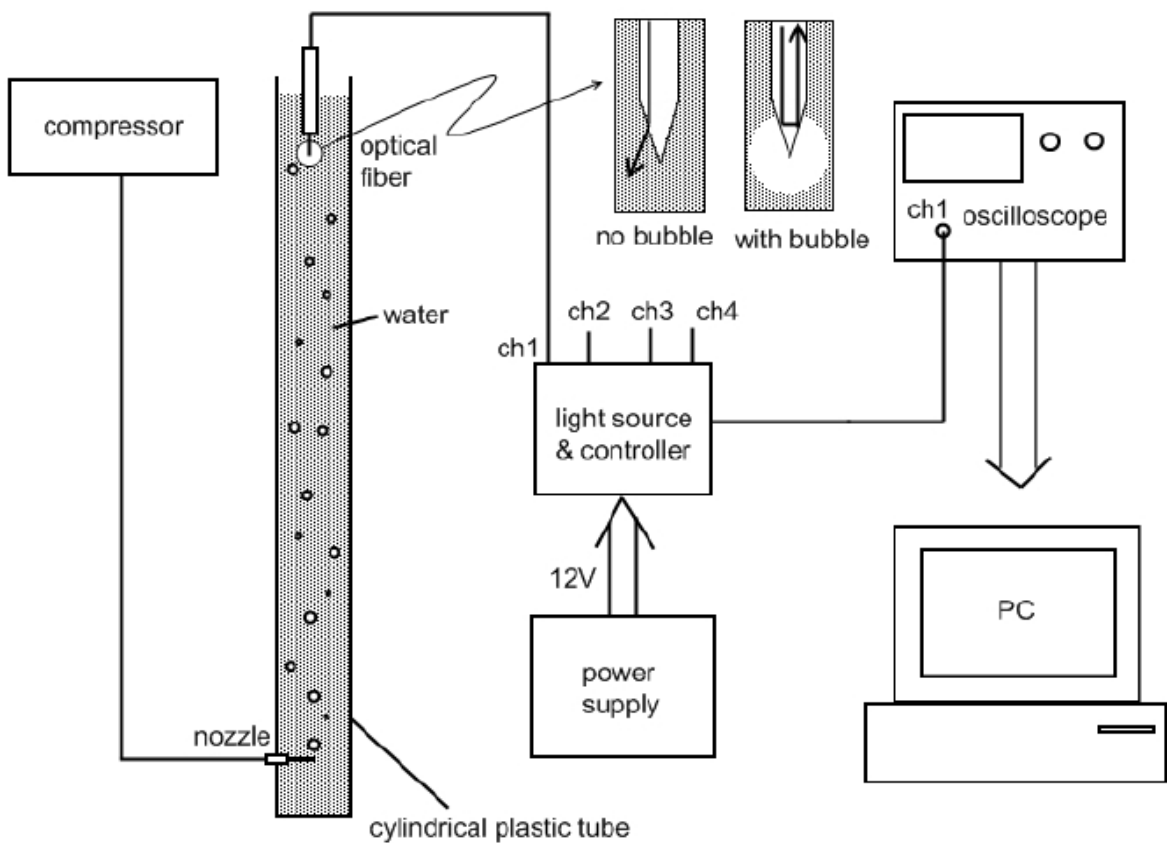


Figure D1: Block diagram for bubble detection using optical fiber.

Figure D2 shows the shape of the tip and the conventional signal shown in the oscilloscope when a bubble is detected by the optical fiber. When bubble touches the tip of the optical fiber, the typical voltage profile of the signal is formed as shown in the figure. Time T_G is duration of the plateau and T_u is rising time of the signal. Define the length and the diameter of the tip as L_a and D_a respectively. Then the bubble radius R_0 can be estimated as [35-36]:

$$2R_0 = \frac{3L_a T_G}{2T_u}, \quad (\text{D-1})$$

The factor 1.5 on the right hand side of the equation is average correction factor to get the approximate bubble size [37-38]. So, repeating the measurement many times, different values of R_0 is obtained and calculated by Eq. (D-1). Then, it is possible to make a distribution of total number of bubbles recorded, $N(R_0)$, as a function of equilibrium bubble radius R_0 . Suppose the cross section of the tip of the optical fiber $A = \pi D_a^2 / 4$. Then, bubble density per unit volume, n_b , is [35-36]:

$$n_b(R_0) = \frac{N(R_0)}{v_t T A}, \quad (\text{D-3})$$

where v_t is terminal velocity of the bubbles and T is total measurement time. Terminal velocity is proportional to the bubble size. Generally, the bigger bubble, the higher speed of v_t when bubbles rise up. However, how the speed v_t is related to the bubble radius inside the tube is not known. Instead, for a given bubble size, terminal velocity is estimated from the distribution of the terminal velocity as a function of bubble size [39]. Suppose the time range for one measurement as T_w and m number of data were successively taken. Then, the total measurement time T is the same as mT_w .

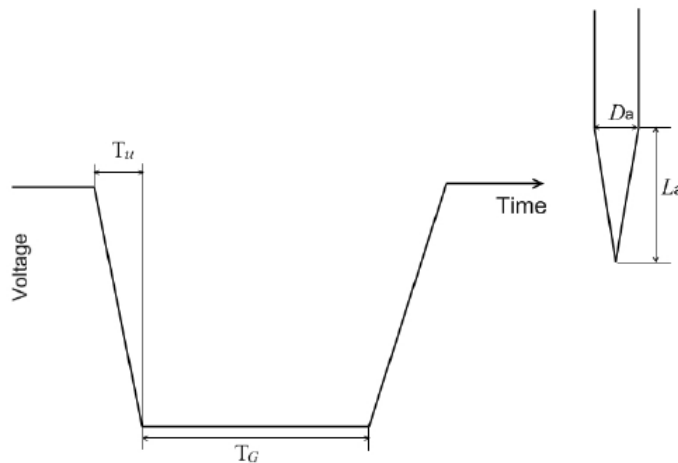


Figure D2: Typical signal recorded by the optical fiber system. This signal associated with the dimension of the fiber determines the bubble size distribution.

Suppose bubbles are introduced with the constant time period T_b and the total number of the introduced bubbles at each time period as n_t . When bubbles are introduced, there is a distribution as a function of bubble size. Because big bubbles generally rise up more quickly than small bubbles, the speed of bubble, ν , is proportional to the bubble size. Hence, bubble distribution by bubble size can be inverted as bubble distribution by ν and it can be expressed as a density function, $g(\nu)$, where $\sum g(\nu) = 1$. Suppose the number of bubbles which have the speed of ν at each introduction as $n(\nu)$.

Then, $\sum n(\nu) = n_t$. From this relation, density function $g(\nu) = n(\nu)/n_t$.

Figure D3 shows an example of measurements when a distribution of bubbles was introduced. Several ideal assumptions are included in this picture.

- 1) Density function $g(\nu)$ is identical at every introduction of bubbles.
- 2) Bubbles do not suffer coalescence or fission during rising up.
- 3) Bubbles rise up with constant speed of ν within the length of investigation L . This also means there is no change of bubble size during rising up because constant speed ν means constant bubble size.

Measurement starts after sufficient time when the measured bubble distribution at the measurement position is identical at every time period, which is shown in Fig. D3. For simple calculation, suppose there exist two size of bubbles in the tube and the length L is chosen close to the multiple of either $\nu_1 T_b$ or $\nu_2 T_b$ where ν_1 and ν_2 are rising speed of big and small bubbles. When the measurement is performed at this stage, the counted bubble distribution is identical to $n(\nu) = n_t g(\nu)$, that is, $n(\nu_1) = 3$, $n(\nu_2) = 1$ and $n_t = 4$. However, bubble distribution all through the volume is different from this. Suppose the total number of bubbles in the volume with speed ν as $N_v(\nu)$. Then, from the figure, $N_v(\nu_1) = 6$ and $N_v(\nu_2) = 4$, that are different from $n(\nu_1)$ and $n(\nu_2)$ respectively. As can be seen in the figure, the number of total bubbles inside the volume is proportional to the quantity $L/(\nu T_b)$. In this figure $L/(\nu_1 T_b) \approx 2$ and $L/(\nu_2 T_b) \approx 4$. Therefore, $N_v(\nu)$, can be expressed as:

$$N_v(\nu) = \frac{n(\nu)L}{\nu T_b} = n_t \frac{g(\nu)L}{\nu T_b}, \quad (D-3)$$

and the total number of bubbles inside the volume, N_t becomes $N_t = \sum N_v(\nu)$. Therefore, the density function $G(\nu)$ for all the volume becomes:

$$G(\nu) = \frac{N_\nu(\nu)}{N_t} = \frac{n_t}{N_t} \frac{g(\nu)L}{\nu T_b}, \quad (\text{D-4})$$

Using the equations, calculating $g(\nu)$ and $G(\nu)$ for bubbles in the figure:

$$\begin{aligned} g(\nu_1) &= \frac{3}{4}, & g(\nu_2) &= \frac{1}{4}, \\ G(\nu_1) &= \frac{n_t}{N_t} \frac{g(\nu_1)L}{\nu_1 T_b} \approx \frac{4}{10} \frac{3}{4} \frac{L}{L/2} = \frac{6}{10}, \\ G(\nu_2) &= \frac{n_t}{N_t} \frac{g(\nu_2)L}{\nu_2 T_b} \approx \frac{4}{10} \frac{1}{4} \frac{L}{L/4} = \frac{4}{10}. \end{aligned} \quad (\text{D-5})$$

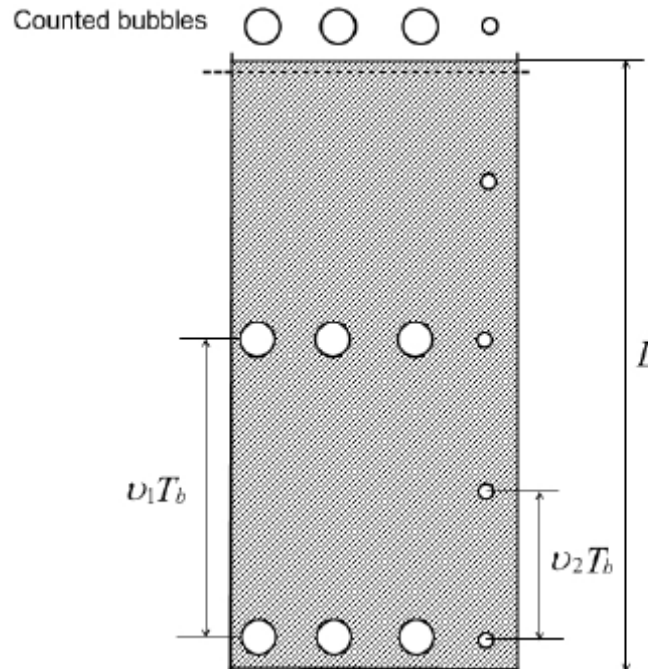


Figure D3: The moments when the measurement is performed.

Thus, the measured density $g(\nu)$ (Local BSD) is different from the density all through the volume, $G(\nu)$ (Global BSD), unless there is only one size of bubble inside the volume. Therefore, the measured density $g(\nu)$ should be inverted to $G(\nu)$ in order to represent the correct bubble distribution in the volume by using Eq. (D-3). Now, looking back the formula, Eq. (D-2) used in the optical fiber method for the calculation of the BSD, it is possible to check if Eq. (D-2) represents the

local BSD or global BSD. From Eq. (D-3), the number of bubbles with speed of ν per unit volume, $n_b(\nu)$ is:

$$n_b = \frac{N_t G(\nu)}{A_t L} = \frac{n_t g(\nu)}{\nu T_b A_t} = \frac{n(\nu)}{\nu T_b A_t}, \quad (\text{D-6})$$

where A_t is cross section of the pipe. When the measurement is repeated m times, such that $T = mT_b$,

$$n_b = \frac{mn_t g(\nu)}{\nu mT_b A_t} = \frac{mn(\nu)}{\nu T A_t} = \frac{N(\nu)}{\nu T A_t}, \quad (\text{D-7})$$

Eq. (D-7) is identical to Eq. (D-2) as far as bubbles are distributed uniformly over the area so that detected numbers of bubbles per unit area are the same in both cases when the measurements are performed through the cross section of the fiber and the tube. Hence, optical fiber method represents the global BSD, $G(\nu)$. Because three assumptions are not valid in the real system, Eq. (D-7) may be true only within the limited length of the interest L in the figure. When local BSD $g(\nu)$ is changing at every introduction of bubbles, Eq. (D-7) is not valid anymore. Instead, it can give the averaged global BSD over a certain amount of the time.

APPENDIX E: μ CORT(MULTI-COLOR RISING TIME) METHOD

The motivation of using a non-acoustic method to estimate the bubble population in this project is to check the correctness of acoustic method. Importantly, it can provide an independent measure of the input bubble distribution for the theory we will develop, a theory which will be validated through measurement of the acoustic sound speed and attenuation in the pipe and, afterwards, inverted to provide estimates of the bubble population in opaque media where the non-acoustical cannot be used. An optical method seems a good choice for a non-acoustic technique, because of its independency from acoustic signal and the advantage of easy implementation. Although the principle of optical imaging is easy to understand, and we can 'by' eye gain a satisfactory impression of the bubbles in the field of view, its limitations can be surprising.

For example, to see small bubbles to sufficient resolution, the field of view and depth of field will be small. This means that only a limited bubble size range can be submitted for automatic processing from a single camera setting, and of those it is important to discard the bubbles which are not in focus. Furthermore, non-bubble artefacts (cracks and imperfections in PMMA, specular glints from curved surfaces) can be interpreted as bubbles, and because the bubble wall is curved, the 'glint' which tells us that a bubble is present will be much smaller than the cross-section of the bubble. All these aspects make image processing (the only viable method for dealing with populations of many bubbles) difficult and prone to misleading results.

That is not to say that recent decades have not seen great advances in the photography of small numbers of bubbles (usually constrained to a particular position to keep them in focus). Rapid developments of camera technique and imaging processing methods in the past several years have for example made it possible to observe single bubbles as small as 1 μm (usually constrained to specific locations at the camera focus). However, the traditional optical method of estimating the bubble population by automatically calculating the area of bubble images on photo has errors in estimating bubble size, because the bubble may not show its full image on the photo. Most of the time only the reflecting part can be clearly recognized. To overcome this problem, here, we use rising speed to estimate bubble size, due to the fact that bubbles in different sizes have different rising speed. We use the documented relationships between bubble size and rise speed which fully consider the bubble dynamics and the characteristics of surrounding media [39].

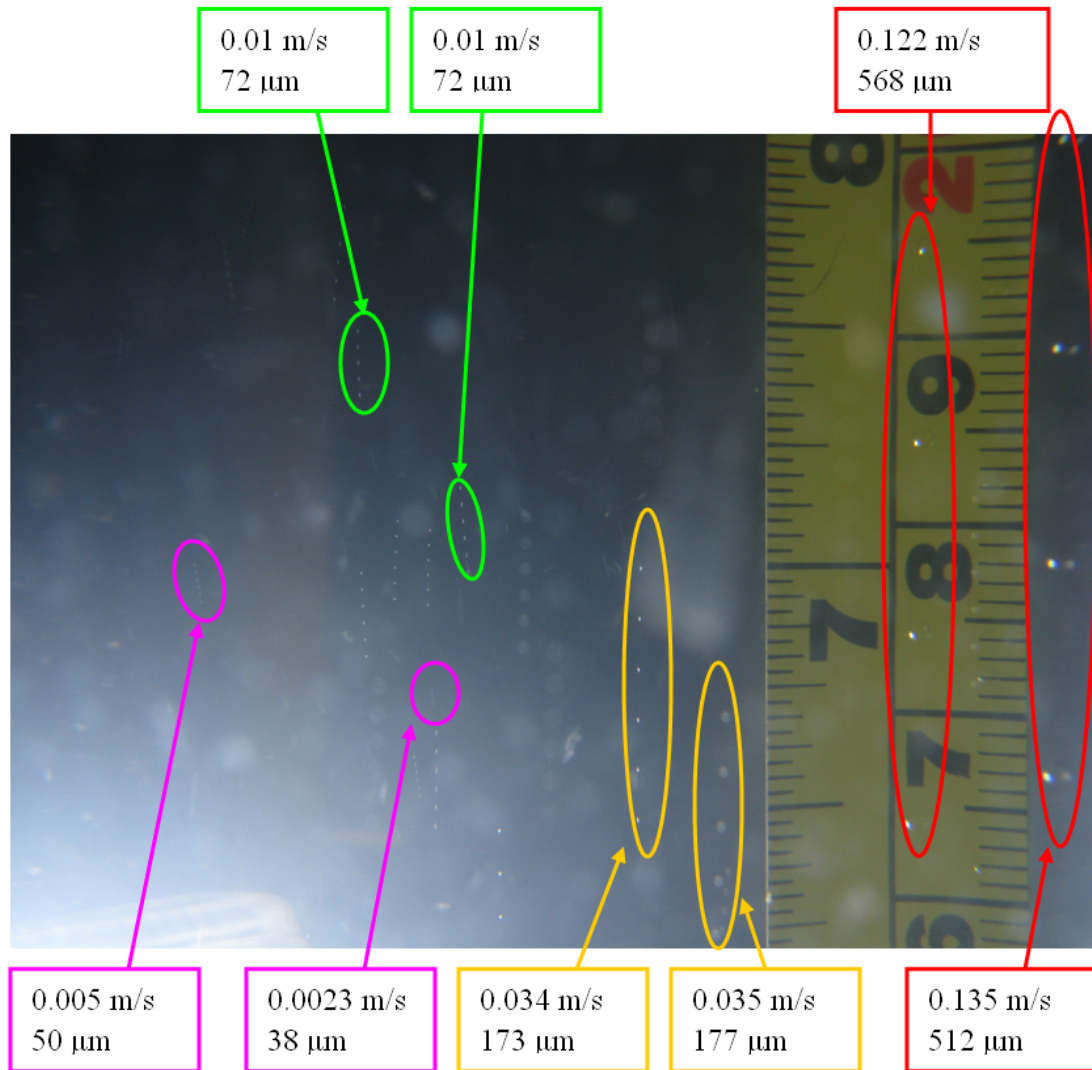


Figure E1: Bubbles in different size rising in water, as imaged by a stroboscope which emitted size flashes in the frame. Each bubble provides an almost vertical trail of 6 images, from which the rise speed can be clearly determined (even though none of the bubbles in the image are sufficiently well-resolved to determine its size from the image directly).

Clift *et al.* [39] provides a summary relationship between bubble size and rise speed which has proved to be correct by many applications and experiments. More detail of this curve is given later in this Appendix. To use this curve, we need to know the exact rising speed of each bubble showing in the photo. A strobe light which has a constant flashing rate can give us several images for the same bubble on a photo if the shutter time of camera is long enough. An example is shown in Figure E1. Each of them shows 6 images in the photo (some of the bubbles are circled), except the two large bubbles on the right, who have run out of the photo during the shutter time. For Figure E1, the flashing rate is 12 Hz, and the shutter time is 0.5 s. By checking the distance of bubble displacement between two flashes, bubble rising speed can be obtained. The rising speed of each bubble is also shown on the photo. They can then be converted to bubble size by using the rise-speed/radius curve mentioned above.

However, this method also has a shortcoming. If there are more bubbles in the water, their images may overlap. This makes the photograph difficult to interpret as the bubble population becomes more dense (although note that simple imaging would have failed at far less dense populations than the stroboscopic method). When this happens we can not tell which image belongs to which bubble. To solve this problem, we use two strobe lights instead of one, and make them each flash once with different colours. The time interval between these two flashes can be adjusted in advance. Then if we choose an appropriate shutter time, the photograph can show two images, of different colours, of the same bubble on the photo. An example is shown in Figure E2. Ten bubbles are shown in Figure E2. Each bubble gives one red and one blue image on the photo. Note that the image of each bubble has a characteristic ‘butterfly’ appearance, the two ‘wings’ of which corresponding to two small highlights on the bubble wall. Therefore the area of red (or blue) in the photograph is much less than the actually cross-sectional area of bubble, showing how use of the rise time removes this source of error which can occur in standard interpretation of images.

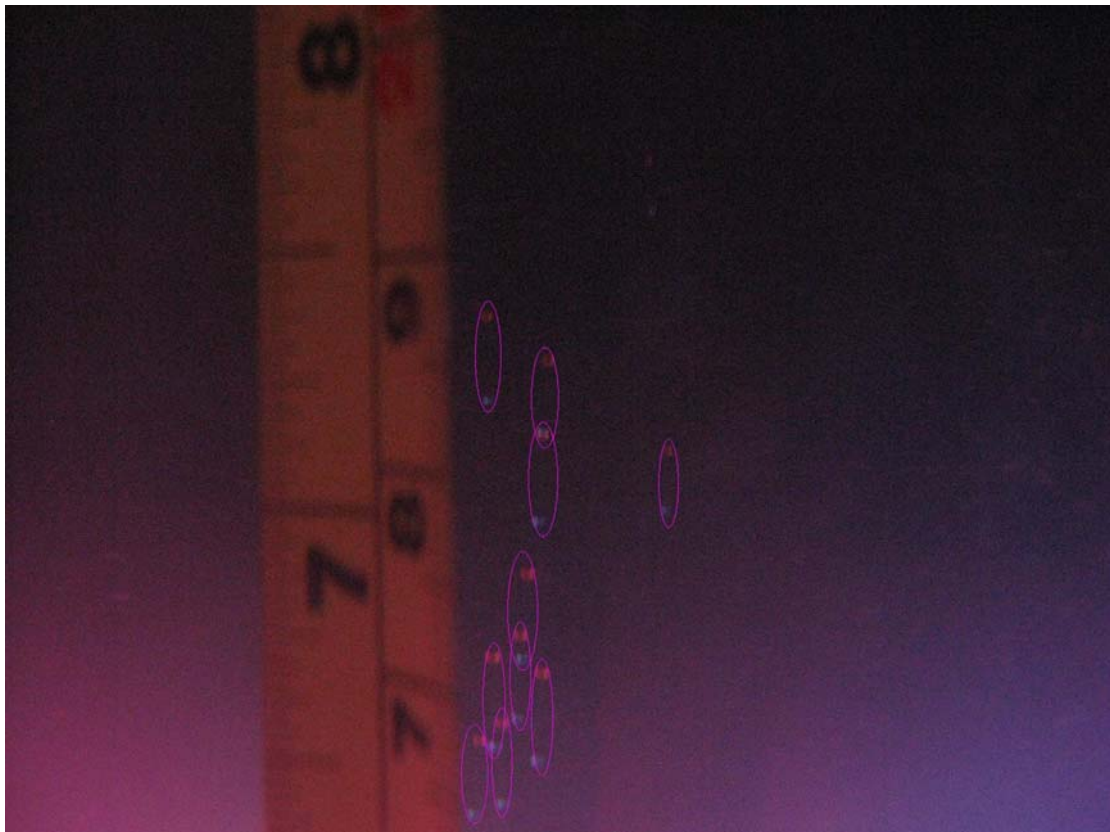


Figure E2: Two strobe lights give bubbles two images in different colours.

By checking the colour, the photo can be separate into two, one for red bubbles and one for blue bubbles. Comparing these two photos, we can get a bubble size distribution. The procedures how we get the bubble size distribution will be carefully introduced in the next section by using an example. This is what we called Multi-Colour Rising Time Method (μ CORT) (it could of course be extended by the use of more colour if necessary and perpendicular viewpoints in a given frame by use of angled mirrors).

E1. Processing procedures

As mentioned in last section, we use two strobe lights in the μ CORT method. It gives one bubble two different-coloured images on each photo. Here we give an artificial photo, which is shown in Figure E3 to illustrate how the bubble size distribution is obtained using the μ CORT method. Figure E3 contains 20 bubbles of 0.2 mm in radius. The bubbles are randomly distributed. By checking the colour, the red bubbles and the blue bubbles images can be picked up respectively, as shown in Figure E4. (In practice, a background elimination procedure and a contrast and brightness adjustment procedure are usually conducted before separating the photo by colour.)

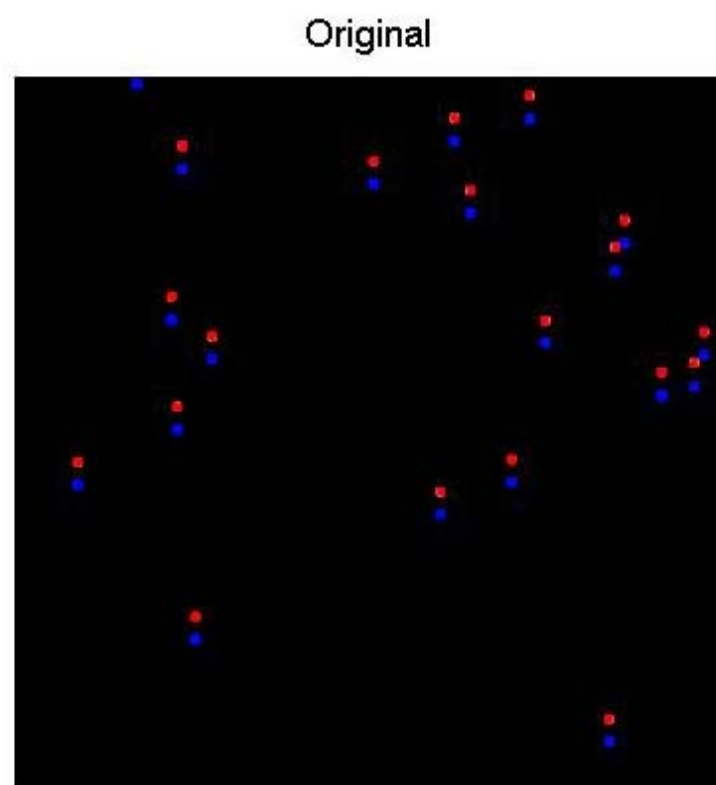


Figure E3: Artificial photo (20 bubbles, 0.2 mm in radius)

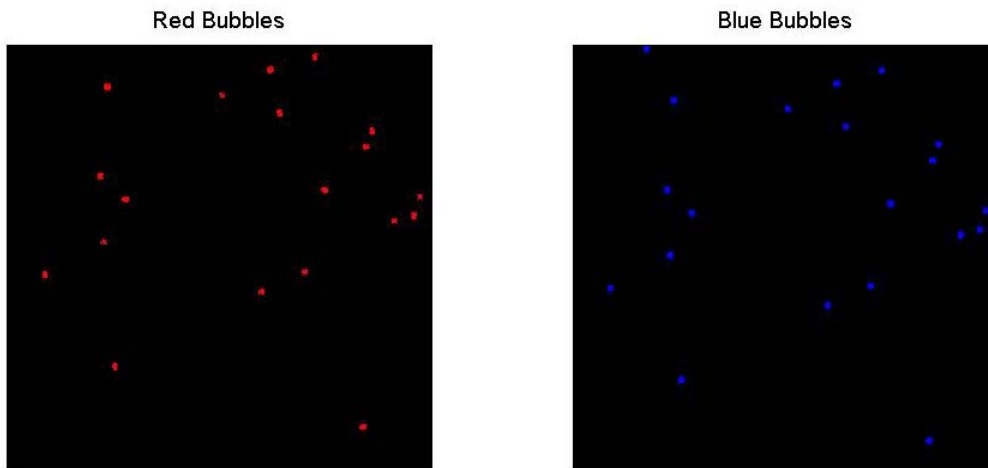


Figure E4: Separated Red and Blue photos



Figure E5: Black and white photos for Red and Blue bubbles.

To make the further processing easy, we change these two photos into black and white as shown in Figure E5. Comparing this two photos using 2 dimensional cross-correlation, we can get a probability distribution of bubble displacement. However, if we use the original photos shown in Figure E5 to get this distribution directly, the size of bubble may also influence the probability value. The result is shown in Figure E6 in red line. Although it can give us an obvious peak which shows the displacement of most of the bubble, this peak is not very concentrated and the maximum peak value is just 0.6, far less than 1 which it should be. Since the estimation of bubble displacement actually does not need any information of bubble size, here, we simplify a bubble into a point at its centre position, and calculate the distribution using the simplified photo. The result is shown in Figure E6 in blue line. It is much more concentrated and has a maximum value of 1, which means it is more accurate.

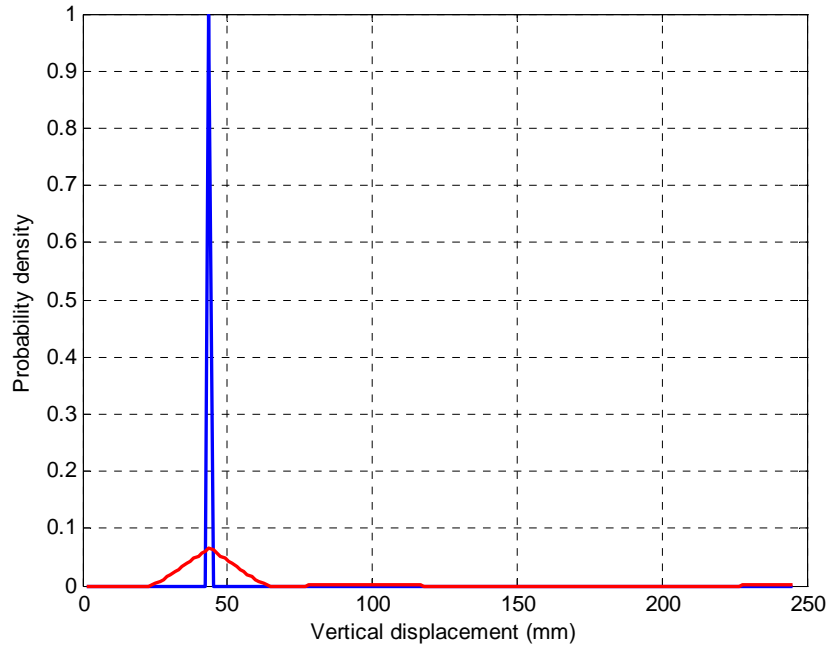


Figure E6: Probability of bubble displacement. (Red line is obtained using whole bubble image. Blue line is obtained using bubble centre position)

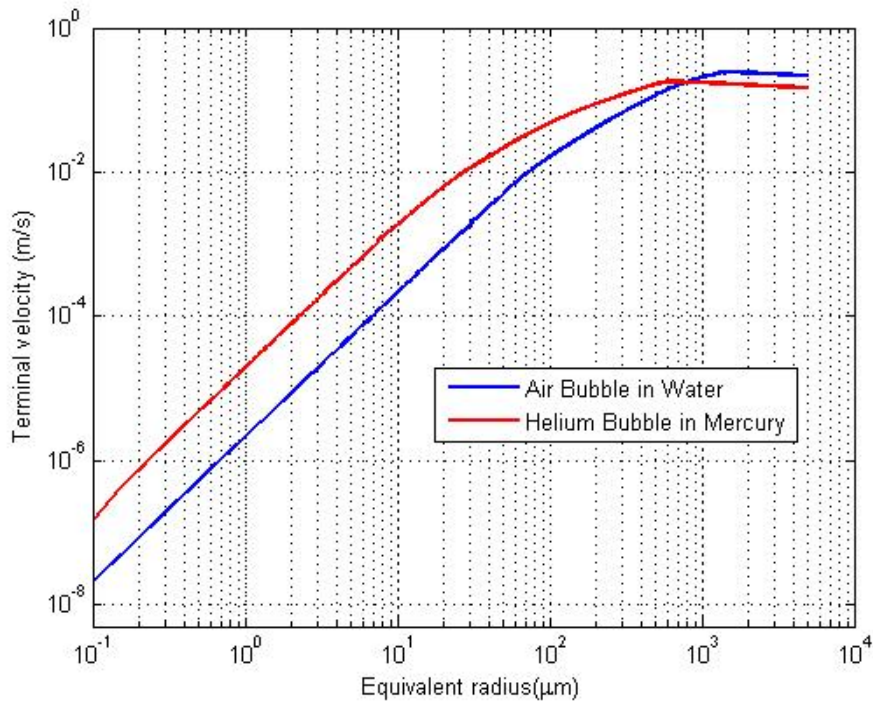


Figure E7: Terminal velocity against equivalent diameters (obtained using R. Clift's theory [39]). Readers should note that caution in the final paragraph of Appendix F.

Since we know the time interval, we can convert the displacement to rising speed by using the summary curve from Clift *et al.* [39] curve which is shown in Figure E7. Figure E7 shows how the Reynold' number data of Clift *et al.* [39] has been converted into rise speed data/bubble diameter data for air bubbles in water, and for helium bubbles in mercury. More detail of how to get these curves is

shown in Appendix F. The total bubble number on the photo can be obtained by checking the numbers of isolated white areas in Figure E5. Assuming the bubble number is proportional to the probability distribution, we obtain the bubble distribution on the photo, as shown in Figure E8.

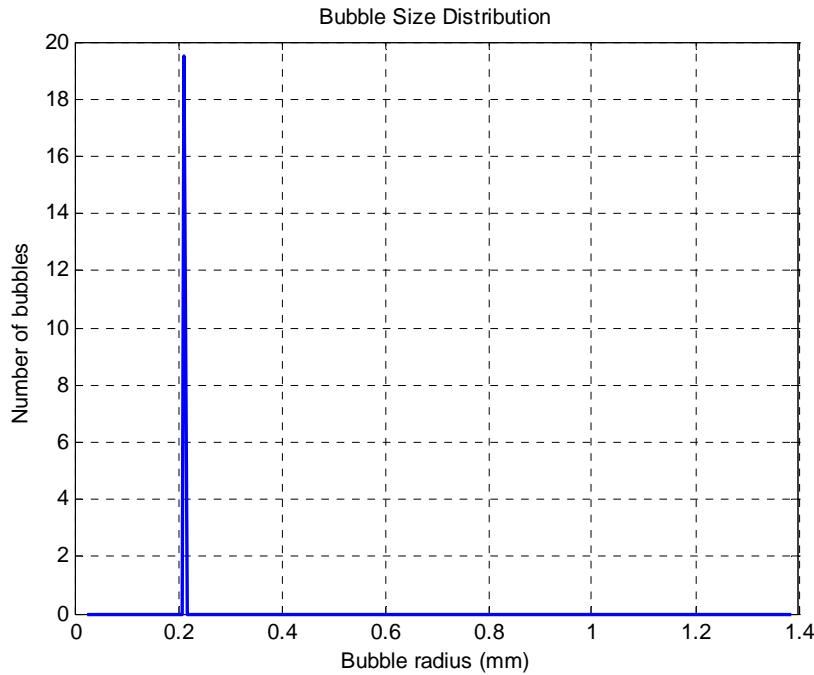


Figure E8: Bubble size distribution (Absolute Number)

However, the number of bubbles shown in Figure E8 is an absolute number. We need to convert it to number per unit volume.

Considering the geometrical characteristics of tube, we assume that

1. There is no optical magnification of bubbles along the perpendicular direction to the photo (out of the page or into the page).
2. The area in original photo is a slice of the cylindrical area as shown in Figure E9

Then the number of bubbles per unit volume, n_b , can be expressed as

$$n_b = \frac{4N}{\pi D^2 h}, \quad (\text{E-1})$$

where N is absolute number of bubbles, D is the diameter of tube and h is the height of tube which is shown in the photo.

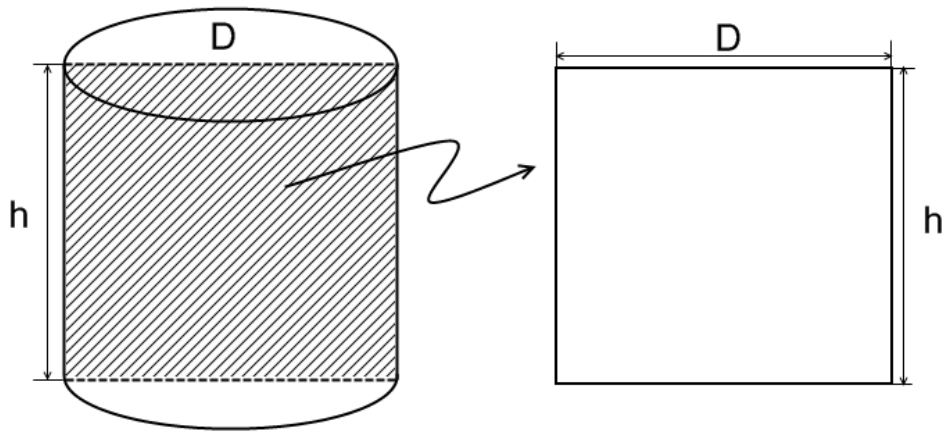


Figure E9: Converting absolute number of bubble to number per unit volume.

Then the bubble size distribution per unit volume for Figure E3 can be obtained and shown in Figure E10.

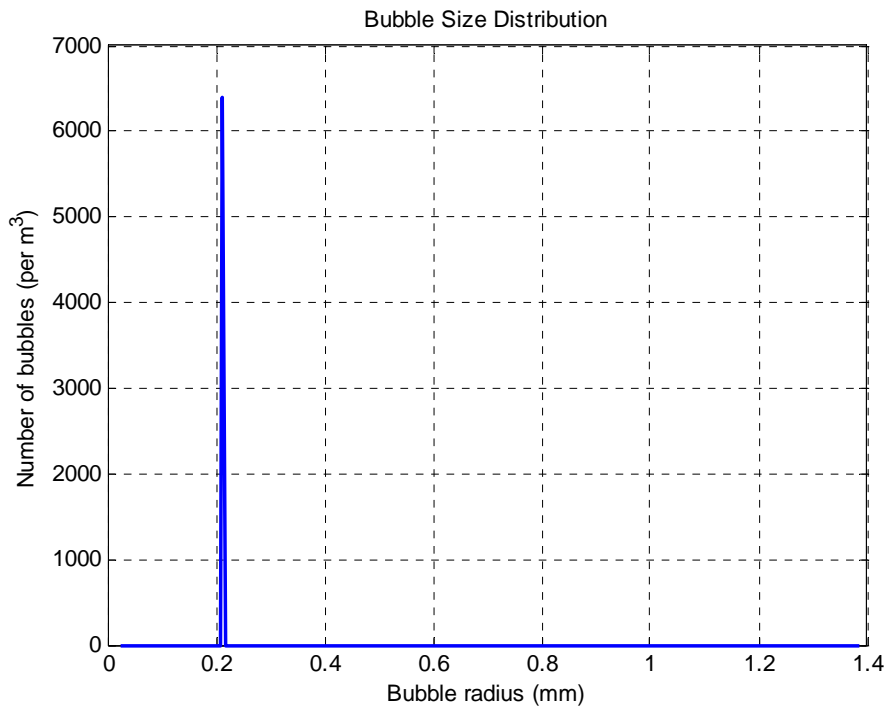


Figure E10: Bubble size distribution (per m³).

E2. Artificial case study for μ CORT

Before using this method in practice, we investigate its accuracy using artificial photos. Several examples are shown bellow. Figure E11(a) shows an artificial photo contains only on bubble. Figure E11(a) shows the relative bubble size distribution obtained by μ CORT method. The result shows that

there is only one bubble in that photo. Its estimated radius is about 0.092 mm, which has an error of 0.018 mm from the real value, 0.11 mm,

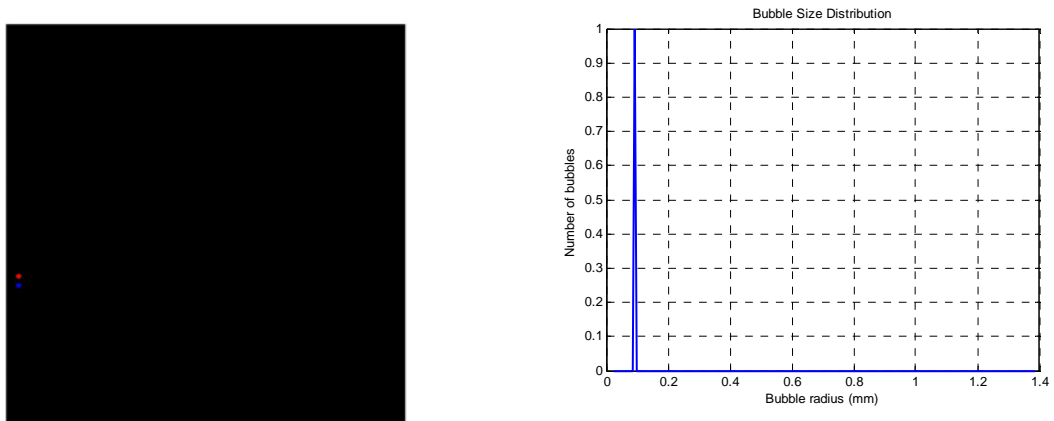


Figure E11: (a) Artificial photo (1 bubble, 0.11mm in radius) and (b) bubble size distribution for (a).

To test the method for an increase in the number of bubbles, Figure E12(a) shows a photo contains 100 bubbles which have uniform radius, 0.11 mm. The relative bubble size distribution is shown in Figure E12(b). In Figure E12(b), the estimated bubble size is also 0.092 mm, and the number of bubble in that radius is about 72 which is less than the real value, 100. Several reasons cause this error. 1) Some of the bubbles in Figure E12(a) overlap or very close to each other. In the image processing, μ CORT method may consider them as one single bubble. 2) The peak also has a width though it is very narrow. Summing up all the values around peak, the total number is about 90. 3) There is some noise shown in Figure E12(b), though they are very small. These noises can be reduced by averaging a number of results.

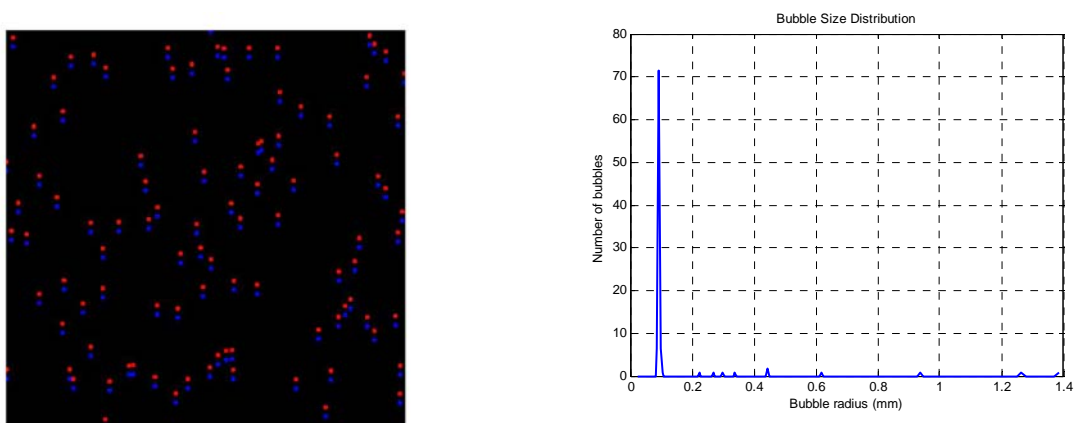


Figure E12: (a) Artificial photo (100 bubble, 0.11mm in radius) and (b) bubble size distribution for (a).

As we know, in practice, the bubbles are never the same size, a photo showing two different sizes of bubbles is also investigate. This photo is shown in Figure E13(a). It contains 100 bubbles, 80 of which is in radius of 0.11 mm, 20 of which is in radius of 0.16 mm. The bubble size distribution is shown in Figure E13(b). From Figure E13(b), two peaks can be found. One is at 0.092 mm, one is at 0.148 mm. They both have an error from the real values, about 0.018 mm and 0.012 mm respectively.

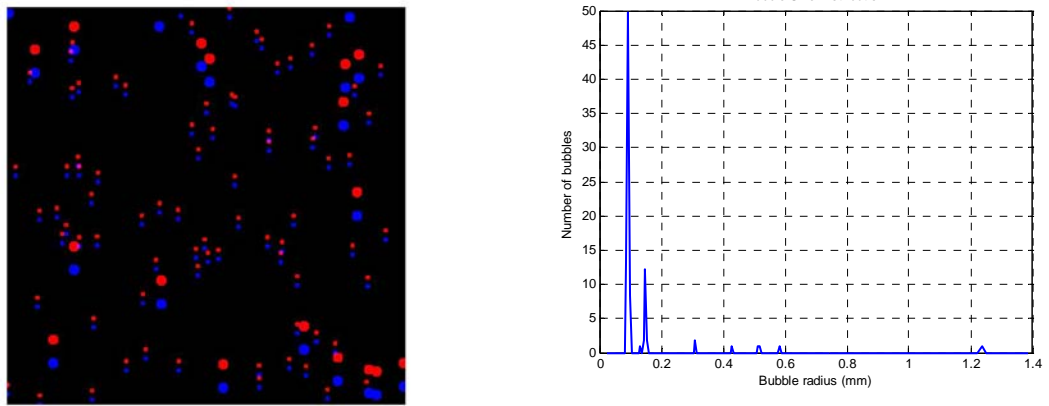


Figure E13: (a) Artificial photo (80 bubbles of 0.11mm radius and 20 bubbles of 0.16mm radius) and (b) bubble size distribution for (a).

As shown in Figures E11 to E13, the μ CORT method has an error in estimating bubble size, though they are very small. By investigating a number of cases we give a correction curve which is shown in Figure E14.

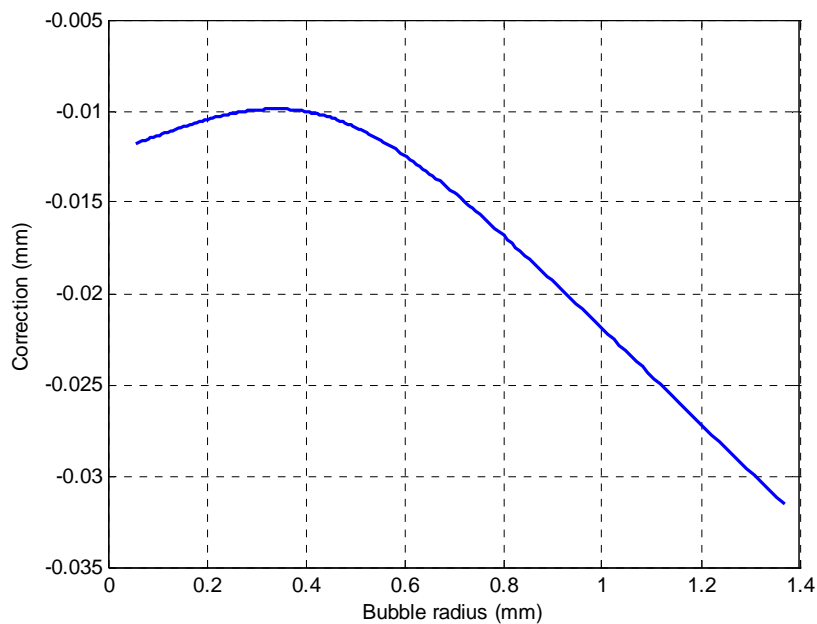


Figure E14: Correction curve for bubble size estimation using μ CORT method.

APPENDIX F: TERMINAL VELOCITY OF BUBBLE IN LIQUID

The data summarized by Clift *et al.* [39] showed that the shape of gas bubbles in liquid can be closely approximated as a sphere in the small size range (typically $d < 1$ mm), an ellipsoid in the intermediate size range (typically $1 < d < 15$ mm), and a spherical-cap in the large size range (typically $d > 15$ mm), where d is the equivalent particle diameter which is the diameter of a sphere that would occupy the same volume as the aspherical bubbles. Based on theoretical analysis and experimental studies, Clift *et al.* gave out the following formula to show the relationship between bubble terminal velocity and their sizes.

1) In the regime of spherical shape

$$u_t = \frac{R\mu}{\rho d}, \quad (\text{F-1})$$

where u_t is terminal velocity, R is Reynold number, μ is the dynamic viscosity of ambient fluid, ρ is density of ambient fluid.

2) In the regime of ellipsoidal shape

$$u_t = \frac{\mu}{\rho d} M^{-0.149} (J - 0.857), \quad (\text{F-2})$$

where

$$J = \begin{cases} 0.94H^{0.757} & (2 < H < 59.3) \\ 3.42H^{0.441} & (H > 59.3) \end{cases}, \quad (\text{F-3})$$

$$H = \frac{4}{3} EoM^{-0.149} \left(\frac{\mu}{\mu_w} \right)^{-0.14}, \quad (\text{F-4})$$

μ_w is the dynamic viscosity of water,

$$M = g\mu^4\sigma^3 \frac{\Delta\rho}{\rho}, \quad (\text{F-5})$$

$$Eo = gd^2\Delta\rho/\sigma \quad (\text{F-6})$$

σ is interfacial tension, g is gravity acceleration, $\Delta\rho$ is density difference between gas and ambient fluid.

3) In the regime of spherical-cap

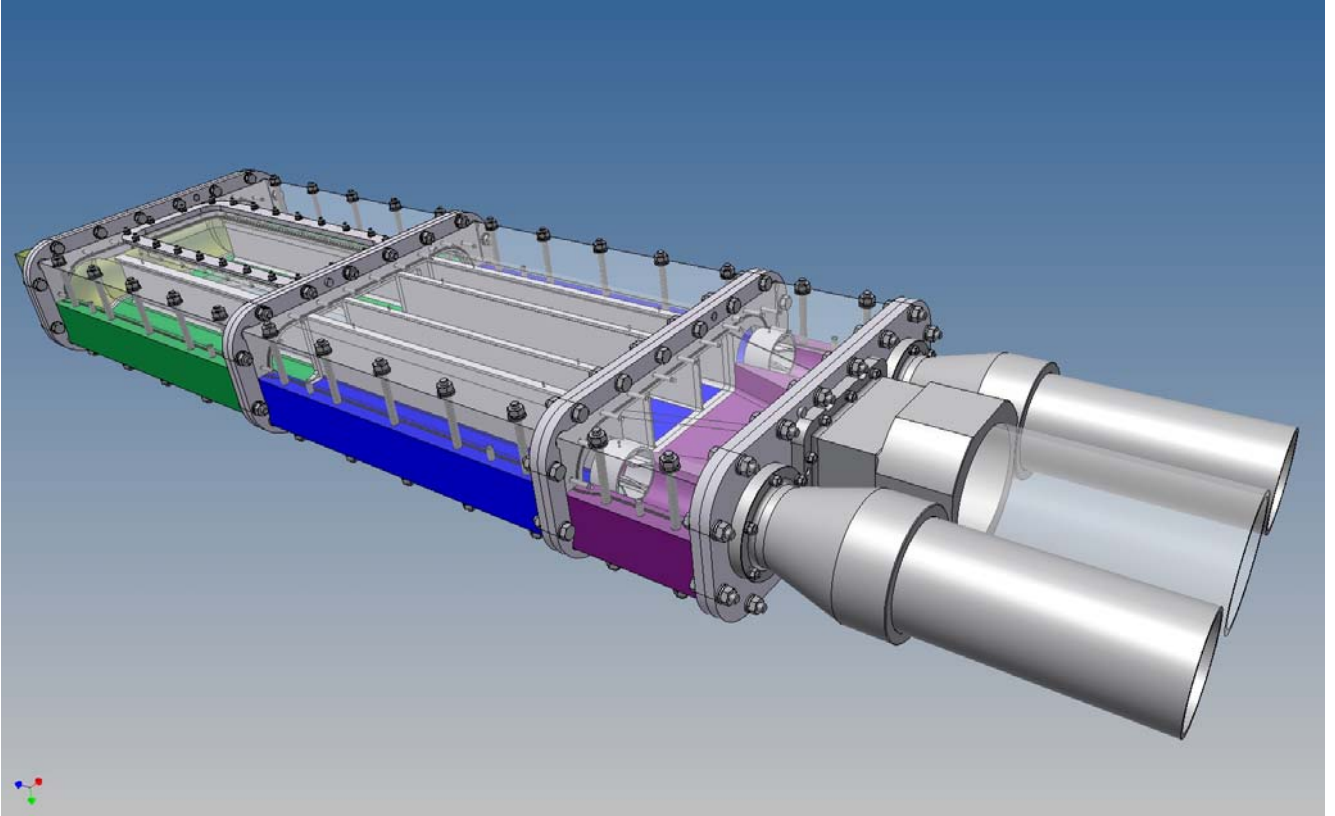
$$u_r = 0.771\sqrt{gd \Delta\rho/\rho}, \quad (\text{F-7})$$

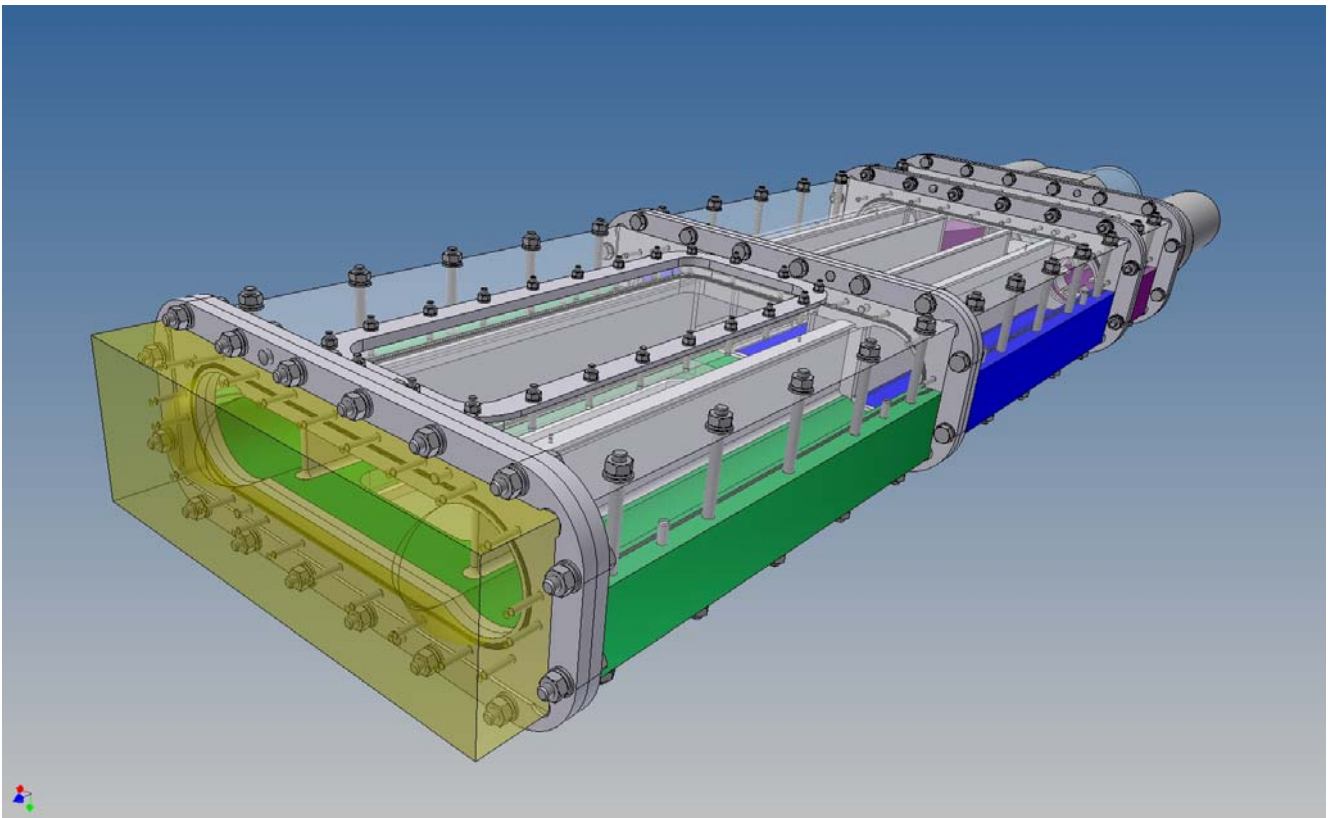
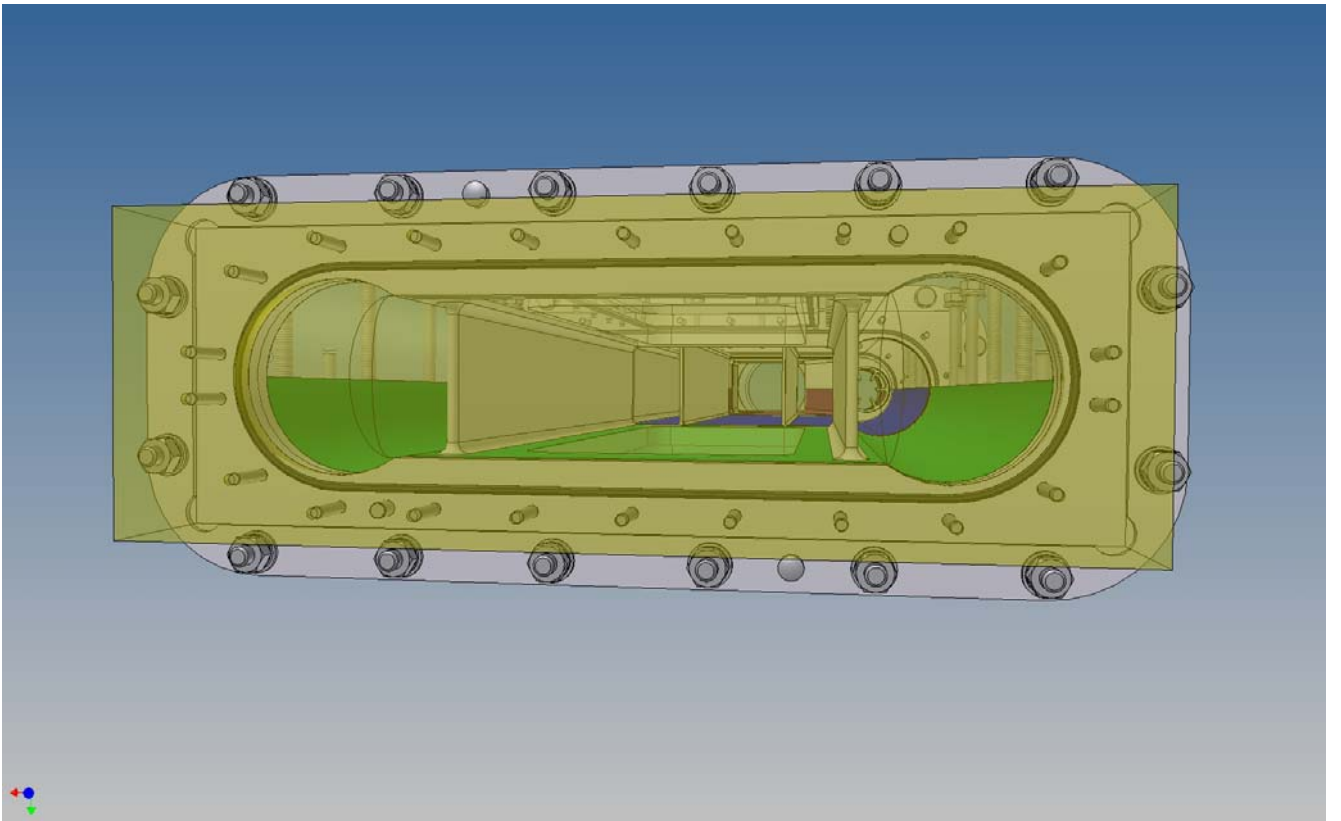
By using the formulae above, we obtained the curves of bubble rise speed against bubble size in water and mercury shown in Figure E7. The curve for water is also used in the optical bubble population estimation method to convert the bubble rising speed into bubble size.

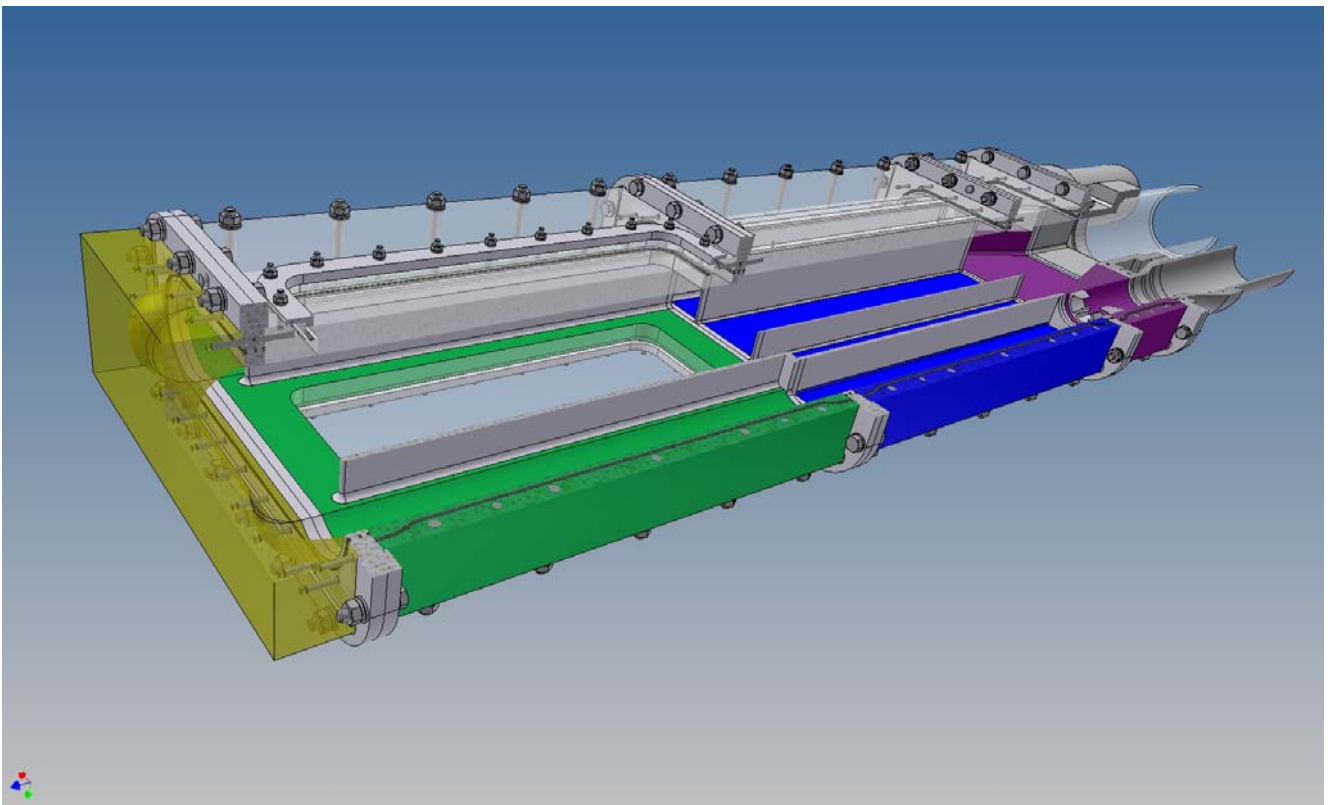
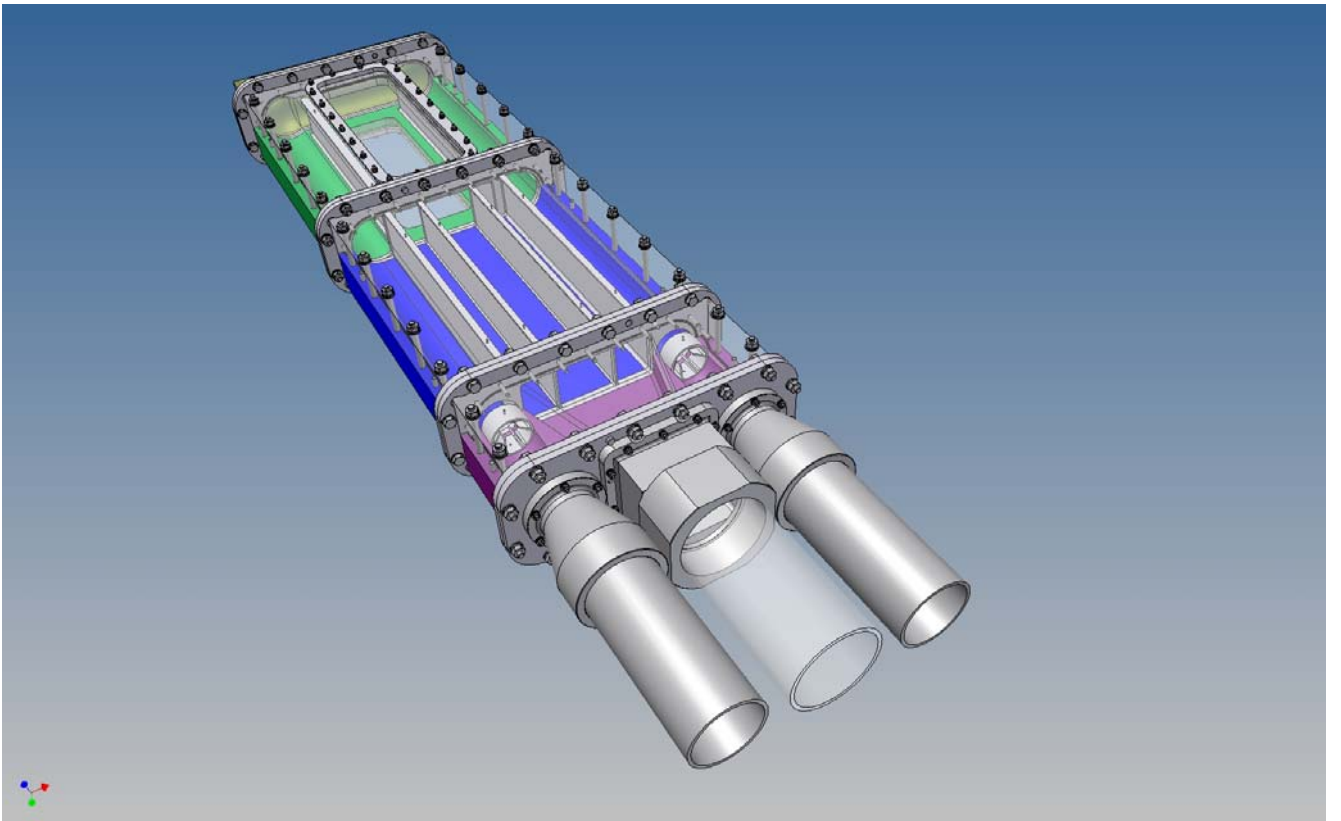
It is recognized that these relationships are derived from empirical studies of mainly air bubbles in water, and that, in the large-bubble regime in particular, the dataset is less populous than one might wish. For these reasons the accuracy of the predicted rise times in mercury are likely to decrease in the large-bubble regime. To date the μCORT method has only been applied to air bubbles in water (the optical opacity of mercury would make its use their problematic), and the largest bubble that has measured with μCORT was ~ 1.4 mm in radius. It is envisaged that measurements with μCORT will be normally involve populations of bubbles that are dominated by bubbles of less than 100 μm radius

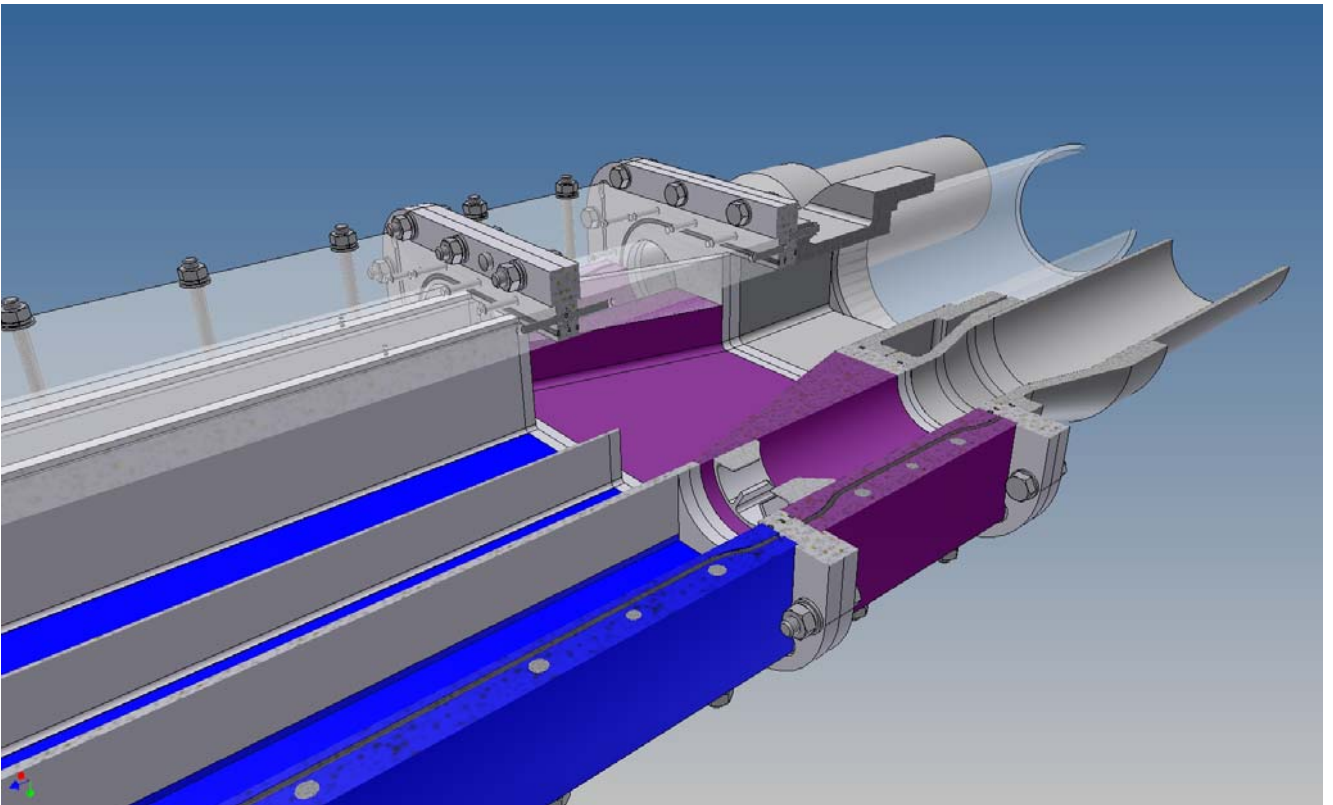
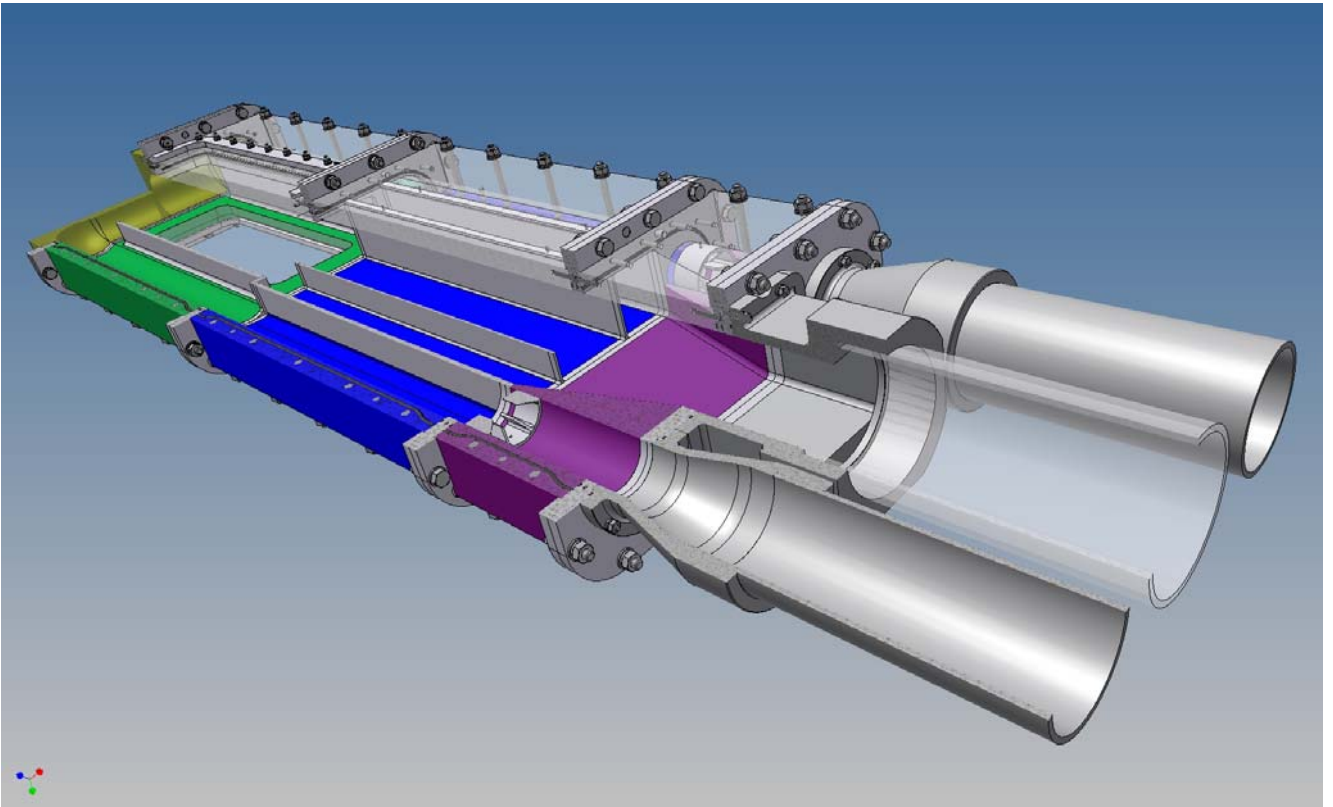
APPENDIX G: DESIGN FOR MIMIC OF TEST SECTION

CAD schematics of the design for the PMMA mimic of the test section, which will be inserted in place of the current joint (shown in Figure 1.5), as indicated in Figure 1.4.









REFERENCES

- [1] T. G. Leighton, "From seas to surgeries, from babbling brooks to baby scans: The acoustics of gas bubbles in liquids," *International Journal of Modern Physics B*, **18**(25), 3267-3314 (2004).
- [2] T. G. Leighton, D. G. Ramble, A. D. Phelps, C. L. Morfey and P. P. Harris, "Acoustic detection of gas bubbles in a pipe," *Acta Acustica*, **84**, 801-814 (1998).
- [3] T. G. Leighton, P. R. White, C. L. Morfey, J. W. L. Clarke, G. J. Heald, H. A. Dumbrell, and K. R. Holland, "The effect of reverberation on the damping of bubbles," *Journal of the Acoustical Society of America*, **112**(4), 1366-1376 (2002).
- [4] N. D. Breitz and H. Medwin, "Instrumentation for in-situ acoustical measurements of bubble spectra under breaking waves," *Journal of the Acoustical Society of America*, **86**, 739-743 (1989).
- [5] D. M. Farmer and S. Vagle, "Bubble measurements using a resonator system," in *Natural physical processes associated with sea surface sound*, T.G. Leighton (ed.), (University of Southampton, UK 1997), 155-162.
- [6] D. M. Farmer, S. Vagle, and A. D. Booth, "A free-flooding acoustical resonator for measurement of bubble size distributions," *J. Atmos. Ocean Technol.*, **15**, 1132-1146 (1998).
- [7] J. M. Muggleton, M. J. Brennan, and P. W. Linford, "Axisymmetric wave propagation in fluid-filled pipes: wavenumber measurements in in vacuo and buried pipe," *Journal of Sound and Vibration*, **270**, 171-190 (2004).
- [8] J. M. Muggleton and M. J. Brennan, "Axisymmetric wave propagation in buried, fluid-filled pipes: effects of wall discontinuities," *Journal of Sound and Vibration*, **281**, 849-867 (2005).
- [9] V. A. Del Grosso, "Analysis of multimode acoustic propagation in liquid cylinders with realistic boundary conditions - Application to sound speed and absorption measurements," *Acustica*, **24**, 299-311 (1971).
- [10] L. D. Lafleur and F. D. Shields, "Low-frequency propagation modes in a liquid-filled elastic tube waveguide," *J. Acoust. Soc. Am.* **97**(3), 1435-1445 (1985).
- [11] K. F. Graff, *Wave Motion in Elastic Solids*, (Dover 1975), pp. 465.

- [12] B. T. Hefner and P. L. Marston, "Backscattering enhancements associated with subsonic Rayleigh waves on polymer spheres in water: Observation and modeling for acrylic spheres", *J. Acoust. Soc. Am.* **107**(4), 1930-1936 (2000).
- [13] T. N. Grigsby and E. J. Tajchman, "Properties of Lamb waves relevant to the ultrasonic inspection of thin plates," *IRE Trans. Ultra. Eng.* **UE-8**, 26-33 (1961).
- [14] A. Prosperetti, L. A. Crum, and K. W. Commander, "Nonlinear bubble dynamics," *J. Acoust. Soc. Am.* **83**(2), 502-514 (1988).
- [15] K. W. Commander and A. Prosperetti, "Linear pressure waves in bubbly liquids: Comparison between theory and experiments," *J. Acoust. Soc. Am.* **85**(2), 732-746 (1989).
- [16] A. Prosperetti, "Thermal effects and damping mechanisms in the forced radial oscillations of gas bubbles in liquid," *J. Acoust. Soc. Am.* **61**(1), 17-27 (1977).
- [17] T. G. Leighton, *The Acoustic Bubble*, (Academic Press 1994).
- [18] Jr. C. Devin, "Survey of thermal, radiation, and viscous damping of pulsating air bubbles in water," *J. Acoust. Soc. Am.*, **31**(12), 1654-1667 (1959).
- [19] A. I. Eller, "Damping Constants of Pulsating Bubbles," *J. Acoust. Soc. Am.* **47**(5), 1469-1470, (1970).
- [20] T. G. Leighton, "What is ultrasound?," *Progress in Biophysics and Molecular Biology*, **93**(1-3), 3-83 (2007).
- [21] T. G. Leighton, S. D. Meers, and P. R. White, "Propagation through nonlinear time-dependent bubble clouds and the estimation of bubble populations from measured acoustic characteristics," *Proc. R. Soc. Lond. A* **460**, 2521-2550 (2004).
- [22] T. G. Leighton and G. B. N. Robb, "Preliminary mapping of void fractions and sound speeds in gassy marine sediments from subbottom profiles," *Journal of the Acoustical Society of America*, **124**(5), EL313-EL320 (2008).
- [23] T. G. Leighton, D. G. Ramble, and A. D. Phelps, "The detection of tethered and rising bubbles using multiple acoustic techniques," *Journal of the Acoustical Society of America*, **101**(5), 2626-2635 (1997).
- [24] T. G. Leighton, A. D. Phelps, D. G. Ramble, and D. A. Sharpe, "Comparison of the abilities of

- eight acoustic techniques to detect and size a single bubble,” *Ultrasonics*, **34**, 661-667 (1996).
- [25] K. W. Commander and R. J. McDonald, “Finite-element solution of the inverse problem in bubble swarm acoustics,” *J. Acoust. Soc. Am.* **89**(2), 592-597 (1991).
- [26] A. N. Tikhonov and V. Y. Arsenin, *Solution of ill-posed problems*, (Wiley 1977).
- [27] P. C. Hansen, “Rank-deficient and discrete ill-posed problems: numerical aspects of linear inversion,” Philadelphia, PA: SIAM.
- [28] T. G. Leighton, “A method for estimating sound speed and the void fraction of bubbles from sub-bottom sonar images of gassy seabeds,” *ISVR technical report*, No. **320**. Dec, (2007).
- [29] H. Wright, C. S. N. Faraday, E. F. T. White, and L. R. G. Treloar, “The elastic constants of oriented glassy polymers,” *J. Phys. D: Appl. Phys.*, **4**, 2002-2014, 1971.
- [30] T. G. Leighton, K. J. Fagan, and J. E. Field, “Acoustic and photographic studies of injected bubbles,” *European Journal of Physics*, **12**, 77-85, (1991).
- [31] T. G. Leighton, P. C. Hsueh, J. R. Chaplin, and J. Y. Liu, “Using the optical fibre sensors to measure the void fraction and distribution of bubble clouds in upper-ocean environment,” 1st. Draft, (2009).
- [32] G. T. Yim and T. G. Leighton, “The use of acoustics for real-time on-line monitoring of ceramic ‘slip’ in pottery pipelines,” *Proc. Inst. Acoust.*, **28**(1), 862-875, (2006).
- [33] G. Deane and M. Stoke, “Air Entrainment Processes and Bubble Size Distributions in the Surf Zone,” *Journal of Physical Oceanography*, **29**, 1393-1402, (1999).
- [34] M. Abramowitz and I. A. Stegun, *Handbook of Mathematical Functions with Formulas, Graphs, and Mathematical Tables*, (Dover, 1965).
- [35] A. Cartellier, “Optical Probes for Multiphase Flow Characterization: Some Recent Improvements,” *Chem. Eng. Technol.*, **24**(5), 535-538, (2001).
- [36] P. Hsueh , “Developing a new optical fiber sensor system to measure the void fraction and distribution of bubble clouds in a laboratory and upper-ocean environment,” Ph.D. dissertation, University of Southampton, Institution of Sound and Vibration Research (Draft written in 2008).
- [37] S. Saberi, K. Shakourzadeh, D. Bastoul, and J. Militzer, “Bubble size and velocity measurement

in gas-liquid systems: Application of fiber optic technique to pilot plant scale," *Can. J. Chem. Eng.*, **73**, 253-257, (1995).

[38] C. D. Serdula and M. R. Loewen, "Experiments Investigating the Use of Fiber-Optic Probes for Measuring Bubble-Size Distributions," *IEEE J. Ocean. Eng.*, **23**(4), 385-399, (1998).

[39] R. Clift, J. R. Grace, and M. E. Weber, *Bubbles, Drops, and Particles* (Academic press, 1978).